



UNIVERSIDAD DE CHILE
FACULTAD DE CIENCIAS FÍSICAS Y MATEMÁTICAS
DEPARTAMENTO DE INGENIERÍA ELÉCTRICA

DESIGN OF OPTICAL SYSTEMS FOR W-BAND ASTRONOMICAL HETERODYNE
CAMERAS

TESIS PARA OPTAR AL GRADO DE MAGÍSTER EN CIENCIAS DE LA
INGENIERÍA, MENCIÓN ELÉCTRICA

MEMORIA PARA OPTAR AL TÍTULO DE INGENIERA CIVIL ELÉCTRICA

ROCÍO GABRIELA MOLINA MORENO

PROFESOR GUÍA:
NICOLÁS ANDRÉS REYES GUZMÁN

PROFESOR CO-GUÍA:
FAUSTO PATRICIO MENA MENA

MIEMBROS DE LA COMISIÓN:
ROLANDO DÜNNER PLANELLA
ERNEST ALEXANDER MICHAEL

Este trabajo ha sido parcialmente financiado por FONDECYT a través del proyecto
11151022.

SANTIAGO DE CHILE
2017

RESUMEN DE LA TESIS PARA OPTAR
AL GRADO DE MAGÍSTER EN CIENCIAS
DE LA INGENIERÍA, MENCIÓN ELÉCTRICA Y
AL TÍTULO DE INGENIERA CIVIL ELÉCTRICA
POR: ROCÍO GABRIELA MOLINA MORENO
FECHA: 2017
PROF. GUÍA: SR. NICOLÁS ANDRÉS REYES GUZMÁN
PROF. CO-GUÍA: SR. FAUSTO PATRICIO MENA MENA

DESIGN OF OPTICAL SYSTEMS FOR W-BAND ASTRONOMICAL HETERODYNE CAMERAS

La nueva generación de telescopios que se instalarán en el mundo y particularmente en Chile está enfocada en la búsqueda de objetivos científicos de alto impacto. Para esto, la tecnología utilizada debe ser de vanguardia, de modo de lograr un mejor desempeño que el logrado actualmente. Este desafío cae en las manos de la ingeniería y esta tesis se enmarca en dicho contexto.

El objetivo general es desarrollar sistemas ópticos intermedios para permitir la implementación de cámaras heterodinas en el rango de 85 - 115 GHz (banda W extendida). Para esto se desarrollan dos sub-proyectos. En el primero se trabaja con el diseño original del radio-telescopio SMWT de 1.2 m que se encuentra actualmente en el Observatorio Astronómico Nacional en Cerro Calán. Se estudia la factibilidad de tener una cámara heterodina sin la necesidad de añadir elementos ópticos adicionales.

Para el segundo proyecto se utiliza el diseño de la antena reflectora de 12 m tipo ALMA y se diseña un sistema óptico intermedio consistente en un telescopio Gaussiano. Se busca adaptar la óptica de la antena con un receptor heterodino de 7 pixeles. Este diseño es aplicable a un mejoramiento futuro de ALMA o para el proyecto LLAMA, que está en desarrollo.

En ambos proyectos se trabaja con modelos matemáticos desarrollados en Matlab y basados en el modelo cuasi-óptico. Posteriormente se afinan los modelos usando softwares de simulación. Parámetros de desempeño como la eficiencia de apertura, temperatura de ruido, truncamiento del haz, componente de polarización cruzada y precisión de la superficie son tomados en cuenta para el diseño.

Se logra encontrar una posición y cintura del haz adecuada para el receptor heterodino de 7 pixeles del SMWT. La eficiencia normalizada de los haces laterales es de 92.9 % respecto al pixel central. Se requiere una separación de 23.6 mm entre haces con cintura de 6.8 mm en el plano focal Cassegrain. No se requiere el uso de óptica adicional.

Para el diseño en una antena de 12 m se obtiene una separación de 58.6 mm en el plano focal Cassegrain, una cintura de haz de 16.8 mm y una eficiencia normalizada de 96.9 % para la frecuencia central (100 GHz). El diseño tanto para ALMA como para LLAMA consiste en un telescopio Gaussiano usando dos espejos elipsoidales y compactado mediante el uso de espejos planos. La magnificación en cada caso es diferente debido a las restricciones de espacio particulares a cada uno. Esto implica que la cintura del haz en la ventana de vacío es diferente.

RESUMEN DE LA TESIS PARA OPTAR
AL GRADO DE MAGÍSTER EN CIENCIAS
DE LA INGENIERÍA, MENCIÓN ELÉCTRICA Y
AL TÍTULO DE INGENIERA CIVIL ELÉCTRICA
POR: ROCÍO GABRIELA MOLINA MORENO
FECHA: 2017
PROF. GUÍA: SR. NICOLÁS ANDRÉS REYES GUZMÁN
PROF. CO-GUÍA: SR. FAUSTO PATRICIO MENA MENA

DESIGN OF OPTICAL SYSTEMS FOR W-BAND ASTRONOMICAL HETERODYNE CAMERAS

The new generation of telescopes that will be installed in the world and particularly in Chile is focused on the search of high-impact scientific objectives. For this, the technology used must be cutting edge, in order to achieve a better performance than currently achieved. This challenge falls into the hands of engineering and this thesis is developed in that context.

The general objective is to develop intermediate optical systems to allow the existence of heterodyne cameras in the range of 85 - 115 GHz (extended W band). For this, two sub-projects are developed. In the first one, we work with the original design of the 1.2-m SMWT telescope that is currently in the National Astronomical Observatory in Cerro Calán. We study the feasibility of having a heterodyne camera without the need to add extra optical elements.

For the second project, the parameters of the 12-m ALMA antenna are used. An intermediate optical system consisting of a Gaussian Beam Telescope is designed. We seek to adapt the optics of the antenna with a heterodyne receiver of 7 pixels. This design is applicable to a future ALMA upgrade or to the LLAMA project, which is under development.

In both projects, we work with mathematical models developed in Matlab and based on the quasi-optical model. Subsequently, fine-tuning the models is performed with simulation software. Performance parameters such as aperture efficiency, noise temperature, beam truncation, cross-polar component and surface accuracy are taken into account for the design.

We find an appropriate beam position and waist for the SMWT 7-pixel heterodyne receiver. The normalized efficiency of the lateral beams is 92.9% with respect to the central beam. A 23.6-mm spacing between beams with a 6.8-mm waist in the Cassegrain focal plane is required. No additional optics are necessary.

For the design in a 12-m antenna, a 58.6-mm spacing is obtained in the Cassegrain focal plane, a beam waist of 16.8 mm and a normalized efficiency of 96.9% for the central frequency (100 GHz). The design for both, ALMA and LLAMA, consists of a Gaussian Beam Telescope using two ellipsoidal mirrors and compacted by the use of flat mirrors. The magnification in each case is different due to the space constraints particular to each. This implies that the waist of the beam in the vacuum window is different.

*To hug you,
to Chito and Jani.*

Acknowledgements

My interest in science started with fascination for light. The moment in life when we realize that colors are not just colors, colors are light... and then I imagined everything without light: a black mass that had been forgotten to be painted.

Many years later, I decided to schedule a meeting with professor Patricio in order to work on one of his projects. This was a major encourage for my life today. I will never regret this decision.

After that meeting I began to work at the Millimeter Wave Laboratory, where Valeria and also everyone else helped me at some point. Another important person was Nicolás who guided my work with enthusiasm, new ideas, but always leaving me free to run my own ideas... I had the best tutors.

When this topic was assigned to me I did not know much about it. Now that I have the knowledge, I would have chosen this topic every time I had the chance. I enjoyed this process and everything I learned. I feel very lucky.

I also want to thank my family. Starting with my grandparents, who have done everything possible for the lives of their children, contemplating now how their grandchildren enjoy their own lives. To my parents, who raised their children to be what they wanted to be, to be happy.

To Pin and Pomi, with whom I have shared so many things that I can communicate without having to speak. To them and all my uncles, aunts and cousins: thank you, I am really proud of my family.

Well, to my friends and "the girls". Those who supported me not having a clue of what I was doing, and the others, who knew quite well and gave me their opinion and help, specially to find some specific code and other computational stuff.

Finally, to Tristi, the pilot who has taken me, literally and not literally, to all the other adventures that have happened to me.

To all, thank you very much!

Próxima estación...

Contents

1	Introduction	1
1.1	Hypothesis	3
1.2	Objectives	3
1.2.1	General Objective	3
1.2.2	Specific Objectives	4
1.3	Structure of the Thesis	4
2	Bibliographic Review	5
2.1	Optical Theory	5
2.1.1	Geometrical Optics	6
2.1.2	Quasioptical Theory	8
2.1.3	Radiation Pattern	10
2.2	Optical Devices	12
2.2.1	Cassegrain Antennas	13
2.2.2	Horn Antennas	15
2.2.3	Focusing Elements: Lenses and Mirrors	16
2.3	Heterodyne Receivers	20
2.3.1	Noise Temperature	21
2.4	Imaging Systems	22
2.4.1	Gaussian Telescope	23
2.4.2	Pixel distances	24
2.4.3	Pixel distribution	25
2.5	Revision of Existing Focal Plane Arrays	25
2.5.1	Submillimeter and Terahertz Regime	25
2.5.2	Millimeter Regime	27
2.6	Summary	27
3	Feasibility of a Camera in the SMWT	28
3.1	Brief History of the SMWT	28
3.2	Description of the Antenna	29
3.3	Simulations with the current feed antenna	30
3.3.1	Central Feed	30
3.3.2	Off-axis Feed	32
3.4	Simulations with a new feed antenna	35
3.4.1	Using the same aperture	35
3.4.2	Using an optimized aperture for a 7-pixel focal plane array	36

3.5	Analysis of the Results	37
3.6	Summary	38
4	Design of an Optical System for a W-Band Camera of a 12-m Antenna	39
4.1	ALMA project	39
4.2	Description of the ALMA 12-m antenna	40
4.3	Design considerations	41
4.4	Design of intermediate optics for ALMA Band-3	42
4.4.1	Restrictions for ALMA	42
4.4.2	Design of a Gaussian-Beam Telescope for ALMA Band-3 camera . . .	45
4.4.3	Mechanical considerations for ALMA	48
4.5	Tolerances in construction and assembly	50
4.6	Analysis of results obtained for ALMA	51
4.7	LLAMA project	52
4.8	Description of the LLAMA 12-m antenna	52
4.9	Design of intermediate optics for LLAMA Band-3	53
4.9.1	Restrictions for LLAMA	53
4.9.2	Design of a Gaussian Beam Telescope for LLAMA Band-3 camera . .	55
4.9.3	Expansion of LLAMA's Band-3 Camera Using More Pixels	57
4.9.4	Mechanical considerations for LLAMA	58
4.10	Analysis of results obtained for LLAMA	58
4.11	Summary	59
5	Conclusion	60
5.1	Further Work	61
	Bibliography	62
A	Formulas for conic sections	68
B	ABCD matrix	69
C	Hexagonal distribution	71
D	Parameters of the SMWT in its original units	73
E	Simulations of the SMWT in Zemax	75
F	Results for the SMWT	76
G	Simulations of the ALMA and LLAMA 12-m antenna in Zemax	83
H	Results for the 12-m antenna	86

List of Tables

2.1	Review of existing submillimeter and terahertz heterodyne arrays.	26
2.2	Review of existing millimeter heterodyne arrays.	27
3.1	Main parameters of the Cassegrain antenna of the SMWT (Mini).	29
3.2	Main parameters of the corrugated horn antenna of the SMWT (Mini). . . .	30
3.3	Illumination efficiency and percentage of power that passes through the main hole. Parameters for the outer pixel using the actual characteristics of the feed horn of the SMWT.	32
3.4	Illumination efficiency and percentage of power that passes through the main hole. Parameters for the outer pixel using the actual electrical characteristics of the feed horn of the SMWT.	35
3.5	Illumination efficiency and percentage of power that passes through the main hole. Parameters for the outer pixel using an hypothetical beam waist for the SMWT.	36
4.1	Main parameters of the 12-m Cassegrain antenna of ALMA.	41
4.2	Illumination efficiency and percentage of power that passes through the hole of the primary reflector for a 12-m ALMA antenna. Parameters for the outer pixel using the actual characteristics of the feed horn+lens+ellipsoidal mirror of Band-3	43
4.3	Parameters for the GBT of ALMA.	46
4.4	Illumination efficiency and percentage of power that passes through the main hole of a 12-m ALMA antenna. Parameters for the outer pixel using the GBT designed for Band-3	47
4.5	Beam distortion in curved mirrors due to reflections and cross polarization in ALMA's GBT	48
4.6	Parameters for the GBT of LLAMA.	55
4.7	Illumination efficiency and percentage of power that passes through the main hole of a 12-m LLAMA antenna. Parameters for the outer pixel using the GBT designed for W band.	56
4.8	Beam distortion in curved mirrors due to reflections and cross polarization in LLAMA's GBT	56
4.9	Comparative analysis of hexagonal cameras with 7, 19, 37 and 61 pixels. . .	57
A.1	Main parameters and formulas to define a conic section.	68
B.1	Examples of ABCD matrix.	69

D.1	Main parameters of the Cassegrain antenna of the SMWT (Mini) in inches. .	73
D.2	Main parameters of the corrugated horn antenna of the SMWT (Mini) in inches.	74
E.1	Parameters (in mm) for simulate the SMWT in Zemax.	75
G.1	Parameters (in mm) for simulate the ALMA 12-m antenna in Zemax.	83
G.2	Parameters (in mm) for simulate the ALMA 12-m antenna in Zemax and the Gaussian Beam Telescope designed.	84
G.3	Parameters (in mm) for simulate the LLAMA 12-m antenna in Zemax and the Gaussian Beam Telescope designed.	85

List of Figures

1.1	Electromagnetic spectrum and the atmospheric windows.	3
2.1	Electromagnetic propagation theories.	5
2.2	Reflection and refraction.	6
2.3	Image formation using geometrical optics.	7
2.4	Scheme of ray transfer.	8
2.5	Optics versus quasi-optics focusing.	9
2.6	Gaussian beam parameters.	10
2.7	Near and far-field regions of radiation.	11
2.8	A 2-D radiation pattern of an antenna.	12
2.9	Cassegrain antenna and its main parameters.	13
2.10	Dual-mode horn.	15
2.11	Parameters of a conical corrugated horn antenna.	16
2.12	Lens geometry.	17
2.13	Paraboloid and ellipsoid geometry.	19
2.14	Heterodyne receiver: DSB, SSB, 2SB.	21
2.15	Gaussian Beam Telescope configuration.	23
2.16	Hexagonal distribution of seven pixels for a focal plane array.	24
3.1	Scheme of the proposed 7 pixel circular array.	29
3.2	SMWT in Zemax	31
3.3	SMWT. Huygens PSF for the central pixel (d=0 mm).	31
3.4	SMWT. Huygens PSF for an outer pixel (d=42.42 mm).	33
3.5	Percentage of power due to truncation and illumination efficiency (spillover and taper).	33
3.6	Seven beams at the hole of the main reflector.	34
3.7	Illumination efficiency as a function of displacement off-axis for the SMWT (using actual horn antenna).	34
3.8	SMWT. Huygens PSF for an outer pixel (d=31.54 mm).	35
3.9	SMWT. Huygens PSF for an outer pixel (d=21.63 mm).	36
3.10	Beam propagation plot on axis for the SMWT at 115 GHz.	37
4.1	Scheme of ALMA 12-m antenna and its cryostat.	43
4.2	Upper view of the actual cryostat of ALMA. 10 bands are placed in the available space.	44
4.3	Model of the optical system proposed for ALMA heterodyne receiver.	46

4.4	Huygens PSF obtained in Zemax for the central and 29.28-mm offset pixel of ALMA model.	47
4.5	Beam propagation plot on axis for ALMA's GBT at 100 GHz.	48
4.6	3-D model of the intermediate optical system designed for ALMA Band-3.	49
4.7	Mechanical model of the cartridge inside the cryostat.	49
4.8	Coupling Efficiency as a function of the displacement, tilt and offset.	50
4.9	Scheme of a Cassegrain Telescope with three possibilities of focal planes.	53
4.10	Scheme of LLAMA 12-m antenna and its cryostat.	54
4.11	Scheme of GBT designed for LLAMA 12-m antenna.	54
4.12	Huygens PSF and Wave-front function obtained in Zemax for the central and 13.01-mm offset pixel of LLAMA model.	56
4.13	Beam propagation plot on axis for LLAMA's GBT at 100 GHz.	57
4.14	3-D model of the intermediate optical system designed for LLAMA Band-3.	58
A.1	Conic sections.	68
C.1	Displacement of pixels in a hexagonal distribution.	72
C.2	Area compared to a hexagonal distribution over a single pixel.	72
D.1	Original blueprint of the horn antenna of the SMWT	74
F.1	Power through the main reflector hole of the SMWT (d=42.42 mm).	76
F.2	Power through the main reflector hole of the SMWT (d=31.54 mm).	77
F.3	Power through the main reflector hole of the SMWT (d=21.63 mm).	77
F.4	Beam Radius and Edge Taper at the secondary reflector of the SMWT as function of the beam waist w_0	78
F.5	Distribution of E for an outer pixel displaced 42.42 mm off axis and the secondary reflector border of the SMWT. Results for the current horn antenna.	79
F.6	Distribution of E for an outer pixel displaced 31.54 mm off axis and the secondary reflector border of the SMWT. Results for the current horn antenna with a thinner wall.	80
F.7	Distribution of E for an outer pixel displaced 21.63 mm off axis and the secondary reflector border of the SMWT. Results for a horn antenna with a beam waist of 6.8 mm.	81
F.8	Illumination efficiency as a function of the beam waist size and the displacement off the center for the SMWT.	82
H.1	Power through the main reflector hole of the 12-m ALMA antenna (d=58.56 mm).	86
H.2	Power at the secondary reflector of the 12-m ALMA antenna (d=58.56 mm).	87
H.3	Beam Radius and Edge Taper at the secondary reflector of the 12-m ALMA antenna as a function of the beam waist w_0	87
H.4	Distribution of E for a central and an outer pixel displaced 58.56 mm off axis and the secondary reflector border of the 12-m ALMA antenna. Results for 100 GHz and an edge taper of 10.9 dB.	88

Chapter 1

Introduction

Around the year 2025 most of the largest astronomical observatories will operate in Chilean territory. In this way Chile will concentrate 70% of the capacity of astronomical observation[1]. As examples we can mention: the *Very Large Telescope* (VLT)[2], *Atacama Pathfinder EXperiment* (APEX)[3], *Atacama Submillimeter Telescope Experiment* (ASTE)[4], *Atacama Large Millimeter/submillimeter Array* (ALMA)[5], among others, which are currently in operation. In the next years new observatories will be fully constructed and will achieve its first light: the *Large Synoptic Survey Telescope* (LSST)[6], *Cerro Chajnantor Atacama Telescope* (CCAT)[7], *Giant Magellan Telescope* (GMT)[8] and the *European Extremely Large Telescope* (E-ELT)[9].

These facilities have been attracted by the particular atmospheric and geographic conditions of the Atacama desert. For optical regime a place with no clouds, no light contamination, and good seeing is required. For millimeter and submillimeter waves a location with low H_2O vapor, high altitude (above 5000 m) and no radio interference is needed. Except for the Altiplanic Winter, there are just a few rainy days in the north of Chile, making it the driest place in the world. Moreover, the Atacama Desert has isolated, high and flat places to allocate an astronomical observatory over the thermal inversion layer with no light and electromagnetic pollution and good seeing. All of these characteristics are suitable conditions for observing in optical, millimeter and submillimeter regime during almost the complete year.

The new generation of ground-based telescopes will obtain unprecedented scientific results due to better performance in terms of sensitivity, angular resolution, and lower noise. Improving analog technology and data processing are necessary to reach this goal and this is a challenge to engineering.

Radio telescopes such as ALMA, *Large Latin American Millimeter Array* (LLAMA), CCAT, ASTE, or APEX are designed to capture millimeter and submillimeter radiation. They operate in the microwave window as can be seen in Figure 1.1. Scientific goals for such projects are cosmology, high redshift objects, galaxies, galactic nuclei, interstellar medium, star formation, astrochemistry, exoplanets, the solar system, stellar evolution and solar studies. Most of the desired targets are cold, faint and very distant sources [10].

Millimeter waves are of interest not just in astronomy, but in other applications as communications, security cameras or measuring instruments. Part of this radiation can be described as black body radiation, i.e., every body radiates in the form of microwaves according to its temperature. This kind of radiation is "visible" despite of sunlight, clothes, polymers, wood and some others.

Three radio telescopes are of specific interest for this thesis. They are the 1.2-m *Southern Millimeter Wave Telescope* (SMWT or Mini) located at Cerro Calán, the 54 12-m ALMA antennas, and the 12-m LLAMA antenna. In this thesis we propose technological improvements for these three telescopes.

The SMWT was built 35 years ago with the aim of mapping the CO $1 \rightarrow 0$ emission of the galaxy. The project was successful and results are widely used by the scientific community. Now it works for educational purposes at the Astronomy Department of the University of Chile. ALMA is the largest astronomical project in the earth, with 66 antennas working together as an interferometer. It covers the frequencies between 35 and 950 GHz, having varied scientific goals [10]. LLAMA is a 12-m single dish telescope to be located in Argentina. It is envisioned as part of a large world wide VLBI network at submillimeter wavelengths, increasing about 10 times the angular resolution achieved by ALMA [11]. It will also work as a single-dish telescope.

In radio astronomy, as well as in optic or infrared astronomy, the light is collected using reflectors and guided into a detector. Afterwards, the information is processed (filtered, amplified and digitalized). The difference between the different types of telescopes is how every sub-process is performed. For example, for the detectors, we can have bolometers or heterodyne receivers.

Bolometer receivers are incoherent or direct detectors that measure the amplitude of the received signal. The main feature is that they are broadband and do not use an LO source. They are preferable when sensitivity is more important than spectral resolution.

Heterodyne receivers are coherent detectors often used in radio astronomy. Unlike bolometers, they are capable of measuring amplitude and phase of the received signal, obtaining higher spectral resolution. The underlying principle of operation is to down-convert frequency keeping the amplitude and phase of the original wave. They are essential, for example, to resolve the velocity structure of spectral lines from cold interstellar gas [12].

Multi-pixel receivers are a way to improve performance. As sensitivity has been achieved close to the fundamental physical limit for coherent detection [12], two approaches can be taken to improve productivity. One is to increase mapping speed and the other one is to increase bandwidth of operation. Multi-pixel receivers take advantage of large focal surfaces, achieve redundancy in the case of failure of one pixel and above all, they increase mapping speed. In this way, they make more efficient the observing time. This feature is of special importance for survey telescopes.

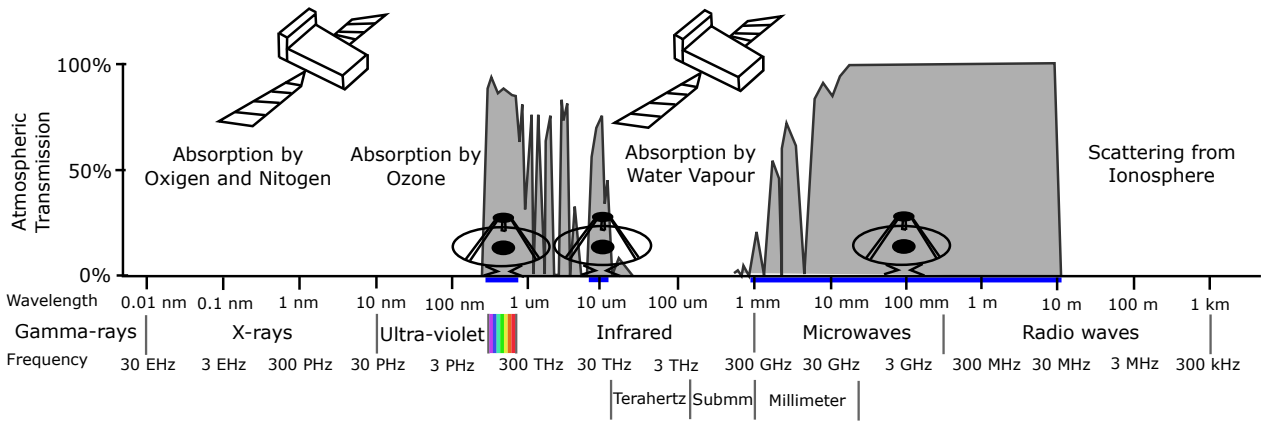


Figure 1.1: Electromagnetic spectrum and the percentage of transmission that reaches the surface of the Earth. Three atmospheric windows allow ground-based telescopes and for the other ranges it is necessary to observe over the atmosphere with space telescopes. Adapted from [13], Fig 3.2.

Cameras, i.e., receivers with multiple pixels, can be bolometric or heterodyne. As an example, CCDs are multi-pixel bolometric detectors for the optical range. However, for heterodyne cameras, there are just a few examples developed in the last 15 years. This is because the receivers are too complex. Then, adding more pixels imply higher cost, greater power consumption and the difficulty of calibrating multiple pixels at a time. Moreover, for the lower frequency range, the electronics is large enough hindering the implementation of more than one sub-detector. This thesis will focus on the study of heterodyne array receivers, specifically the optical system for such detectors. We choose to work with W band as the lower limit band for cameras due to size of the devices.

1.1 Hypothesis

The use of heterodyne cameras will be a major technological step for the new generation of radio telescopes. Focal plane arrays make possible parallel processing of pixel information. These instruments permit having the same spatial resolution and sensitivity of current instruments, but obtaining higher mapping efficiency. At the same time, they should obtain similar levels of noise temperature, efficiency, and cross-polarization. To achieve the construction of cameras, an intermediate optical system is necessary to couple the multiple beams of the receiver to the antenna.

1.2 Objectives

1.2.1 General Objective

The objective of this work is to design an intermediate optical system for a multi-pixel heterodyne receiver in the range of millimeter waves (specifically W band).

1.2.2 Specific Objectives

- A study of the feasibility of implementing a 7-pixel array receiver for the existing SMWT single-pixel will be performed.
- A 7-pixel imaging optical system will be designed for 12-m antennas such as ALMA and LLAMA. In particular, this work is of importance to the next upgrading of ALMA, which will include the possibility of cameras.
- Any design should comply with the following basic requirements:
 - Additional optical elements should have minimal addition of noise and cross polarization
 - Use two resolutions elements of pixel spacing to have acceptable values of diffraction losses and a fully coverage of sky with one sweep.
 - Gaps between pixels should be covered by multiple observations

1.3 Structure of the Thesis

This work is organized in 4 more chapters. *Chapter 2* is a bibliographic review of the theoretical concepts behind the work performed on this thesis. *Chapter 3* reports the feasibility of a multi-pixel camera in the SMWT. *Chapter 4* involves the design and simulation results for an optical system to place a camera in an ALMA and LLAMA 12-m antenna and *Chapter 5* summarize about the obtained results, conclusions and future work.

Chapter 2

Bibliographic Review

We start by presenting a basic revision on optical theory, including geometric and Gaussian optics. It is followed by a presentation of basic optical components. Finally, concepts for imaging systems and a review of existing heterodyne astronomical cameras in the range of millimeter, submillimeter and terahertz waves is presented.

2.1 Optical Theory

To explain electromagnetic propagation, different approaches are used, as shown in Figure 2.1. The simplest approach is geometric optics, while the more complex is quantum optics. The more complex the theory is, the more accurate it is, allowing to model more phenomena. For example, using geometric optics is not possible to explain diffraction, with physical optics is not possible to explain polarization and with Electromagnetic theory is not possible to explain laser noise.

For the purpose of this thesis we use geometrical optics as a first approach. Then, Gaussian optics is used for better performance description. Complete electromagnetic models are not required for the design of mirrors. They have a large computation cost and provide not additional relevant information to our problem.

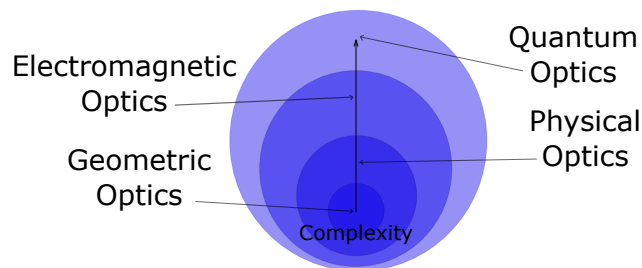


Figure 2.1: Different theories used to represent electromagnetic propagation. At the inner part is geometric optics, which is the simplest model. At the outer is quantum optics that is the most complex but explains every phenomenon, as the behavior of the photon.

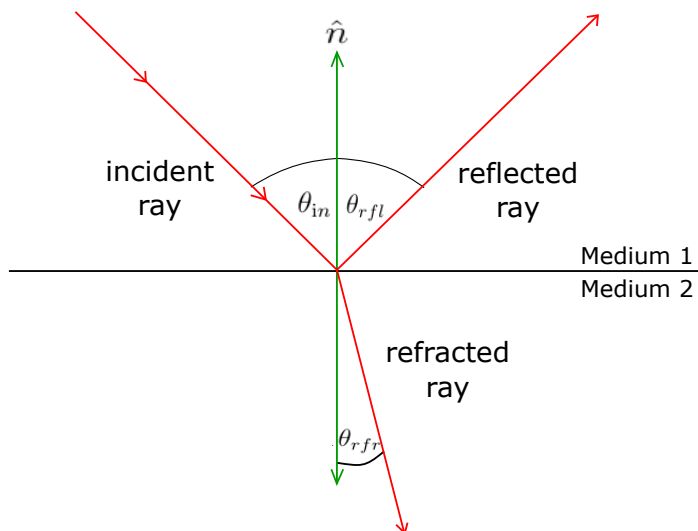


Figure 2.2: Scheme of reflection and refraction of a ray. After the incident ray hits a glossy surface, it is reflected with the same angle of incidence. When the light is transmitted to the second media, the ray changes its trajectory according to Snell's law.

2.1.1 Geometrical Optics

This approach treats the light as rays. Given a set of rules, the path of an incoming ray of light is described. Reflection and refraction are taking into account but not diffraction and interference. It is commonly used to describe systems where the wavelength is small enough compared to the devices involved.

Reflection and Refraction

The phenomena of reflection is presented schematically in Figure 2.2. The angle of the incident ray is equal to the reflected one, separated by the normal,

$$\theta_{in} = \theta_{rfl}. \tag{2.1}$$

These three vectors lay in one plane. Reflected images can be real (made with the rays) or virtual (made with the extrapolation of the rays). Mirrors and other reflector surfaces can be flat or curved.

When light passes from one medium to another with different indices of refraction, it changes its trajectory. This phenomena is described by Snell's law,

$$n_1 \sin \theta_{in} = n_2 \sin \theta_{rfr}, \tag{2.2}$$

where n_1 and n_2 are the refraction index of the medium 1 and 2, respectively, and θ_{in} and θ_{rfr} are the angle of incidence and the angle of refraction, respectively (see Figure 2.2).

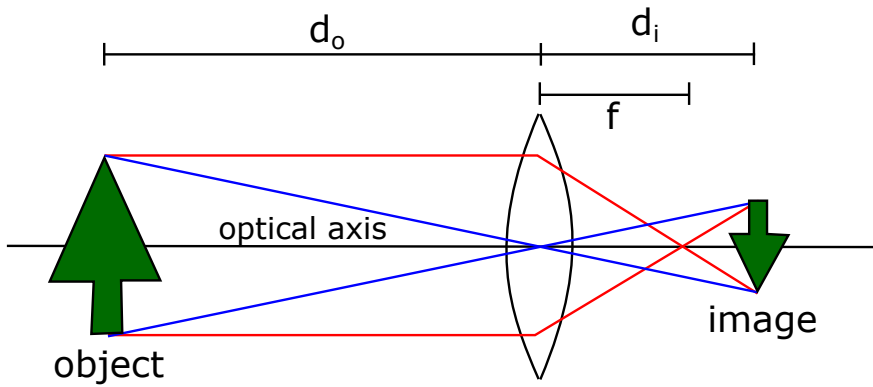


Figure 2.3: Image formation using geometrical optics. Rays are used to describe the path of light. The object and image are located at distance d_o and d_i from the optical device. The focal length of the device is f . In this case the image is reduced and inverted.

Optical Systems

Figure 2.3 shows a simple example of image formation using a lens. More complex systems are based on the same idea. Light coming from an object arrive at the optical system where it is deflected. The image is located at the plane where the rays parallel to the optical axis and the rays that passes through the center of the optical device converge. It can be magnified by the optical system. The focus is the point where the parallel rays converge. The optical system is characterized, among other parameters, by the focal length, which is the distance from the optical device to the focal point along the optical axis.

The 2×2 ABCD matrix is a relationship of the input and outcome of an optical device. In a system with multiple elements it is the combination of each transference in cascade. Given a ray in the input plane, the ABCD matrix indicates how it is deflected at the output plane. The distance from the light ray to the optical axis is x and the angle of incidence is θ , as it is shown in Figure 2.4. This two parameters are related according to:

$$\begin{bmatrix} x_{out} \\ \theta_{out} \end{bmatrix} = \begin{bmatrix} A & B \\ C & D \end{bmatrix} \begin{bmatrix} x_{in} \\ \theta_{in} \end{bmatrix}$$

PSF

A way of representing the quality of a formed image is the *Point Spread Function* (PSF), which is a measure of the spatial distribution of irradiance of a point source. The irradiance is the power received by a surface by unit area (W/mm^2). In this work we use the Huygens PSF [14].

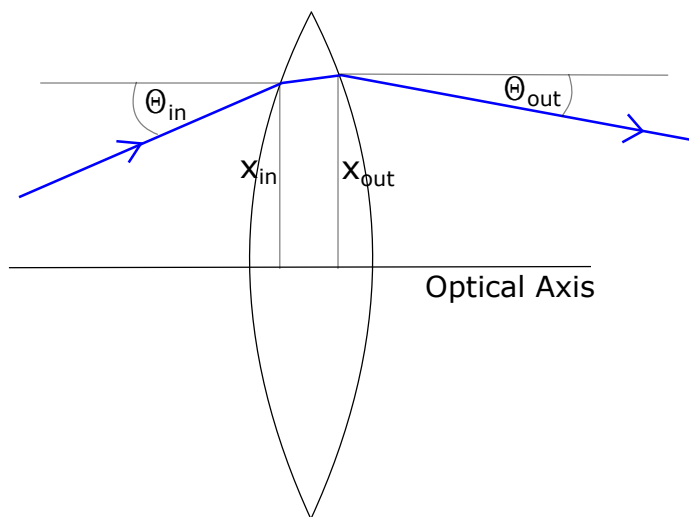


Figure 2.4: Scheme of ray transfer. The ABCD matrix relates the input parameters x_{in} , θ_{in} with the output parameters x_{out} , θ_{out} .

Strehl Ratio

A parameter used for optical systems is the Strehl ratio that is defined as "the ratio of the peak intensity of a measured point spread function (PSF) to the peak intensity of a perfect diffraction-limited PSF for the same optical system" ([15], page 504). This is a measure of optical image quality. Normally a Strehl Ratio of at least 0.8 is used to define a good model. Information about techniques and algorithms of how to calculate the Strehl ratio can be found in [15].

2.1.2 Quasioptical Theory

In between of geometrical and electromagnetic optics, physical optics allows modelling electromagnetic radiation considering diffraction effects. Although Electromagnetic theory is a complete way to study almost every kind of electromagnetic radiation it has an enormous computational cost to solve the simple problem of free space propagation.

In most millimeter and submillimeter-wave systems, the wavelength is comparable to the components involved. Therefore, geometrical optics cannot be used because it does not consider diffraction effects. Nevertheless, physical optics suffices as the radiation is represented as a reasonably well-collimated beam that is small (in wavelengths) in the direction transverse to the axis of propagation.

To represent the behavior of the radiation, the optical axes are described with geometrical optics and the beam propagation with quasioptics. Figure 2.5 is a comparison between image formation in a telescope using geometrical optics and Gaussian optics.

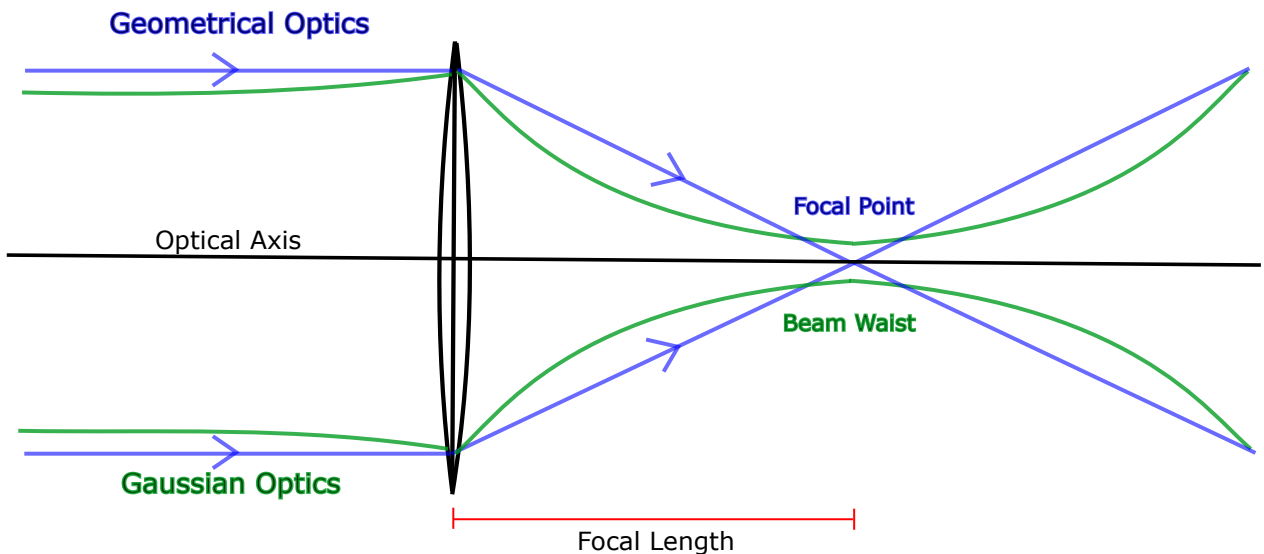


Figure 2.5: Focusing using two different approaches. Optics: the image is formed using reflection and Snell’s laws to describe light as a ray. Quasioptics: the image is formed using a Gaussian beam. Diffraction effects are considered.

Consider a plane wave where the electric and magnetic fields are mutually perpendicular and perpendicular to the direction of propagation (\hat{k}). Then, the electric field can be written as the solution of the Helmholtz wave equation as,

$$E(r, z) = u(r, z)e^{-jkz}, \quad (2.3)$$

where the time dependence ($e^{j\omega t}$) has been suppressed. $u(r, z)$ is a complex scalar function that describes the non-plane behavior, r is the radial point where E is evaluated, z is the point in the direction of propagation and $k = \frac{2\pi}{\lambda}$ is the wave number.

If we assume that the amplitude distribution u will not change abruptly over the propagation direction, and that the axial variation is small compared to the perpendicular one, we can use a Gaussian beam as a solution of the paraxial wave equation. It can be demonstrated that the angular divergence of the Gaussian beam should be confined in ~ 0.5 rad to accomplish the paraxial approximation requirements [16].

Gaussian Beam Propagation in Fundamental Mode

A Gaussian beam can be represented assuming $u(r, z)$ as a Gaussian distribution of radius $w(z)$. The propagation axis is \hat{z} and $w_0 = w(z = 0)$ is the beam waist, as shown in Figure 2.6. Using this approximation, we can define the *radius of curvature* R , the *radius* w , the *phase shift* ϕ_0 and the *edge taper* T_e , which is the relative power density of the beam at a certain radius r :

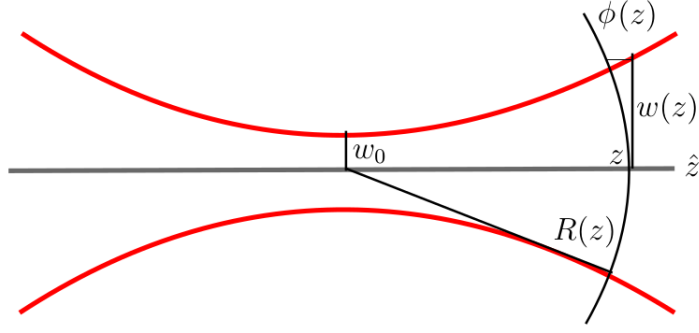


Figure 2.6: Typical parameters of an ideal Gaussian beam. The beam waist w_0 defines the shape of the beam and $w(z)$ is the radius of the beam at a certain z distance from the beam waist. $R(z)$ is the radius of curvature of the beam at z .

$$R(z) = z + \frac{1}{z} \left(\frac{\pi w_0^2}{\lambda} \right)^2 \quad (2.4)$$

$$\phi_0(z) = \arctan \left(\frac{\lambda z}{\pi w_0^2} \right) \quad (2.6)$$

$$w(z) = w_0 \sqrt{1 + \left(\frac{\lambda z}{\pi w_0^2} \right)^2} \quad (2.5)$$

$$T_e(r) = \exp \left(\frac{-2r^2}{w^2} \right) \quad (2.7)$$

With these algorithms, using cylindrical coordinates and the paraxial approximation, equation 2.3 can be rewritten for the normalized electric field distribution as:

$$E(r, z) = \sqrt{\frac{2}{\pi w^2(z)}} \exp \left(\frac{-r^2}{w^2(z)} - jkz - \frac{j\pi r^2}{\lambda R(z)} + j\phi_0(z) \right) \quad (2.8)$$

The derivation of these equations, higher order solutions and more detail about quasioptical systems and Gaussian beams can be found in [16], chapter 2.

2.1.3 Radiation Pattern

In order to measure the performance of a radiative source, its radiation pattern can be analyzed. This is a 2-D or 3-D graphical representation of the radiation properties in space coordinates. It can be linear or logarithmic scaled (often in decibels), absolute or normalized and relative to the field or the power.

Usually the far-field (Fraunhofer) zone is represented, that is, at a distance larger than $\frac{2D^2}{\lambda}$ (see Figure 2.7). Both, the co-polarization pattern and the cross-polarization can be represented in this way. This two are mutually orthogonal vectors, tangent at a radiation sphere. In most applications, the cross-polar component is minimized to avoid cross-polar talk in the system.

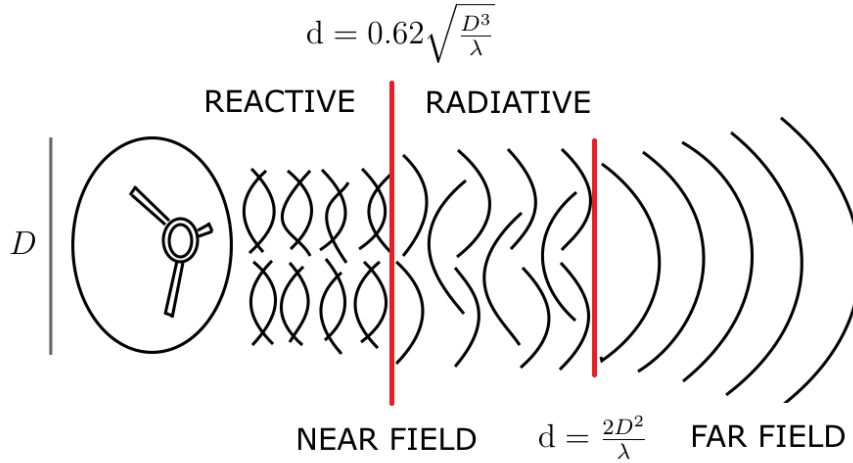


Figure 2.7: Near and far-field regions of radiation and the limit of each region. The radiative near field is also called Fresnel region and the far field is called Fraunhofer region. In the reactive near field zone, the behavior of the wave is not well described. In the Fresnel region, the behavior of the wave is predictable but does not have the characteristics of the far-field region. In the Fraunhofer region, waves are considered as having a plane-phase wavefront. The shape of the pattern is not dependent on the distance. Adapted from [17].

The radiation pattern of an antenna can be obtained in emitting or receiving mode due to the theorem of reciprocity ([18], chapter 3.8). The antenna has the same properties, no matter if it is used as emitter or receiver.

Performance Parameters

The radiation pattern presents precise information about how the antenna radiates electromagnetic energy into space. Important parameters are symmetry, directivity, bandwidth, frequency behavior, antenna efficiency, gain and presence of side lobes. In the following, we define some of the commonly used parameters. More detail about radiation pattern and radiation parameters can be found in [18], chapter 2.

HPBW: Half Power Beam Width, the width of the beam at the half of its power (0.707 of the maximum field amplitude, 0.5 of the maximum power or at -3 dB).

FNBW: First Null Beam Width, the width of the beam between the first two null points.

Directivity: It is a measure of the distribution of the power, defined as "the ratio of the radiation intensity in a given direction from the antenna to the radiation intensity averaged over all directions." [18], page 44.

Gain: It is a mixed measure of the directivity and efficiency of the antenna defined as "the ratio of the intensity, in a given direction, to the radiation intensity that would be obtained if the power accepted by the antenna were radiated isotropically." [18], page 66.

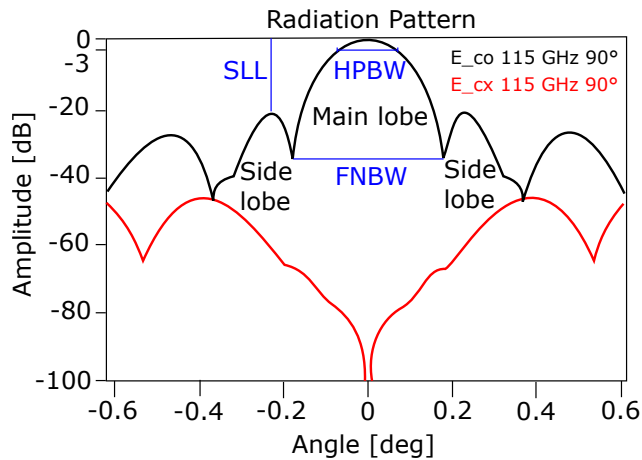


Figure 2.8: A typical 2-D radiation pattern of an antenna and its main components. This pattern corresponds to a directional antenna with a narrow main lobe and side lobes at a low level of amplitude. It is common to normalize to the maximum amplitude.

Bandwidth: It is defined as "the range of frequencies within which the performance of the antenna, with respect to some characteristic, conforms to a specified standard." [18], page 70.

Return Loss: It is a measure of the reflection in a device, defined as the ratio of the amplitude of the reflected wave to the incident one.

SLL: Side Lobe Level, is a measure of the relative amplitude of the side lobes compared to the main one, defined as the difference (in dB) of the maximum of the main lobe and the first side lobe.

Figure 2.8 shows a typical radiation pattern of a horn antenna. Appears the E-copolar, H-copolar fields, and the cross-polar or Xpolar. For astronomy applications, this patterns are very directive, with low side lobes and good symmetry. Moreover, the Xpolar pattern should be extremely low.

2.2 Optical Devices

In this section we summarize the main concepts of the optical devices involved in this work: Cassegrain antennas, horn antennas, lenses and mirrors for microwaves. This three optical devices are necessary to receive the signal: reflectors of a Cassegrain antenna concentrate the radiation into the focal point. Usually a set of lenses and mirrors are used to redirect the input radiation into a horn antenna, which concentrate the radiation into the electronic detector.

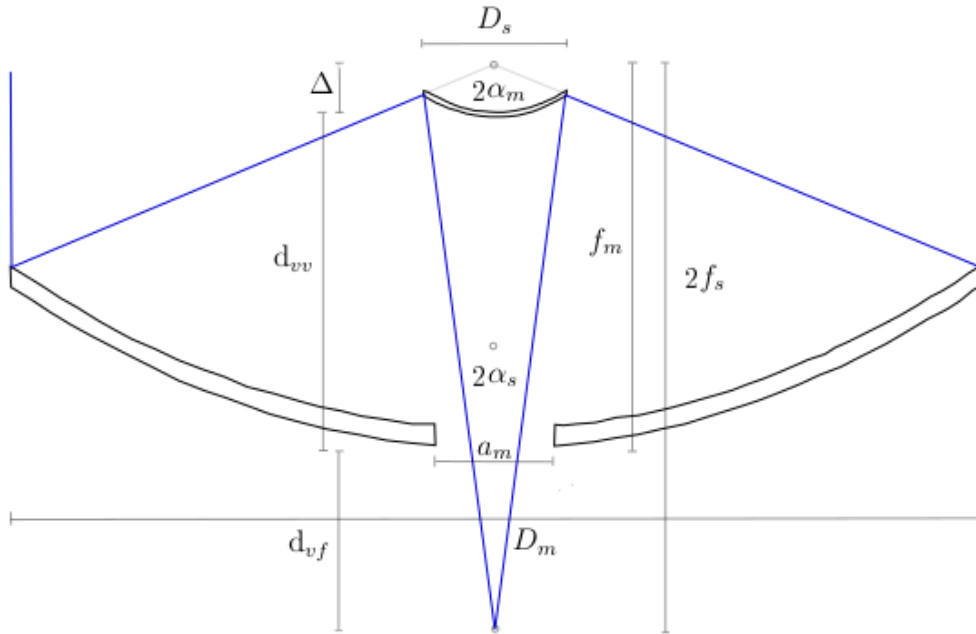


Figure 2.9: A typical configuration for a Cassegrain antenna and its main parameters. It is composed by two reflectors that focus the signal into a feed placed in the focal point. A hole in the main reflector allows the light pass to the focal point placed behind the reflector. D_m and D_s are the diameters of the main and secondary reflector, a_m is the central aperture in the main reflector, f_m and f_s are the focal distances of the main and secondary, α_m and α_s are the half-angle of aperture for the main and secondary, Δ is the distance between the vertex of the secondary and the focal point of the main, d_{vv} is the distance between vertices of the reflectors and d_{vf} is the distance between the vertex of the main reflector and the focal (feed) point.

2.2.1 Cassegrain Antennas

This antenna is a combination of two reflectors: a large primary with parabolic shape, and a smaller secondary with a convex hyperbolic shape. This design is adapted from the Cassegrain Telescope invented in 1672 by Laurent Cassegrain. The secondary is placed to have its focus coincide with the primary focus. The feed antenna is placed on the other secondary focus. The system acts as a major telescope (larger effective focal length, bigger field of view) but reducing the spacing between reflectors. The feed antenna and all the electronics (a very massive and voluminous system) can be mounted behind the main reflector. More about reflectors in [18], chapter 15.

Incoming radiation arrives approximately as a well-collimated beam. Therefore, after it impacts at the main reflector, the rays would go directly to the focus. However, before that, the secondary reflector sends the rays to its own focus where a feed antenna is located.

The main parameters of a Cassegrain reflector are presented in Figure 2.9. Not all parameters are independent and equations 2.9 - 2.16 relates some of them [19]. f_{eq} is the equivalent focal distance of the Cassegrain antenna. F_{eq} is the f number, it characterizes the light-gathering power of the optical system. M is the magnification, a dimensionless factor that quantifies how much the image is reduced in the telescope. $e_m = 1$ and $e_s > 1$ are the eccentricity of the the primary and secondary and θ_{min} is the angular resolution of the telescope ([13], eq 3.3).

$$\alpha_m = \arctan \left(\left(\frac{4f_s}{D_s} - \cot \phi_0 \right)^{-1} \right) \quad (2.9) \quad M = \frac{f_{eq}}{f_m} \quad (2.13)$$

$$\alpha_s = 2 \arctan \left(\frac{D_m}{4f_m} \right) \quad (2.10) \quad e_s = \frac{M + 1}{M - 1} \quad (2.14)$$

$$f_{eq} = \frac{D_m}{4} \cot \left(\frac{\alpha_0}{2} \right) \quad (2.11) \quad \Delta = f_s \frac{e_s - 1}{e_s} \quad (2.15)$$

$$F_{eq} = \frac{f_{eq}}{D_m} \quad (2.12) \quad \theta_{min} = 1.22 \frac{\lambda}{D_m} \quad (2.16)$$

Aperture Efficiency

As a measure of performance, a commonly used parameter is the aperture efficiency. It is defined as "the ratio of the effective area to the physical area of the antenna" ([16], page 129). A good system is characterized by an aperture efficiency above 80%. In a Cassegrain antenna illuminated by a feed antenna in the focus, the aperture efficiency can be calculated as the multiplication of the taper efficiency, the spillover efficiency, and the blockage efficiency, which are its main components.

Taper efficiency is a measure of the coupling over the antenna. Spillover efficiency is a measure of the power intercepted by the antenna aperture compared to the power at the whole aperture plane. Blockage efficiency is a measure of how much area of the primary reflector is shadowed by the secondary. Taper and spillover efficiency re given by

$$\eta_t = \frac{|\iint_{ap} E_a dS|^2}{\iint_{ap} |E_a|^2 dS \iint_{ap} dS} \quad (2.17) \quad \eta_s = \frac{\iint_{ap} |E_a|^2 dS}{\iint_{ap-plane} |E_a|^2 dS} \quad (2.18)$$

where the subscript ap denotes the integrals are over the aperture and $ap - plane$ that they are considered over the complete aperture plane. E_a is the electrical field ignoring phase shift.

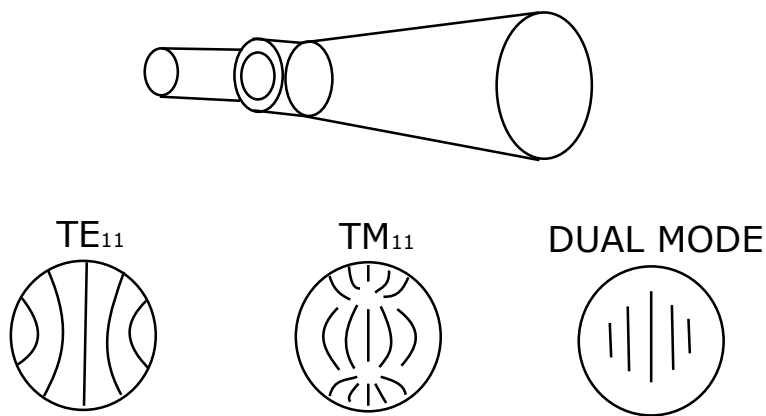


Figure 2.10: Dual-mode conical horn and its approximate aperture field distribution. Adapted from figure 15.14 of [20].

Illumination efficiency is a value used for this thesis and refers to the aperture efficiency for the secondary reflector. It is computed as the multiplication of the taper and spillover efficiencies,

$$\eta_{ill} = \eta_t \eta_s |_{secondary}. \quad (2.19)$$

As it is explained in [16], chapter 6.3, the optimum efficiency, 0.82, is obtained with an edge taper of 10.9 dB. A big edge taper will reduce side lobes but if it is too high, taper efficiency is low. On the other hand, if the edge taper is too small, the efficiency is lost due to spillover.

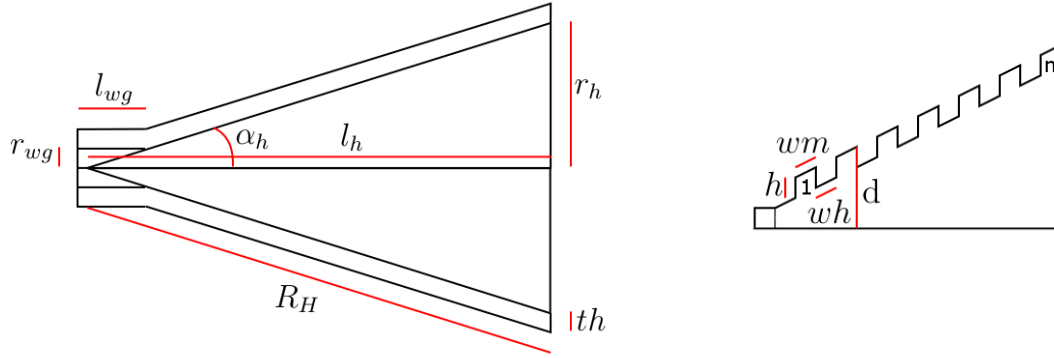
2.2.2 Horn Antennas

A horn antenna is a device designed as a transition between free space and a confined wave propagation. In most radio telescopes the feed antenna is located at the receiver, usually inside a cryostat, to minimize its noise contribution.

They have circular or rectangular aperture and its shape is varied, according to the required pattern. The dual-mode and the conical corrugated horn antennas have the most axially-symmetric pattern and low levels of cross-polarization. The Huygens principle is used to characterize the radiation properties.

Dual mode conical horn

The dual mode conical horn has a mixture of transversal electric and magnetic mode (see Figure 2.10). The inner radius must be large enough to allow TE_{11} and small enough to not allow TM_{11} . The second radius must be of a size that allows TM_{11} and not TE_{12} . The TM_{11} and TE_{11} cancel the ϕ component to have an axially symmetric and low cross-polarization pattern.



(a) A typical conical horn antenna (lateral cut) and (b) Details of the corrugations of a conical horn antenna (lateral cut).

Figure 2.11: Parameters of a conical corrugated horn antenna. r_{wg} and r_h are the radius of the waveguide and the horn aperture, l_{wg} and l_h are the longitude of the waveguide and the cone. α_h is the half angle of aperture, R_H is the slant longitude of the cone and th is the total thickness of the horn, including corrugations. h is the depth of the corrugations, d is the radial high of the corrugations, wm and wh are the length of the taken part and the not-taken. n is the total number of corrugations.

Conical corrugated horn

By using a corrugated wall, an hybrid mode propagation is forced. Transversal electric and magnetic mode propagate together with a unique common velocity. The mixture of modes TE_{11} and TM_{11} in a combination of $\sim 85\%$ and $\sim 15\%$ respectively is known as the hybrid mode HE_{11} . The corrugations imply different reactances in azimuthal (X_ϕ) and axial (X_z) directions. While $X_z \rightarrow \infty$, $X_\phi \rightarrow 0$ and the components become locked in the hybrid mode. As a result, an axially-symmetric radiation pattern with low side-lobe level and low cross-polar component in a wide frequency range is obtained.

Figure 2.11 presents a scheme of a conical corrugated horn antenna and its main parameters. More information about horn antennas theory can be found in [20], chapter 15. In chapter 15.4 there are details about the dual mode conical horn and in 15.5 about conical corrugated horns.

2.2.3 Focusing Elements: Lenses and Mirrors

Lenses and mirrors (or reflectors) are optical devices that change the direction and properties of a ray of light. Reflection and refraction laws are used to describe the path and geometric relationships for each figure are used to define the shape of the device.

At microwave regime, as the wavelength is much greater than in optics, the surface can be mechanically machined because the accuracy is in the order of the wavelength. These devices are made of other materials than in visible optics. Typically used materials for lenses are High Density Polyethylene (HDPE) or Polytetrafluoroethylene (PTFE) commonly called Teflon. Reflectors are usually made of aluminum or copper. By coating the mirrors with silver or

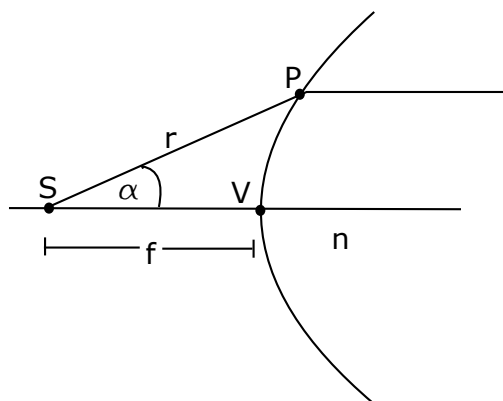


Figure 2.12: Single surface lens geometry. The lens collimates rays emanating from the point source S a distance f away from the lens vertex V. Adapted from figure 5.1 of [16].

gold the reflection efficiency is improved. Design of such components is done with the use of geometrical optics. Additional considerations are used to include diffraction and polarization effects. To avoid diffraction due to the finite size of the optical components a diameter of $5w$ is recommended.

Lenses

Lenses are refractive focusing elements composed by a dielectric (chapter 5.4 and 5.5 of [16], chapter 16 of [20]). For microwave it is common the use of hyperbolic lenses according to

$$r = \frac{(n - 1)f}{n \cos \alpha - 1} \quad (2.20)$$

(see Figure 2.12 and Appendix A for conic formulas). To get the rays directed to the hyperbola focus, it is required that the eccentricity of the hyperbola is equal to the refractive index of the lens ($e = n$)[16]. Other important parameter to describe the hyperbola is the focal length $f = a(1 + e) = a + c$, where a is the distance from the center to the vertex of the hyperbola and c is the distance from the center to the focal point of the hyperbola. For an ellipsoidal lens the same idea is maintained, but the eccentricity of the ellipse is equal to the inverse of the refractive index of the lens ($e = 1/n$)[16].

The dielectric produces loss due to the material absorption. This depends on the thickness so it is desirable to have a thin lens. In [16], Table 5.1 there are examples of materials with its refractive index and loss tangent for the frequency measured.

The use of anti-reflection coating is common to avoid undesirable reflections. It can be implemented with the use of corrugations. Advanced designs using *zoning procedure*, minimizing the losses due to the absorption in the dielectric. As a counterpart, these procedures could reduce the bandwidth of operation, gain and increase side lobes.

Mirrors

Mirrors are reflective focusing elements made of a smooth surface of a metallic material (chapter 5.8 of [16], chapter 17 of [20]). They have less absorptive and reflective loss than lenses. The typical shapes used are ellipsoidal and paraboloidal. For example, in a Cassegrain antenna, paraboloidal and hyperboloidal shapes are used jointly. They can be constructed using direct metal machining and polishing. It is usual to use mirrors off-axis, with the consequence of producing beam distortion and adding cross-polarization. Nevertheless, this disadvantages are of less impact than the use of lenses.

In a paraboloidal mirror a ray parallel to the optical axis is deflected passing through the focal point of the parabola (see Appendix A). A paraboloid with the origin at the vertex (Figure 2.13a) can be described as

$$z = \frac{x^2 + y^2}{4f_p}. \quad (2.21)$$

In an ellipsoidal mirror a ray that passes through one of the focal points is deflected passing through the other focal point of the ellipse. An ellipsoid with the origin in the center of the ellipse (Figure 2.13b) can be described as

$$\frac{x^2 + y^2}{b^2} + \frac{z^2}{a^2} = 1. \quad (2.22)$$

To evaluate the beam distortion two coefficients are of great interest. The distortion due to reflection

$$K_f = 1 - \frac{w_m^2 \tan \theta_i}{8f^2}, \quad (2.23)$$

and due to cross-polarization

$$K_{co} = 1 - \frac{w_m^2 \tan^2 \theta_i}{4f^2}. \quad (2.24)$$

Both are a function of the beam radius at the optical device reference plane w_m , the angle of incidence θ_i and the focal length f .

Other consideration is the surface accuracy, which must be with an error less than 0.01λ to have a good transmission factor. The losses in the material can be minimized using those with low resistivity. Gold plating is regularly used.

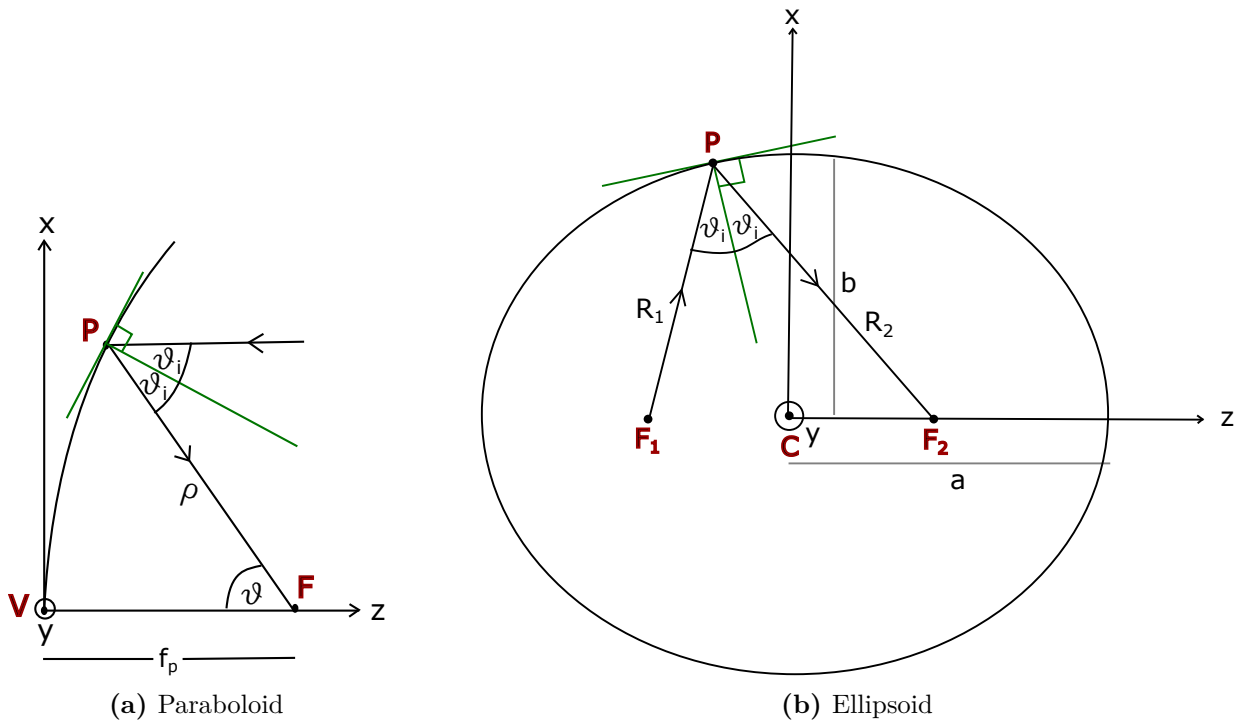


Figure 2.13: Paraboloid and ellipsoid reflectors geometry. Paraboloids have only one focal point (F) while ellipsoids have two (F_1 and F_2). θ_i is the incidence angle. f_p is the focal length of the parabola. a and b are the semi-major and semi-minor axes of the ellipse, respectively. Adapted from figure 15.17 and 15.18 of [16]

ABCD Matrix for Gaussian Beams

The ABCD matrix concept is inherited from optical theory to Gaussian-optics. Instead of using the position and angle of incidence as input and output we have the position and slope of the beam such that,

$$\begin{bmatrix} r_{out} \\ r'_{out} \end{bmatrix} = \begin{bmatrix} A & B \\ C & D \end{bmatrix} \begin{bmatrix} r_{in} \\ r'_{in} \end{bmatrix}$$

where r_{in} and r_{out} are the positions of start and end of the ray and r'_{in} and r'_{out} the slope over that position. Using this we can find d_{out} and w_{0out} , the position and size of the beam waist as output of the optical device, as

$$d_{out} = -\frac{(Ad_{in} + B)(Cd_{in} + D) + ACz_c^2}{(Cd_{in} + D)^2 + C^2z_c^2} \quad (2.25)$$

$$w_{0out} = \frac{w_{0in}}{\sqrt{(Cd_{in} + D)^2 + C^2z_c^2}}. \quad (2.26)$$

The analysis for lenses is analogous for mirrors, the difference is that in lenses the radiation passes through the other side and with mirrors the radiation bounce back.

This model does not take into account absorptive and reflective losses and cross-polarization, so they must be considered apart. Moreover, optical devices can produce higher order beam modes that should be considered.

Two examples of ABCD matrix with interest for this thesis are presented below. They are obtained by multiplication of simpler ABCD matrix, as the one for uniform material propagation and the one for interface between different media. More examples in Appendix B. The ABCD Matrix for a biconvex thick lens is

$$\begin{bmatrix} A & B \\ C & D \end{bmatrix} = \begin{bmatrix} 1 + \frac{d(n_2 - n_1)}{n_2 R_1} & d \frac{n_1}{n_2} \\ -\frac{n_2 - n_1}{n_1} \left(\frac{1}{R_2} - \frac{1}{R_1} \right) - \frac{d(n_2 - n_1)^2}{n_1 n_2 R_1 R_2} & 1 - \frac{d(n_2 - n_1)}{n_2 R_2} \end{bmatrix}$$

We consider that the ray arrives from a media of refractive index n_1 to a media of refractive index n_2 . R is the radius of curvature of the corresponding surface and d is the thickness of the lens. The ABCD Matrix for a special configuration named Gaussian Telescope, to be presented in detail in section 2.4.1, is

$$\begin{bmatrix} A & B \\ C & D \end{bmatrix} = \begin{bmatrix} -\frac{f_2}{f_1} & f_1 + f_2 \\ 0 & -\frac{f_1}{f_2} \end{bmatrix}$$

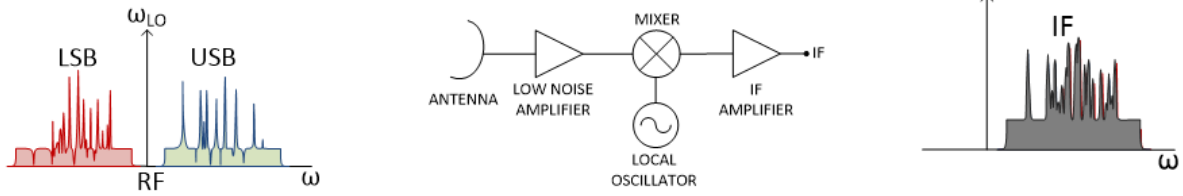
where the first device has a focal length f_1 and the second f_2 . They are separated by a distance equals to $f_1 + f_2$.

2.3 Heterodyne Receivers

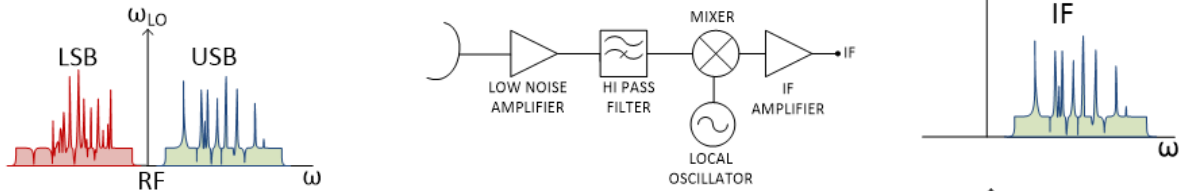
A telescope collects the light and guides it into a device where it is detected by an electronic sensor. When high spectral resolution is required, a heterodyne receiver is used. This type of receiver senses, amplifies and down-converts an originally faint high-frequency signal. The output signal have the same basic features as the input signal, but it is ready to be processed by further low frequency stages. Heterodyne receivers are not just used in astronomy. In fact, they were invented during World War I [21] and have been used ever since in different areas of telecommunications, remote sensing and radio astronomy.

The heterodyne receiver is a coherent detector that is able to maintain phase and amplitude of the original signal but at a desired lower frequency called Intermediate Frequency (IF). A scheme of three types of heterodyne receiver is shown in Figure 2.14. The electromagnetic wave is collected by an antenna. Usually, the process involves Low Noise Amplifiers (LNA) to amplify a faint signal adding minimal noise. Then, the signal is mixed with a local signal called Local Oscillator (LO) obtaining a mix of signals. Afterward, it is filtered and only the desired part of the spectrum is obtained, which is usually amplified again. The IF signal

Double Side Band (DSB)



Single Side Band (SSB)



Side Band Separation configuration (2SB)

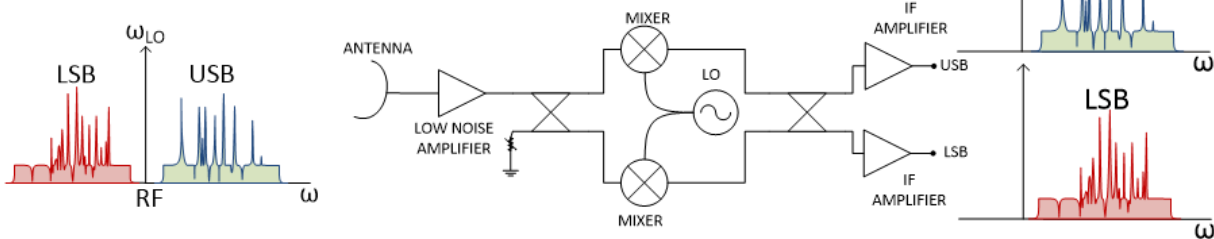


Figure 2.14: Scheme of a double side band (DSB), single side band (SSB) and side-band separation (2SB) heterodyne receiver [24]. Using DSB receivers the intermediate frequency signal (IF) is a mixing of upper (USB) and lower side band (LSB) signals. Using SSB receivers the IF is just the USB because of the high pass filter. Using 2SB receivers both sides are obtained in two different IF signals. This is the more complete but the more complex system.

contains the information about amplitude and phase of the original incident wave but in a lower frequency. The complete process adds the minimum noise possible (they are noise-limited detectors). More information about mixers, low noise amplifiers, and filters can be found in [22], chapters 13.5, 12.3 and 8 respectively, and more about receivers in [23], chapters 4 and 5.

2.3.1 Noise Temperature

The noise temperature of a device is a measure of the noise that is added by the device to the signal. For faint sources, it is important to minimize this parameter in order to be able of distinguishing the signal of the noise. For this reason, in the first stage, the electronic devices are usually cooled inside a cryostat. For a system with N stages, the noise temperature can be calculated as

$$T_{cas} = T_{e1} + \frac{T_{e2}}{G_1} + \frac{T_{e3}}{G_1 G_2} + \dots + \frac{T_{eN}}{G_1 G_2 \dots G_{N-1}}. \quad (2.27)$$

The noise temperature of each element is divided by the gain of previous elements. The minimum addition of noise should be in the first stage. More information about how to measure the noise temperature of a device in [22], chapter 10.1.

2.4 Imaging Systems

In particular, let us consider imaging systems composed of one reflector antenna, a system of lenses and mirrors and a heterodyne receiver with a horn feed. In such systems, the telescope focal plane will concentrate the power of the received signal of the sky. Then, the signal is relocated at the imaging focal plane where the receiver array is located.

In order to have a good performance, some restrictions must be taken into account. The feed horn should be small enough to be placed inside the cryostat and to have a small beam radius at the cryostat window to reduce its size. To achieve this, the feed horn must be designed to have a waist close to its aperture. Nevertheless, to maximize aperture efficiency a particular waist is needed. The beam of the source should be matched to the beam of the feed horns in the receiver. Lenses and mirrors are used to guide and transform the beam properties, a process known as *mode matching*. It is often preferred the use of mirrors as the lens involve losses in the dielectric adding noise to the system. On the other hand, mirrors add distortion and cross-polarization as well.

In multi-pixel we also deal with maximizing aperture efficiency and minimizing distortion and cross-polarization not just for the central pixel but also the lateral ones. For that reason, multi-pixel design is more complex. An additional restriction is that the multiple beams must be at an image of the pixels in the receiver. The optical axes must be parallel and keep the positions in the entrance and exit of the intermediate quasi-optical system. This will allow to have a *focal plane array*, an array of receivers located in the focal plane, that generate an image of the sky.

We will use the fundamental Gaussian beam mode. The beam radius and radius of curvature (w and R respectively) are not mode dependent. The only parameter that could change is the phase shift (ϕ) (information about higher order modes in [16], chapter 2.4).

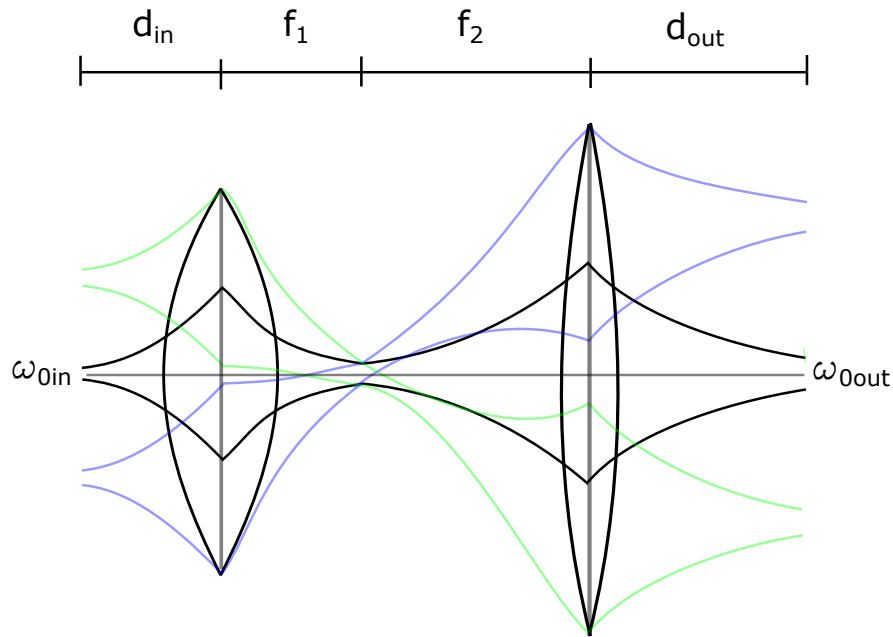


Figure 2.15: Gaussian Beam Telescope configuration. The magnification is $M = f_2/f_1$. Offset beams have the same propagation properties than the central beam.

2.4.1 Gaussian Telescope

Unlike single-pixel receivers, the need to form an image restricts the use of optical devices. One option is to use a Gaussian beam telescope ([16], chapter 3.3.3), where two devices with focal lengths f_1 and f_2 are used. They are separated by a distance equals to $f_1 + f_2$. The input beam waist is at d_{in} from device 1 and the output beam waist is at d_{out} from device 2, as shown in Figure 2.15. A particular case is to choose $d_{in} = f_1$. Then, the output beam waist is at the focal plane (f_2) of the second device. The magnification is calculated as $M = f_2/f_1$ for any case and represents the scaling factor for the beam spacing and the waist size.

In this configuration, the beams at the exit are collimated and also the position and magnification of the beam waist is frequency independent. This device has the property of re-image. The beam waist and spacing between pixels at the input of the Gaussian Beam Telescope are amplified by M towards the output. This wide bandwidth is very useful at imaging systems in which the scientific interest is not just in a particular wavelength.

Despite the fact that they are designed to work on axes, for space criteria, in some cases it is necessary to compact them. In off-axes configuration, the performance may not be the same. Examples and useful criteria to design Gaussian telescopes can be found in [25].

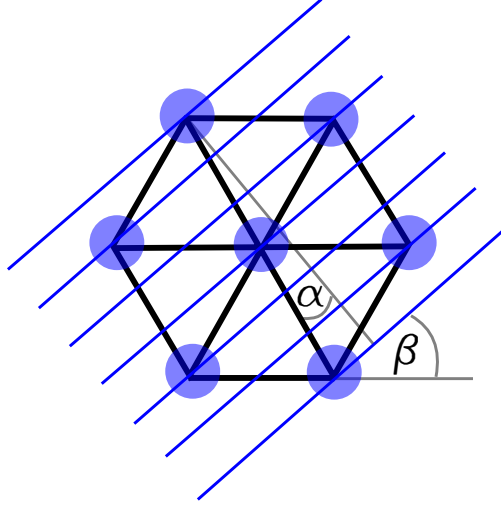


Figure 2.16: Hexagonal distribution of seven pixels for a focal plane array. Each of the seven pixels is located at the vertices and the center of the hexagon. The sweep is performed at an angle $\beta = 40.89^\circ$ from the horizontal to allow a maximized coverage. $\alpha = 10.89^\circ$.

2.4.2 Pixel distances

Using the criteria of separating the pixels in a distance of at least $s_{min} = 3w_0$, we assure acceptable levels of diffraction at each pixel. An object of size s in the focal plane is seen of angular size θ in the sky, according to

$$s = f_{eq} \tan(\theta) \approx f_{eq}\theta, \quad (2.28)$$

where f_{eq} is the equivalent focal length of the system ([13], eq 3.1). It can be demonstrated that this minimum size s_{min} corresponds to an angular size of $2\theta_{min}$ in the sky, where θ_{min} corresponds to the angular resolution of the telescope ([12], Chapter 4.1). Then, the minimum distance to allocate the second pixel is given by

$$s_{min} = f_{eq} \tan(2\theta_{min}) \approx f_{eq}2\theta_{min}. \quad (2.29)$$

After accomplishing that restriction we want to minimize the distances between beam waists to maximize the area that is covered in one scan. As the rule is to use approximately $2\theta_{min}$ some area will not always be covered. This implies that multiple observations must be taken to fully cover an area of the sky.

2.4.3 Pixel distribution

One option to maximize the use of multiple pixels in a focal plane is to distribute them in a hexagon, as shown in Figure 2.16. This configuration is used in the designs presented here because it keeps the use of a central pixel. It also allows a soften mapping process *on the fly*. If a continue integration is performed, the pixels appears extended but it can be corrected later on by performing a new scan in the perpendicular direction. This configuration can be made with pixels not as close as in other configurations. Consequently, the feeds can be more separated in the cryostat and more flexibility of design is allowed.

While a single pixel covers an angle of θ_{min} , this configuration covers $7\theta_{min}$. If the spacing between pixels is chosen to be $2\theta_{min}$, it can be demonstrated that the sweep width is $4.91\theta_{min}$. Thus, if the same sweep velocity is used, the hexagonal distribution covers an area approximately 5 times bigger, in other words, the mapping is 5 times faster. If we do not consider filling the area, in one shot the hexagonal configuration covers an area about 25 times larger than a single pixel (see Appendix C for more details).

2.5 Revision of Existing Focal Plane Arrays

As it was described above, astronomical cameras with bolometric detectors have been developed since many years in CCD detectors and in lesser amount in millimeter and submillimeter arrays. Nevertheless, heterodyne arrays is a less explored area because the complexity and size of the devices is an obstacle at the time to develop multi-pixel technology.

In the following, there is a review of existing cameras in the millimeter, submillimeter and terahertz regime, based on [12]. This will just involve heterodyne receivers, bolometers are excluded because is not the topic of this thesis. Millimeter regime is considered above 30 GHz and under 300 GHz, beyond that frequency we name it submillimeter and terahertz.

All of the instruments presents different properties. Some of the examples present dual polarization while others just one. Systems use different technology, as HEMT or SIS. The geometry of the array could be square or circular and are installed in different kinds of telescopes in different places around the world.

2.5.1 Submillimeter and Terahertz Regime

Table 2.1 shows 8 examples of submillimeter cameras developed since the year 1998, and 2 examples of terahertz cameras since 2009. Just two terahertz cameras have been deployed, meanwhile, others as STO-2 are under development. The only example which passes the barrier of 16 pixels is SuperCam, one of the newest ones.

Submillimeter cameras have had more instances to be tested, CHAMP and CHAMP+, of the Max-Planck-Institut für Radioastronomie, PoleStar, DesertSTAR, SuperCam and KAPPA, of a consortium of institutes and universities including University of Arizona, Caltech, Universität zu Köln, Harvard-Smithsonian, JPL, University of Virginia and University of Massachusetts, HARP, of University of Cambridge, UK Astronomy Technology Centre, Joint Astronomy Centre, Herzberg Institut of Astrophysics and Delft University of Technology and SMART of the Universität zu Köln.

Table 2.1: Review of existing submillimeter and terahertz heterodyne arrays.

Instrument	Installed at (year)	Frequency	Pixels	Reference
CHAMP	Caltech Submm Observatory, 1999	480 GHz 625 μm	16	[26]
CHAMP+	APEX, 2007	660 - 850 GHz (455 - 353 μm)	14	[27]
DesertSTAR	HHT	345 GHz (870 μm)	7	[28]
HARP	James Clerk Maxwell Telescope, 2005	325 - 375 GHz (923 - 800 μm)	16	[29]
KAPPA	–	660 GHz (455 μm)	16	[30]
PoleStar	AST/RO, 2000	800 - 820 GHz (375 - 366 μm)	4	[31]
SMART	KOSMA 3 m, 2001 / NANTEN2, 2008	490 GHz (612 μm) 810 GHz (370 μm)	8 8	[32]
STO receiver	STO, 2009	1.46 THz (205 μm) 1.9 THz (158 μm)	4 4	[33]
SuperCam	HHT, 2010	350 GHz (857 μm)	64	[34]
upGREAT	SOFIA, 2016	1.9 - 2.5 THz (158 - 120 μm) 4.7 THz (120 μm)	14 7	[35]

2.5.2 Millimeter Regime

Table 2.2 presents ten examples of millimeter cameras developed since the year 2000. It has to be noticed that most of the developments have been deployed during the last few years. As the submillimeter and especially the terahertz regime, millimeter heterodyne cameras are a new piece of technology that needs to be improved. Of the examples shown, four of them are developed for W-band as the project of this thesis. However, only Argus uses current technology as the other three are around 15 years old.

The instrument listed are from different institutes and universities. Argus of Stanford University, Caltech, NRAO, JPL, University of Miami and University of Maryland, BEARS of Nobeyama Radio Observatory, HERA and the other IRAM's receivers are from IRAM and LAOG, KFPA of the Green Bank, Sardinia of the Istituto di Radioastronomia di Bologna, the Cagliari Observatory and the Arcetri Astrophysical Observatory, SEQUOIA of the FCRAO.

There is also more examples at lower frequencies, as the 13 beams and 7 beams for Parkes 64-m, 4 beams for Lovell 76-m, 7 beams ALFA for Arecibo 305-m and others, but all of them operates lower than 18 GHz (under K band), and are not the topic of this work.

Table 2.2: Review of existing millimeter heterodyne arrays.

Instrument	Installed at (year)	Frequency	Pixels	Reference
Argus	Green Bank Telescope	85 - 116 GHz (3.53 - 2.59 mm)	16	[36]
BEARS	NRO 45m Telescope	82 - 116 GHz (3.66 - 2.59 mm)	25	[37]
HERA	IRAM 30 m, 2001	215 - 270 GHz (1.40 - 1.11 mm)	9	[38]
IRAM 30 m receiver	IRAM 30 m, 2009	129 - 174 GHz (2.37 - 1.72 mm)	4	[39]
IRAM 30 m receiver	IRAM 30 m	80 - 116 GHz (3.75 - 2.59 mm)	25	[40]
KFPA	Green Bank Telescope	18 - 26.5 GHz (16.67 - 11.32) mm	7	[41]
Sardinia K-band	Sardinia	18-26 GHz (16.67 - 11.54 mm)	7	[42]
Sardinia Q-band	Sardinia	33 - 50 GHz (9.09 - 6.00 mm)	19	[42]
SEQUOIA	FCRAO 14m telescope / GTM, 2016	85 - 115.6 GHz (3.53 - 2.60 mm)	16	[43]

2.6 Summary

We have presented the theoretical framework required to described and support the design of optical devices for heterodyne cameras. Additionally, we have reviewed the existing astronomical heterodyne cameras for millimeter, submillimeter and terahertz waves.

Chapter 3

Feasibility of a Camera in the SMWT

In this chapter we study the feasibility of replacing the single-pixel receiver of the 1.2-m SMWT by a camera of 7 pixels. Two basic guidelines that we follow during the development of the project are (i) avoiding the use of additional optical devices and (ii) keeping a system with a pixel located on the telescope optical axis, as in the configuration shown in Figure 3.1. The design was done using geometrical optics.

3.1 Brief History of the SMWT

The *Southern Millimeter-Wave Telescope* (SMWT), also known as Mini, is a radio telescope for 85-115 GHz. It was built at Columbia University in 1980 with the objective of mapping the CO emission in the galaxy through the $1 \rightarrow 0$ spectral line emission. This transition emits radiation at 115 GHz and the telescope is optimized for that frequency. Two identical telescopes were developed, one installed in the northern hemisphere (NMWT), in Columbia University's Pupin Physics Laboratory and one in the southern hemisphere, specifically in the Cerro Tololo Inter-American Observatory (CTIO) and operated by the Astronomy Department of the University of Chile together with Harvard and Columbia University [44][45].

After more than 15 years of scientific observations it ceased operations in 2005. Its receiver was moved to the (Chilean) National Astronomical Observatory in Cerro Calán to be upgraded and to measure the opacity of the sky. Finally, in 2009, the whole telescope was relocated at Cerro Calán. Since then, different parts of the system have been modified and upgraded as part of undergraduate [45][46][47][48][49][50] and graduate theses [51][52].

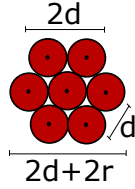


Figure 3.1: Scheme of the proposed 7 horn antennas in the receiver (upper view) as a circular array with a central pixel. d is the distance between the center of each pixel and r the outer radius of the horn feed.

3.2 Description of the Antenna

The Mini is a Cassegrain antenna with an heterodyne single-pixel receiver and a corrugated feed horn. Table 3.1 shows the values of the optical parameters of the Mini, calculated using equations (2.9) to (2.15). Table 3.2 presents the values for the feed antenna obtained from the original drawings [53]. In Appendix D we present the original values in imperial units. For this work we focus on the target frequency of CO $1 \rightarrow 0$ emission (115 GHz), that has an edge taper of 12.55 dB.

Table 3.1: Main parameters of the Cassegrain antenna of the SMWT (Mini). See Figure 2.9 for definitions. D is the diameter of the reflector, a is the diameter of the hole in the main reflector, f is the focal length, F is the ratio f/D , e is the excentricity of the reflector, α is the half angle of aperture, M the total magnification of the reflectors, Δ the distance between the vertex of the secondary reflector and the focal point behind it, d_{vv} is the distance between vertex of reflectors and θ_{min} is the resolution of the telescope at the specified frequency.

Main Reflector		Secondary Reflector	
Parameter	Value	Parameter	Value
D_m	1.2192 m	D_s	0.1778 m
a_m	0.1524 m	-	-
f_m	0.4572 m	f_s	0.3556 m
F_m	0.375	F_s	2
e_m	1	e_s	1.2184
α_m	0.131 rad	α_s	1.176 rad
Other Parameters			
f_{eq}	4.6468 m	F_{eq}	3.8114
M	10.16	Δ	0.0637 m
d_{vv}	0.3935 m	θ_{min}	0.15° (at 115 GHz)

Table 3.2: Main parameters of the corrugated horn antenna of the SMWT (Mini). See Figure 2.11 for definitions. r is the radius of aperture, α is the half angle of aperture, l is the length, R_H is the length of the cone, th is the thickness of the material, h is the depth of the corrugation, d is the internal radius of the corrugation, wm is the width of the corrugation, wh is the width of the no-corrugation. The corrugations are numbered from the waveguide to the aperture.

Horn		Waveguide	
Parameter	Value	Parameter	Value
r_h	14.770 mm	r_{wg}	1.486 mm
α_h	6.48°	α_{wg}	0°
l_h	130.078 mm	l_{wg}	2.540 mm
R_H	130.914 mm	-	-
th_h	6.439 mm	th_{wg}	6.439 mm
Parameters of the corrugations			
h_1	1.219 mm	d_1	5.766 mm
h_2	1.118 mm	d_2	5.842 mm
h_3	1.016 mm	d_3	5.918 mm
h_4	0.914 mm	d_4	6.020 mm
h_{5-92}	0.813 mm	d_5	6.096 mm
wm_{1-92}, wh_1	0.762 mm	wh_{2-93}	0.508 mm

3.3 Simulations with the current feed antenna

The following results were obtained using the simulation software *Zemax OpticStudio15* and the numerical computing *Matlab R2013b*. The known parameters presented in Table 3.1 were given to the model and other necessary parameters like the radius of curvature and the conic constant were calculated as explained in Appendix E. The aim is to represent the reflectors as realistic as possible and extract information about the system. Then, the feed was moved off-axis but keeping the illumination angle and the results are compared with the first configuration. Values used to evaluate the performance were the Strehl ratio and the illumination efficiency (2.19). A good definition of how the Strehl ratio is calculated in Zemax can be found in [54].

3.3.1 Central Feed

Using the original configuration, with the antenna in receiving mode (see Figure 3.2), the Huygens PSF for the central pixel is obtained (Figure 3.3). This result correspond to the efficiency of the actual system and will be used as a reference for subsequent scenarios. The obtained Strehl ratio is 1, which means that an image with no aberrations is obtained.

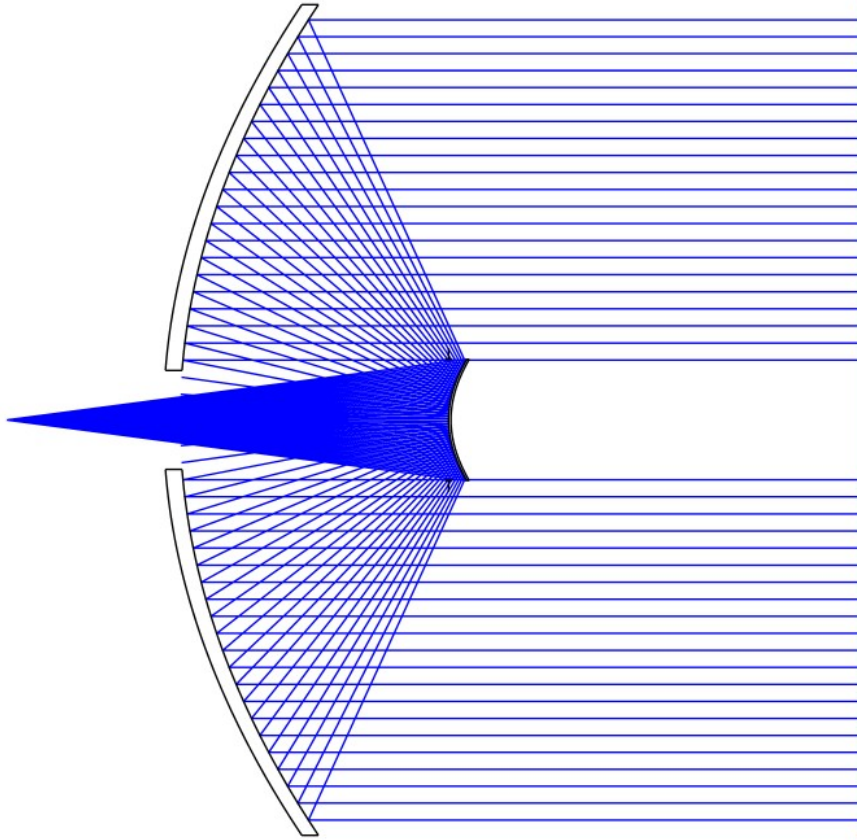


Figure 3.2: Scheme of the incoming rays to the reflectors of the SMWT (Zemax). The radiation arrives as a plane wave in parallel rays that are collected into the feed.

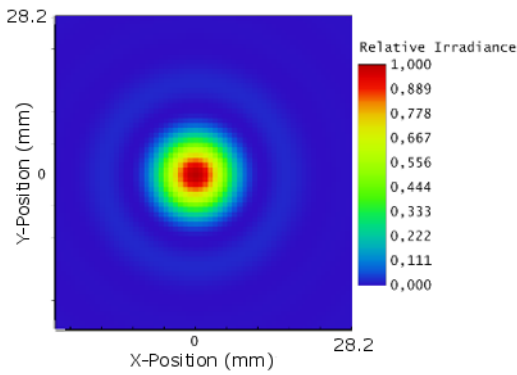


Figure 3.3: 2-D coloured linearly scaled Huygens PSF. Shows the peak of irradiance at the center. Zemax results for an on-axis feed in 115 GHz ($\lambda=2.6$ mm). Strehl Ratio = 1.

3.3.2 Off-axis Feed

The minimum object size that a telescope can distinguish is its resolution. At 115 GHz, the SMWT has $\theta_{min} = 2.61$ mrad, equals 0.15° (eq. (2.16)). From an antenna point of view it is equivalent to say that the main beam width is 0.15° .

The minimum spacing between pixels to avoid coupling between them is $d = 3w_0$ where $w_0 = 7.3$ mm is the beam waist at the focal plane. Then, the surrounding pixels should be located at least 21.93 mm off the center. When separated by this distance, the pixels, projected in the sky by eq. (2.29), are separated by $\sim 0.3^\circ$. This is equivalent to 2 times the antenna resolution, as expected.

The limit position to allocate the outer feed antenna is 45 mm off-axis because the aperture in the main reflector that has a radius of 76.2 mm and a beam displaced more than that will be considerably shadowed by the main reflector.

The feedhorn that is installed on the Mini is 42.42-mm wide in the outer part, and 29.54 mm corresponds to the aperture. This made impossible to allocate a second antenna of this kind closer than 42.42 mm. The main conclusion is that if we keep the actual horn design we need to use a pixel spacing of 42.42 mm. This is 3.5 times the spacing for one resolution element and the sky could not be fully covered in simultaneous mode scan.

Figure 3.4 shows the Huygens PSF obtained for a feed located out of the main axis by a distance of 42.42 mm. The Strehl ratio normalized over the central pixel is 0.833. We can see how the image is distorted due to the offset. It adopts a non-symmetric ellipsoidal shape, in the direction of displacement.

We calculate the illumination efficiency and the percentage of power that can overstep the main reflector hole (Figure 3.5a). The results are given in Table 3.3. At 115 GHz, the normalized efficiency is under the desired. The theoretical maximum is 0.8 as shown in Figure 3.5b. Also, 7.1% of the power of the six lateral beams cannot overstep the hole of the main reflector, as shown in Figure 3.6. In Appendix F a more detailed representation of this effect is presented. Figure 3.7 shows how the illumination efficiency changes when the outer pixel is moved off-axis. This shows that to obtain better results we need to decrease the distance between pixels.

Table 3.3: Illumination efficiency (effective e_{total} and normalized over the central pixel e_{norm}) and percentage of power that passes through the main hole. Parameters for the outer pixel using the actual characteristics of the feed horn of the SMWT. w_0 is the beam waist of the horn, w_{sec} is the beam radius at the secondary reflector, T_{e-sec} is the Edge Taper at the secondary, d the distance between pixels.

f [GHz]	w_0 [mm]	w_{sec} [mm]	T_{e-sec} [dB]	d [mm]	e_{total}	e_{norm}	Power %
115	7.31	73.96	12.55	42.42	0.598	0.740	92.90

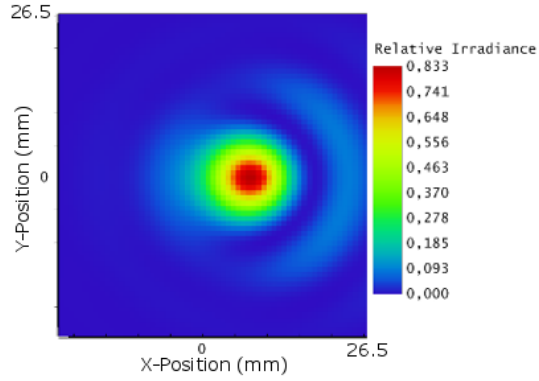
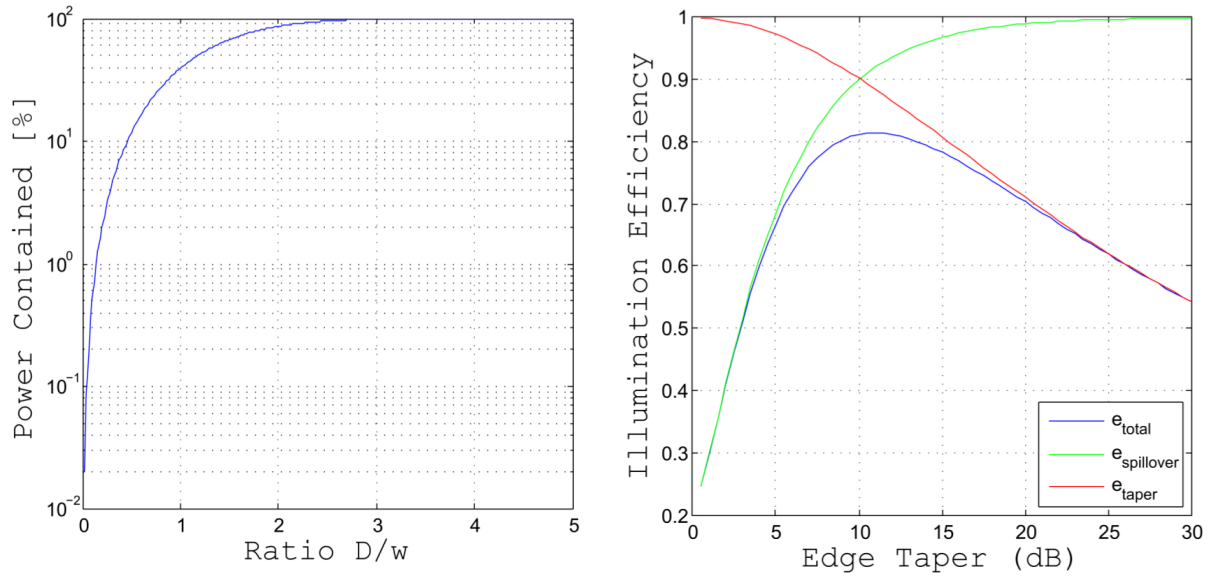


Figure 3.4: 2-D coloured linearly scaled Huygens PSF. Zemax results for a 42.42 mm off-axis feed in 115 GHz ($\lambda=2.6$ mm). Strehl Ratio = 0.833.



(a) Percentage of power contained on a circle of diameter D for a beam radius w .

(b) Illumination efficiency as a function of the edge taper for an on-axis system.

Figure 3.5: Percentage of power due to truncation and illumination efficiency (spillover and taper).

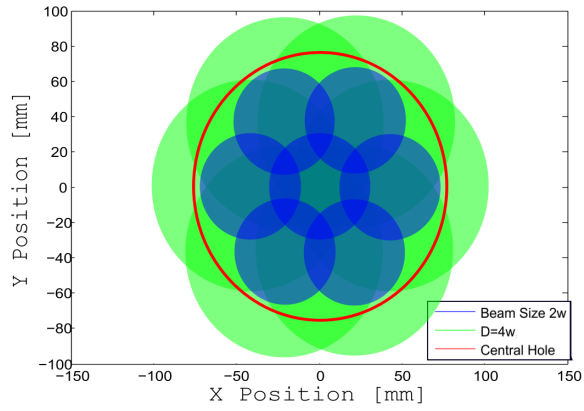


Figure 3.6: Seven beams at the hole of the main reflector. The beam size $2w$ contains 86.47% of the power. 99.97% of the power is contained in a diameter $D=4w$. It can be noticed that the hole produce sever truncation on the offset pixels.

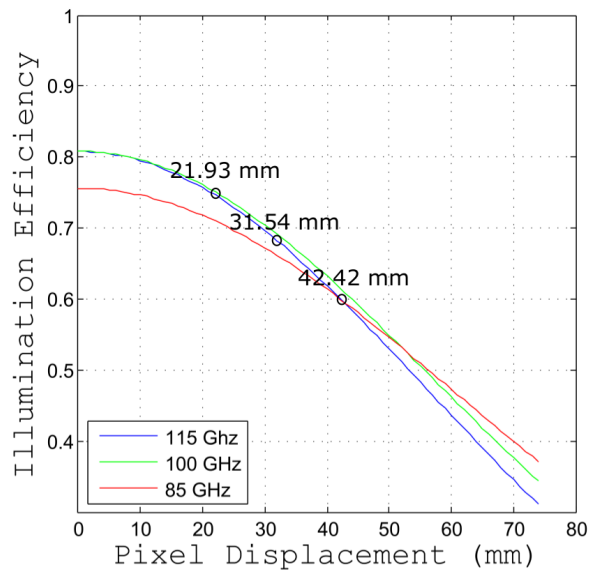


Figure 3.7: Illumination efficiency for the outer pixel as a function of displacement of the lateral pixels. Three scenarios are shown. With a distance of 21.93 mm, illumination efficiency of 0.75 is achieved.

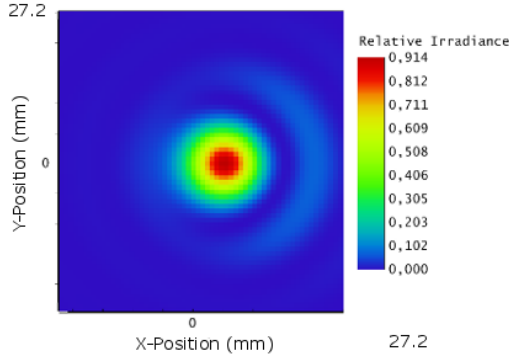


Figure 3.8: 2-D coloured linearly scaled Huygens PSF. Zemax results for a 31.54 mm off-axis feed in 115 GHz ($\lambda=2.6$ mm). Strehl Ratio = 0.914.

3.4 Simulations with a new feed antenna

3.4.1 Using the same aperture

Using the results of Figure 3.7, it is clear that to obtain a 7-pixel array with better performance is necessary to reduce the feedhorn separation. To achieve this goal a new feed has to be used. In a first stage we propose to keep the same aperture i.e. the same beam waist but avoiding the use of corrugations. Therefore a new smooth wall horn should be designed and fabricated.

We can reduce the size of the feed by redesigning the corrugated horn into a smooth-wall horn. If we use narrow walls down to 1 mm we obtain a distance of displacement between horns of 31.54 mm and a more compact configuration in the focal plane. Smooth-walled feedhorn designs have been achieved with good results in terms of crosspolar, side lobes and symmetry [55][56].

On this new design we obtain an illumination efficiency of 0.69 and 98.9% of power overstepping the main hole as shown in Table 3.4. The Huygens PSF is shown in Figure 3.8. The improvement compared to the previous configuration is almost 9% in efficiency and 6% of power. The normalized Strehl ratio over the central pixel is 0.91.

Table 3.4: Illumination efficiency and percentage of power that passes through the main hole. Parameters for the outer pixel using the actual electrical characteristics of the feed horn of the SMWT.

f [GHz]	w_0 [mm]	w_{sec} [mm]	T_{e-sec} [dB]	d [mm]	e_{total}	e_{norm}	Power %
115	7.31	73.96	12.55	31.54	0.686	0.849	98.89

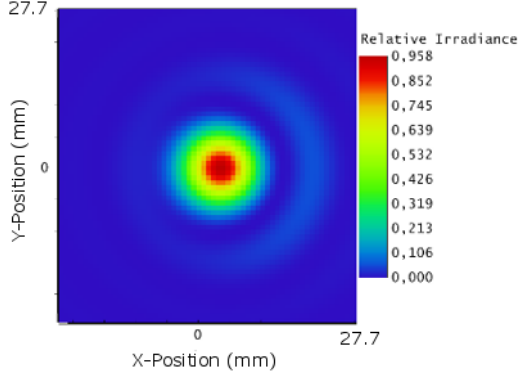


Figure 3.9: 2-D coloured linearly scaled Huygens PSF. Zemax results for a 21.63 mm off-axis feed in 115 GHz ($\lambda=2.6$ mm).Strehl Ratio = 0.958.

Corrugations permit having an axially-symmetric radiation pattern with better performance in terms of side lobe levels, cross-polarization and bandwidth at the expense of a thick wall.

In this work we decided not to do any changes to the antenna itself (primary and secondary reflectors), as this would imply a complete new telescope. But if a new telescope is built some design decision can be made to increase the field of view and therefore, allow an easier installation of multi-pixel systems.

3.4.2 Using an optimized aperture for a 7-pixel focal plane array

In a third scenario we decided to explore the feasibility of using other kind of feeds for the antenna. For this, we look for the best possible solution for a 7-pixel array. We obtain a pair of (w_0, d) that allows an efficiency to be over 70% (Appendix F.8). The frequency of interest is 115 GHz, so the system is optimized for that. The results are presented in Table 3.5 and Figure 3.9.

Table 3.5: Illumination efficiency and percentage of power that passes through the main hole. Parameters for the outer pixel using an hypothetical beam waist for the SMWT.

f [GHz]	w_0 [mm]	w_{sec} [mm]	T_{e-sec} [dB]	d [mm]	e_{total}	e_{norm}	Power %
115	6.7	80.56	10.58	28.0	0.725	0.891	98.89
115	6.7	80.56	10.58	32.0	0.699	0.859	97.39
115	6.8	79.40	10.89	18.0	0.778	0.956	99.89
115	6.8	79.40	10.89	21.63	0.756	0.929	99.69
115	6.8	79.40	10.89	27.0	0.731	0.898	99.18

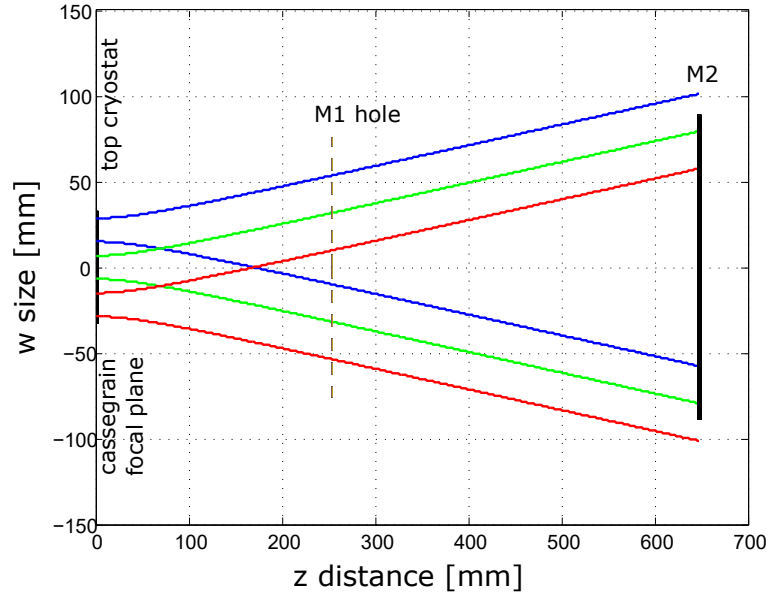


Figure 3.10: Beam propagation plot on axis for the SMWT at 115 GHz. Lateral view. The three colors represent 3 contiguous pixels.

The main restriction is again the size of the aperture. If it were possible to design a horn antenna that allows a beam waist $w_0 = 6.8$ mm, and a separation between them of 21.63 mm, a better performance is obtained, with an efficiency of 0.756 (94.5% of the theoretical maxima) and a normalized Strehl ratio over the central pixel of 0.958. We can see how distortion is reduced in comparison to the PSF of Figure 3.4.

The beam propagation plot for that case is shown in Figure 3.10. The option with a displacement of 18 mm is rejected as it doesn't satisfy the minimum distance of 21.63 mm that allows low levels of diffraction losses (eq. (2.29)).

3.5 Analysis of the Results

Considering the restriction of the hole of the main reflector, the most efficient configuration for an array receiver is a circular array of 7 pixels. A squared array of 3x3 wasn't studied in detail as it loses too much efficiency in the corner pixels, making this approach not efficient.

In a first scenario we decided to keep the current feed horn design. The pixel spacing is 42.42 mm, which translate as $\theta = 0.52^\circ$ on the sky. It would be necessary to make several scans in order to cover the full area of the sky. Moreover, the outer pixels will have an efficiency of 0.60 and just the 92.9% of power will overstep the central hole.

In a second scenario we propose to use a smooth wall horn antenna. The volume occupied in the focal plane is smaller, but keeping the aperture of 29.54 mm the maximum efficiency possible is of 0.69 and 98.9% of the power transmitted. A possible solution to achieve this illumination parameters are Vivaldi antennas [57].

The final proposal is to change the aperture size. We also change the beam waist, optimizing the illumination efficiency. We consider the restriction for the diffraction losses and obtain an efficiency of 0.76 with 99.7% of power overstepping.

The use of mirrors in the design was not considered due to the small space available between the focal plane and the primary mirror. Furthermore, the addition of weight is an obstacle for this small telescope.

The best of the three options in terms of performance is the one with a new antenna with a beam waist of 6.8 mm and at a distance between horns of 21.63 mm. To achieve this the beam waist should be located as close as possible to the aperture of the antenna.

Before designing this feed antenna is necessary to have a more detailed study, simulating the whole system with the 7 beams interacting. A simulation in the software HFSS using the real pattern of the feed horn antenna was attempted to be performed, but due to the dimensions of λ compared to the main reflector, the computing time to resolve the system was too high. Another approach that could be done is using the software GRASP, specifically designed for physical optics and to where the pattern of a feed antenna could be imported.

3.6 Summary

We have studied the feasibility of replacing the single-pixel receiver of the SMWT by a 7-pixel camera. Due to the reduced space between the receiver and the main reflector, the use of optical devices was avoided. The main restriction was the hole of the main reflector, which is 152-mm wide, truncating the outer beams of the array.

In order to obtain a reasonable illumination efficiency, a separation of pixels of 22 mm and a beam waist of 6.8 mm were used. 99.7% of the power was transmitted to the secondary reflector and the outer pixel had a normalized efficiency of 0.93. To achieve this results, a smaller feedhorn must be designed with thin walls without corrugations.

Chapter 4

Design of an Optical System for a W-Band Camera of a 12-m Antenna

One of the main improvement that has been proposed for the next generation of ALMA receivers is the use of a multi-pixel system. As a pathfinder for this technology we look to install such a system in an existing radiotelescope as LLAMA. LLAMA is a 12-m ALMA type antenna to be developed in the next years. The existence of a camera in one of its three cabins is considered. It would be a technological demonstrator for ALMA 2030. With these idea we explore the feasibility of such a system at W band in both scenarios.

For the design we use the known parameters of a 12-m ALMA antenna to design an intermediate optical system in the range of 85-115 GHz. The goal is to efficiently couple the beam of a 7-pixel array of horn antennas to the Cassegrain antenna. The work is performed with the consideration of minimizing beam truncation, adding the less amount of noise to the system and low levels of cross-polarization. A mixing of optics and quasi-optics theory is used to design and refine the model.

4.1 ALMA project

ALMA is a radio-astronomical project composed of 66 antennas with state of the art technologies. It was developed by an international consortium formed by the *European Southern Observatory* (ESO), the *U.S. National Science Foundation* (NSF) and the *National Institutes of Natural Sciences* (NINS) of Japan, together with NRC (Canada), NSC and ASIAA (Taiwan), and KASI (Republic of Korea), in cooperation with the Republic of Chile. The project is located at the Chajnantor plateau, at 5000 m above sea level. There is no radio pollution and the sky is dry so it allows observation almost all year, during day and night [5].

It has high resolution and sensitivity and is made to study faint sources of the beginning of the universe. This type of sources are invisible in the optical range and ALMA will allow new scientific targets. Nevertheless, there are some other scientific specialities that are also covered by ALMA. For example, star formation, chemistry of giant clouds of gas and dust, and the ability of mapping them in our and other galaxies.

The 66 antennas operate in interferometric mode, with baselines up to fifteen kilometers. Antennas can be relocated from compact to extended configuration according to the scientific objective of study. The range of operation is from 35 GHz (Band 1) to 950 GHz (Band 10). The division of ten bands is to match with the atmospheric transmission windows. Each of the bands is contained in a cartridge, inside the cryostat, under the focal plane of the antenna.

From the 66 antennas, twelve of them are of 7-m diameter and the other 54 are of 12-m. The bigger were made by three different distributors: AEM consortium (Alcatel Alenia Space Francia, Alcatel Alenia Space Italia, European Industrial Engineering S.r.L.y MT Aerospace), Vertex AntennenTechnik GmbH and Mitsubishi Electric Corporation (MELCO) which also provides the small antennas. All the 12-m antennas have the same geometrical properties and performance spite of the differences in design.

ALMA started with fully operations in year 2012. A new upgrade of ALMA is planned for the future, including the possibility of cameras and other improvements. For survey scientific targets the use of cameras is a major step. The time of scanning is valuable and the increase of mapping efficiency can make better use of it. We study the feasibility of a camera for ALMA and we design an optical system to achieve that. We decided to work with ALMA Band 3 as it is the low frequency limit for camera systems. At lower frequencies the large beam size makes more difficult the use of such technologies. If we can design an optical system for such band, for the others, with higher frequencies, the size of the devices will be smaller and then, the system will fit in the available space with no problems.

4.2 Description of the ALMA 12-m antenna

We used the parameters of the Cassegrain 12-m ALMA antenna. It has a target surface RMS accuracy of $15 \mu\text{m}$, and a target antenna pointing accuracy of 2 arcsecs. The angular resolution will be between 8 arcsecs (higher frequency) to 3 arcmin (lower frequency). For ALMA band 3 the angular resolution is 8 arcmin.

Table 4.1 shows the values of the optical parameters of the ALMA 12-m antenna, calculated using equations (2.9) to (2.15) and [58]. To simulate the feed pattern we used the data of the feed horns of ALMA Band 3 of [59].

Table 4.1: Main parameters of the 12-m Cassegrain antenna of ALMA. See Figure 2.9 for definitions. D is the diameter of the reflector, a is the diameter of the hole in the main reflector, f is the focal length, F is the ratio f/D , e is the eccentricity of the reflector, α is the half angle of aperture, M the total magnification of the reflectors, Δ the distance between the vertex of the secondary reflector and the focal point behind it, d_{vv} is the distance between vertex of reflectors and θ_{min} is the resolution of the telescope at the specified frequency.

Main Reflector		Secondary Reflector	
Parameter	Value	Parameter	Value
D_m	12 m	D_s	0.75 m
a_m	0.75 m	-	-
f_m	4.8 m	f_s	3.0885 m
F_m	0.4	F_s	4.1180
e_m	1	e_s	1.1053
α_m	1.1172 rad	α_s	0.0625 rad
Other Parameters			
f_{eq}	96 m	F_{eq}	8
M	20	Δ	0.2941 m
d_{vv}	4.5059 m	θ_{min}	0.0175° (at 100 GHz)

4.3 Design considerations

The design of the intermediate optics is based on the model of a Gaussian Telescope, explained in 2.4.1. A Zemax model of the system was built using the antenna parameters presented in Table 4.1. Some additional parameters were derived (details on Appendix G). The effect on efficiency caused by using an off-axis feed is studied. Values used to evaluate the performance are the Strehl ratio and the illumination efficiency (2.19). A set of considerations and assumptions that we take are:

- We design for a heterodyne camera of 7 pixels, limited to the available space (widget space).
- We design for the central pixel in the central frequency and then we evaluate the performance for the other frequencies and for the outer pixels.
- We give ourselves some freedom in changes. We assume that the robotic arm and the Water Vapor Radiometer will have to be redesigned and also the position of the cartridge for each band will change.
- We choose an edge taper of 10.9 dB.
- We choose a Gaussian Beam Telescope magnification M_{gbt} that allows a small aperture window at the cryostat.
- We choose the smallest incidence angle to the mirrors and the biggest focal length, to maximize efficiency.
- The size of lenses and mirrors should be small but for the outer pixel, it should fit $4w$ to guarantee that the power of the beam is minimally truncated.
- The use of a bi-hyperbolic HDPE fly-eye lens is considered at the vacuum window.
- We use the software *Matlab R2013b* and *Zemax OpticStudio15*.

4.4 Design of intermediate optics for ALMA Band-3

We present the main restrictions and parameters to design an intermediate optic system to couple a 7-beam array to the secondary reflector of ALMA. A design that fulfill those conditions and the mechanical consideration of the design are presented.

4.4.1 Restrictions for ALMA

For the second generation of ALMA, multi-pixel receivers will be considered. This kind of system will use the same antenna, but the complete cryostat, optics and calibration scheme can be redesigned.

The cryostat is placed just under the Cassegrain focal plane as is shown in Figure 4.1. The space available to place warm optics is a cylinder of 0.6 m high with a radius of 510 mm. It is also necessary to consider that other bands will be allocated around Band-3. Figure 4.2 shows the actual configuration of ALMA bands in the cryostat.

The receiver, including the feed horn antenna, will be placed inside the cryostat. The communication between the outside and the inside will be through a window. It must be small and strong to keep the temperature inside and to resist differences of pressure. At the same time, it should be transparent for the operating frequency.

Having an edge taper of 10.9 dB, the beam radius at the top of the cryostat is the beam waist. For 100 GHz, this corresponds to $w_0 = 16.8$ mm (eq. (2.5) and (2.7)). The spacing between pixels at the focal plane should be $s_{fp} = 58.6$ mm (eq. (2.29)).

As we cannot place every band on the Azimuth axis, we can use a switchable mirror to choose between the 10 bands. Another option is to illuminate the secondary reflector with a small angle, which is the way that ALMA does currently. In any case the use of an intermediate optical system to reduce the beam size is required and then, to reduce the vacuum window. On the contrary, for a 7-pixel camera we will have a window seven times larger than the current window, which is of 70 mm of diameter [58]. We choose the first option to our design.

To have a reference of performance we calculate the efficiency of a system with 7-pixels using the focal plane beam waist of ALMA Band-3. The system using the actual ALMA Band-3 optics: horn, lens and ellipsoidal mirror gives the results shown in Table 4.2. This system is not feasible as the space used into the cryostat for the 7 pixels does not fit into the cartridge.

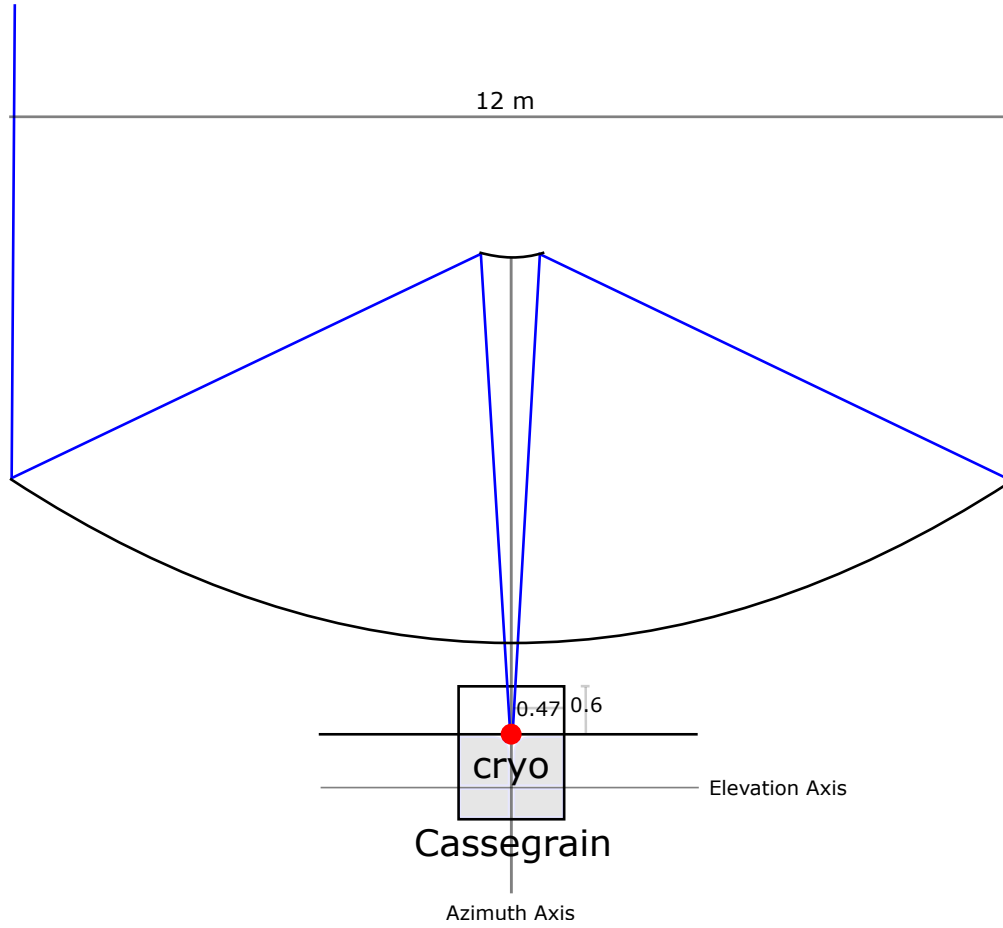


Figure 4.1: Scheme of ALMA 12-m antenna and its cryostat. Ten ALMA bands are placed into the cryostat and over it a widget space of 0.6 m is available to place intermediate optical systems. Adapted from 3.1 [58]

Table 4.2: Illumination efficiency (effective and normalized over the central pixel) and percentage of power that passes through the hole of the primary reflector for a 12-m ALMA antenna. Parameters for the outer pixel using the actual characteristics of the feed horn+lens+ellipsoidal mirror of Band-3 [59]. w_0 is the beam waist at the Cassegrain focal plane, w_{sec} is the beam radius at the secondary reflector and d is the spacing between pixels at the Cassegrain focal plane.

f [GHz]	w_0 [mm]	w_{sec} [mm]	T_{e-sec} [dB]	d [mm]	e_{total}	e_{norm}	Power %
115	16.8	334.8	10.9	58.6	0.790	0.970	100
100	19	296.3	13.9	58.6	0.771	0.969	100
85	22.6	249.6	19.6	58.6	0.670	0.944	100

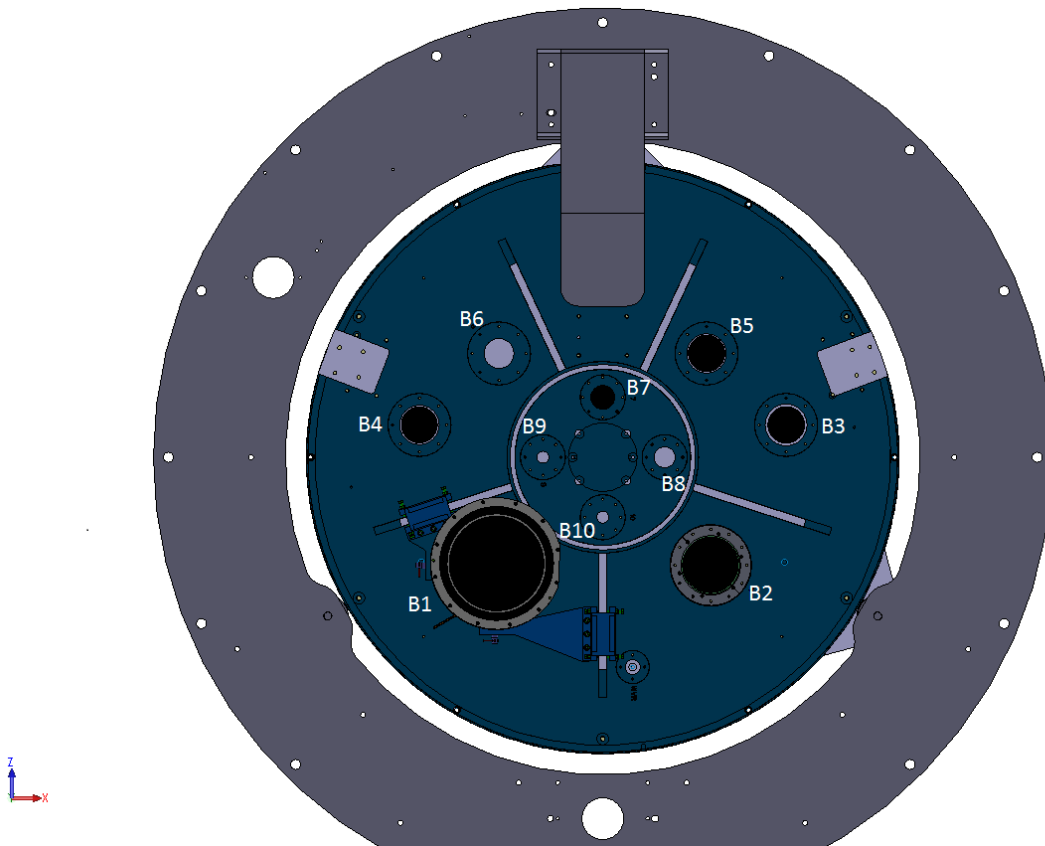


Figure 4.2: Upper view of the actual cryostat of ALMA. 10 bands are placed in the available space.

We have the conditions of having an optimized beam waist at the focal plane of the telescope and image formation. At the same time we have restricted space into the cartridge. Then, we choose to use a compacted Gaussian Beam Telescope made by 2 mirrors in order to minimize noise temperature and cross polarization and to achieve the conditions previously specified in Section 4.3

4.4.2 Design of a Gaussian-Beam Telescope for ALMA Band-3 camera

The specific parameters of design of the Gaussian Beam Telescope (GBT) are related to the optimization of efficiency. In this case, we know the edge taper at the secondary reflector. Then, we know the size of the beam waist at the Cassegrain focal plane. Choosing a magnification (M_{gbt}) we have the input beam waist of the system. To minimize the vacuum window we placed w_{0in} at the top of the cryostat.

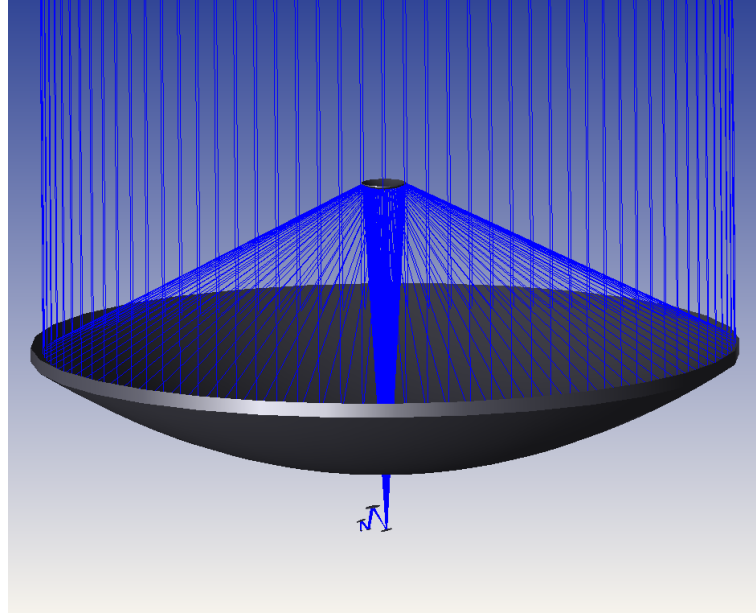
Finally we have three free parameters: the incidence angle to the mirrors (θ_i) and two of the following: d_{in} , f_1 , f_2 , d_{out} . For convenience, we choose a pair (d_{out}, f_2) as inputs and (d_{in}, f_1) as outcome. This because d_{out} and f_2 are bigger so the restrictions of space can be applied in better way. After testing several combinations, the parameters that deliver better performance were chosen.

Flat mirrors are used to compact the system but they do not change the properties of the beam. They add distortion as the surface is not perfectly flat, so the number of them must not be excessive. The size of the mirrors is a function of the waist at that distance. We use the criteria of having $4w$ of the outer pixel, this is a size of $2s + 4w$ where s is the spacing between pixels.

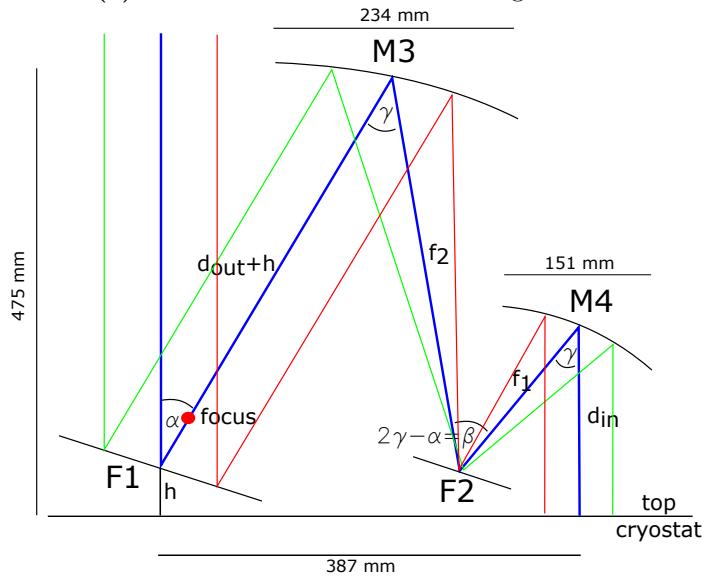
We choose ellipsoidal mirrors as they have been used with more success than other conics. To calculate the shape of the mirrors, we use the procedure described in [25] and summarized in Appendix B. Finally, the distortion due to reflection and cross polarization is calculated using eq. (2.23) and (2.24).

Model

The proposed model is presented in Figure 4.3. The values of the parameters are in Table 4.3. We choose a magnification $M_{gbt} = 2$, thus, the spacing between pixels at the top of the cryostat is 29.28 mm. The beam waist at the same place is 8.4 mm. The size of M3 is 253.94 mm (238.63 perpendicular to the direction of propagation) and the size of M4 is 160.94 mm (151.24 perpendicular to the direction of propagation). The central pixel is placed at 387 mm off the center of the cryostat. The total vertical space used is 475.15 mm, considering the size of M3. The vacuum window is of radius 43.92 mm, which is an area of 60.60 cm². Fly-eye lenses can be used as a vacuum window if necessary, depending on the design of the feed antenna. In Appendix G are shown the parameters to simulate this model in Zemax.



(a) ALMA 3D model obtained using Zemax.

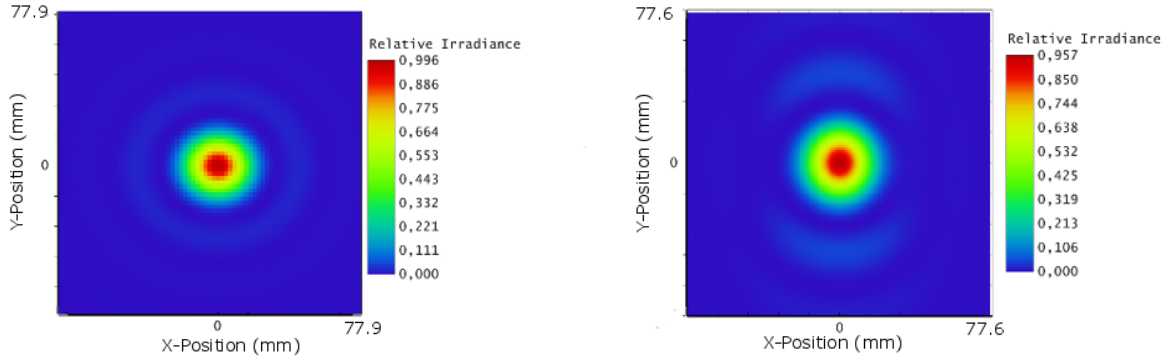


(b) Scheme of GBT designed for ALMA 12-m antenna. The beam hits a flat mirror placed above the top of the cryostat. Then it is directed to the GBT formed by M3 and M4. Another flat mirror is placed between the curved mirrors to compact the system. Finally, the 7 beams arrive into the vacuum window.

Figure 4.3: Model of the optical system proposed for ALMA heterodyne receiver.

Table 4.3: Parameters for the GBT of ALMA.

d_{in} [mm]	f_1 [mm]	f_2 [mm]	d_{out} [mm]	h [mm]	γ [°]	α [°]
189.97	200.86	401.73	445.30	24.70	40	30



(a) Huygens PSF for the central pixel. Strehl Ratio=0.996. (b) Huygens PSF for the offset pixel. Strehl Ratio=0.957.

Figure 4.4: Huygens PSF obtained in Zemax for the central and 29.28-mm offset pixel of ALMA model.

Table 4.4: Illumination efficiency (effective and normalized over the central pixel) and percentage of power that passes through the main hole of a 12-m ALMA antenna. Parameters for the outer pixel using the GBT designed for Band-3. The three frequencies has the same efficiencies as the edge taper is similar and the effects of a non ideal feed are not considered. w_0 is the beam waist at the Cassegrain focal plane, w_{sec} is the beam radius at the secondary reflector and d is the spacing between pixels at the Cassegrain focal plane. $M_{gbt} = 2$.

f [GHz]	w_0 [mm]	w_{sec} [mm]	T_{e-sec} [dB]	d [mm]	e_{total}	e_{norm}	Power %
115	14.6	335.07	10.88	58.6	0.790	0.969	100
100	16.8	334.75	10.90	58.6	0.790	0.969	100
85	19.8	334.44	10.92	58.6	0.790	0.969	100

Performance

The Huygens PSF for the central and 29.28-mm offset pixel are shown in Figure 4.4. The Strehl ratio normalized over the central pixel is 0.961. There is not a considerable distortion when we displaced the feed. An ellipsoidal shape is formed in the PSF when the outer pixel is analysed. The enlargement happens in the same direction of displacement of the pixel.

The illumination efficiencies calculated for this model are in Table 4.4. Comparing to the reference of Table 4.2, we obtain the same normalized efficiency but a higher effective efficiency. There are no problems with beam truncation at the main dish hole.

The beam distortion due to reflections and cross polarization are shown in Table 4.5. The condition that $k \geq 0.99$ is accomplished as we have used long focal length and a relatively small incidence angle ([16], chapter 5.8.2 and 5.8.3).

The beam propagation plot is presented in Figure 4.5. At distance f_1 from M4 the flat mirror F2 is placed, where the beams intersect each other, so the size of the mirror is minimized. F1 is placed near the Cassegrain focal plane, minimizing the mirror size.

Table 4.5: Beam distortion in curved mirrors due to reflections and cross polarization in ALMA’s GBT

mirror	k_f	k_{co}	$k = k_f k_{co}$
M3	0.9997	0.9998	0.9995
M4	0.9994	0.9996	0.9990
GBT	0.9991	0.9994	0.9985

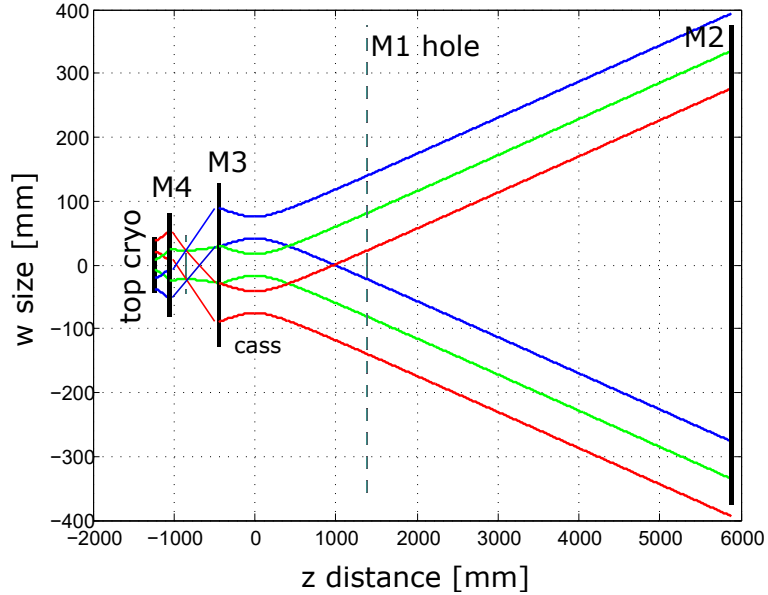
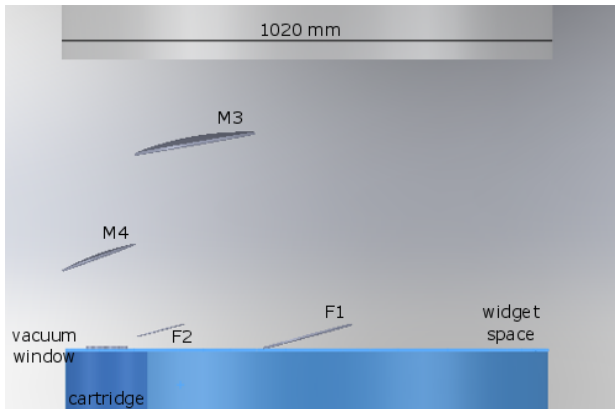


Figure 4.5: Beam propagation plot on axis for ALMA’s GBT at 100 GHz. Lateral view. The three colors represent 3 contiguous pixels.

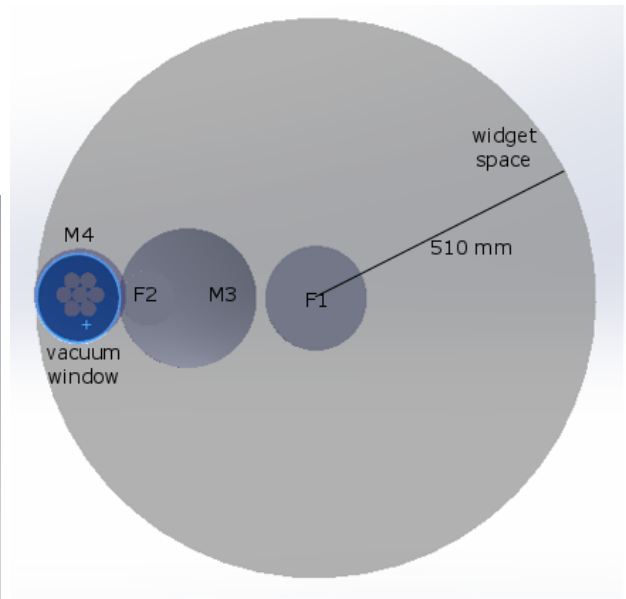
As the system is optimized for the central beam, the lateral beams suffers from spillover in the secondary reflector (M2). This effect is considered when calculating illumination efficiency and the consequences are not restrictive.

4.4.3 Mechanical considerations for ALMA

An image of the 3-D model is presented in Figure 4.6. This model was exported from *Zemax’s* optical model and then completed with the widget space and cryostat space. The system fits in the available space, leaving space for other ALMA bands. Figure 4.7 shows the mechanical model of the ALMA cartridge with 7 hypothetical feedhorns inside it.

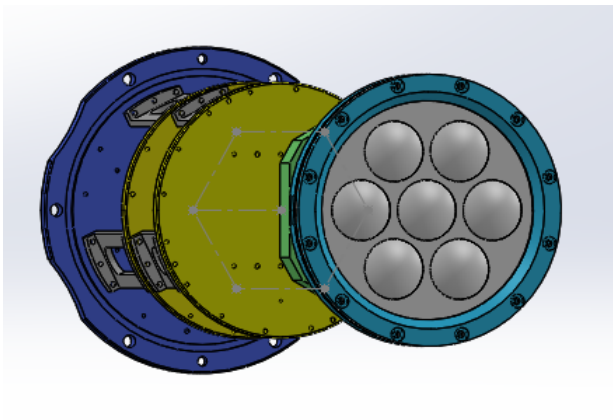


(a) Frontal view of the model.

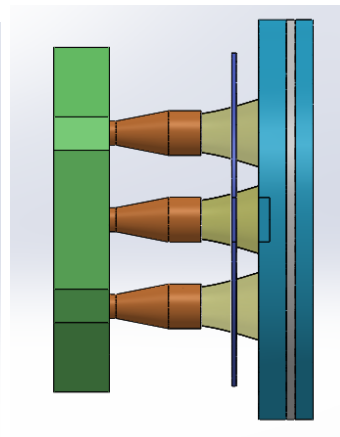


(b) Upper view of the model.

Figure 4.6: 3-D model of the intermediate optical system designed for ALMA Band-3.



(a) The cartridge where the 7 horn antennas will be placed.



(b) Lateral view of the 7 horn antennas inside the cryostat.

Figure 4.7: Mechanical model of the cartridge inside the cryostat.[60]

4.5 Tolerances in construction and assembly

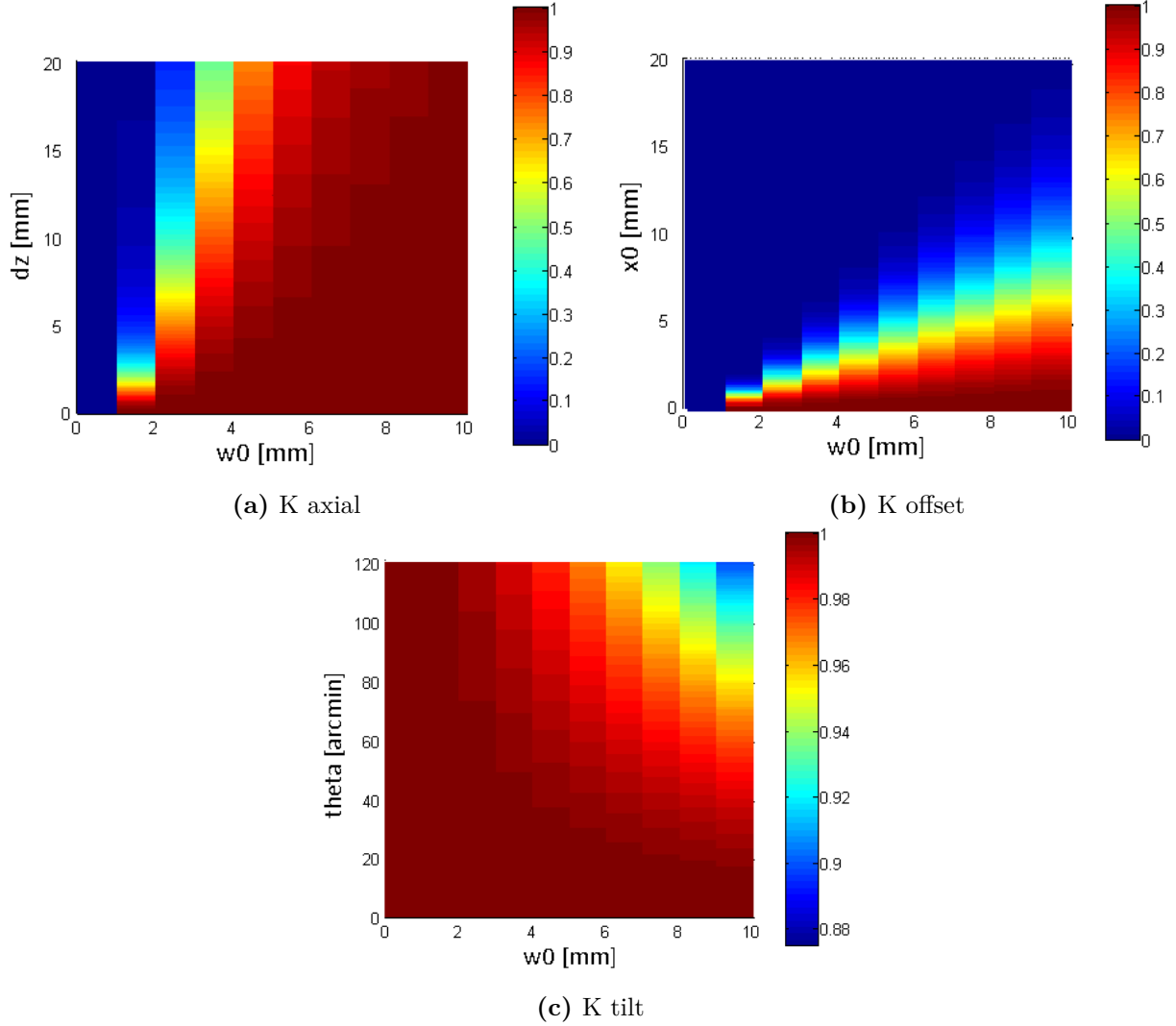


Figure 4.8: Coupling Efficiency as a function of the displacement, offset and tilt. w_0 is the beam waist of the horn, dz is the difference in position between the beam waist produced in the horn and the designed position, x_0 is the offset between propagation axes and θ is the tilt between propagation axes.

If the peak surface deviations are kept lower than 0.01λ , losses are 0.8%. For the four mirrors this translates in a total lost of 3.2% (transmission $K \geq 0.968$). This implies to have a surface accuracy better than $26.1 \mu\text{m}$, considering the higher frequency of the band ([16], chapter 5.8.4).

Since we have a warm optics stage and then a cold one, misalignment effects are likely to happen. Once the horns are inside the cryostat we do not have access to them and we will only have the chance to calibrate the warm optics. This effect must be taken into account. Using the formulas in chapter 4 of [16], the coupling efficiencies due to axially alignment, tilt and offset beams is calculated and presented in Figure 4.8. Keeping an axial displacement less than 10 mm, an offset of 0.8 mm and a tilt of 48 arcmin, a coupling factor of 99% is obtained for a beam with beam waist of 8.4 mm.

4.6 Analysis of results obtained for ALMA

Ten bands are placed in the same cabin. Despite the fact that the widget space is 0.6 m high, only 0.24 m are actually used because of a moving mechanical arm. In the design presented we assumed that the mechanical arm should be redesigned, and the full widget space was considered available. Otherwise, the restrictions of space will be that strong that a decay in efficiency will result for the addition of extra mirrors or the short focal lengths and truncation of the beams due to the need of having smaller devices.

A design for ALMA Band-3 camera was developed. We considered the use of four mirrors, two of them used to have a Gaussian Beam Telescope with magnification $M_{gbt} = 2$ and two to compact the system. The optical axis of the system is contained in a single plane.

A flat mirror F_1 was placed at the Azimuth axis. This acts as a switchable mirror that select the observing band. As it was designed for Band-3, it is large enough to be used to select higher bands of the system. It has to be noticed that we are proposing to change the actual band selection scheme. The current strategy consist on having all the receivers in the antenna focal plane, pointing to the subreflector with small different angles.

The proposed system achieves an illumination efficiency of 79% for the outer pixel, meanwhile the central pixel has an efficiency of 81%. Strehl ratio obtained is 0.996 and 0.995 for ALMA central and offset pixel.

Beam truncation in the hole of the main reflector is not an issue as it is big enough to allow the pass the seven beams. For all the mirrors we use the criteria of having $4w$ of the outer pixel contained in the surface to minimize beam truncation.

Although cross polarization of the pattern was not calculated, this should be low because we use mirrors instead of lenses. We also considered the use of small incidence angles and long focal length for the same reason. The addition of noise temperature should also be minimal as we restrict the use of lenses in the design.

The surface accuracy of the mirrors must be better than $26.1 \mu\text{m}$ to have total losses under 3.2%. A good alignment of optics is also relevant to guarantee the performance as it is expected.

The vacuum window is planned to be as a fly eye lens made of HDPE. Using this configuration each part of the lens acts as a pixel and keeps the image, which will not happen with a single lens. The size of each one is equal to $s_{fp}/M_{gbt} = 57 \text{ mm}$ and contains approximately $3.5w_{0in}$. By-hyperbolic lenses haven been used with good results but the final shape and focal length depend highly on the feed horn antenna used and the position relative to the top of the cryostat.

Considering that the resolution is the same for a single or multi-pixel receiver, while a single pixel scans a zone of 1 arcmin, the 7-pixel arranged as proposed here can scan 7 arcmin, and the mapping is about 5 times faster (see Chapter 2.4.3).

4.7 LLAMA project

LLAMA, the *Large Latin American Millimeter Array*, is a project of Argentina and Brazil whose objective is to install and operate a radio-telescope. It will be located at the north-west of Argentina in Alto Chorrillos (Puna of Atacama) at 4820 m above sea level. This is 180 km far from ALMA, with similar atmospheric conditions.

The telescope will be used in the *Very Large Baseline Interferometry* (VLBI) network and also as a single telescope. ALMA, APEX and ASTE together with LLAMA connected in a network will have an angular resolution 10 times greater than ALMA by itself.

As a single dish radiotelescope, the scientific goals are astronomical objects located in a broad distance range, from the Sun to red-shifted galaxies using spectroscopy. More details about the LLAMA project can be found in [11]. In the middle term, LLAMA is envisioned to participate of the Event Horizon Project. Telescopes located around the world will operate as a single interferometer achieving the highest angular resolution for ground-based telescopes. Using this will be possible to understand the physics of accretion in the area surrounding the black hole at the center of the galaxy and also to test some phenomena of General Relativity [61].

It will be an ALMA-type antenna with 12 m of diameter for its main reflector. They choose Vertex AntennenTechnik GmbH, one of the distributors of ALMA, to develop their antenna. LLAMA will cover the same frequency range that ALMA, with frequencies between 35 to 1000 GHz. One difference with the ALMA antenna is that LLAMA will have one Cassegrain focus and two Nasmyth cabins to place different types of receivers, as shown in Figure 4.9. An heterodyne array receiver is planned for the Cassegrain cabin.

For the purpose of this work, we will design the intermediate optics corresponding to W band or ALMA Band-3 (84 - 116 GHz). Cameras for bands in higher frequencies will need smaller optical devices. For lower frequencies, the size of the devices would be too much big to be developed, then Band-3 is the critical case.

4.8 Description of the LLAMA 12-m antenna

LLAMA will have the same Cassegrain 12-m antenna than ALMA, manufactured by Vertex AntennenTechnik GmbH. As it was mentioned, three cabins with multiple instruments are planned for LLAMA: single and multi-pixel receivers in bolometric or heterodyne technology. We design for the Cassegrain cabin a heterodyne camera of 7 pixels.

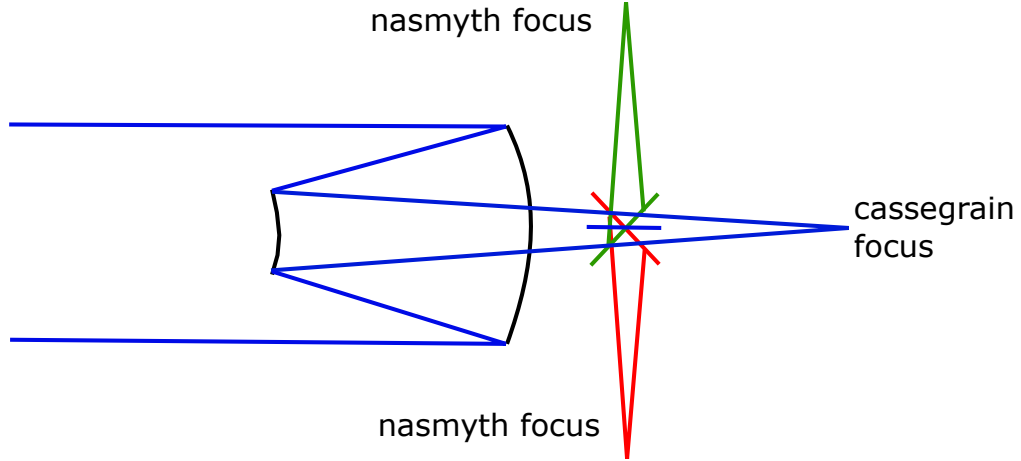


Figure 4.9: Scheme of a Cassegrain Telescope with three possibilities of focal planes. The traditional Cassegrain, behind the main reflector and two Nasmyth at the sides. A movable mirror is used to guide the radiation to one of the three cabins. This allows a fast swapping between different instruments.

4.9 Design of intermediate optics for LLAMA Band-3

We present the main restrictions and parameters to design an intermediate optic system to couple a 7-beam array to the secondary reflector of LLAMA. Finally a design that fulfil those conditions and the mechanical consideration of the design are presented. The design considerations are the same that we use for ALMA design in Chapter 4.3.

4.9.1 Restrictions for LLAMA

LLAMA is planned to contain cameras between its instruments. The heterodyne camera will be allocated in the Cassegrain cabin. A dichroic and some mirrors are used to guide the beam to the lateral Nasmyth cabins (see Figure 4.10). This optical system occupy some of the available space and is located at the elevation axis, 803 mm under the Cassegrain focus. This implies that the radius of the beam at that distance is bigger than the beam waist, so the optical devices to collect them will be proportionately bigger.

Finally, the available space is of 0.45 m high and with a radius of 0.53 m. The first optical device of our system will pick up the radiation from the azimuth axis, and will be located just under the mirror that provide cabin selection. The window of the cryostat should be minimized, for the same reasons as in ALMA cryostat. Moreover, the system should be compact to allow other bands at the same cabin.

Similarly, as we did for ALMA design, having an edge taper of 10.9 dB, the beam radius at the Cassegrain focal plane is the beam waist, which in this case does not match with the one at the top of the cryostat. For 100 GHz, this corresponds to $w_0 = 16.8$ mm (eq. (2.5) and (2.7)). The spacing between pixels at the focal plane should be $s_{fp} = 58.6$ mm (eq. (2.29)). Then, we design another Gaussian Beam Telescope with magnification 4.5, formed by two ellipsoidal mirrors and flat mirrors to compact the system.

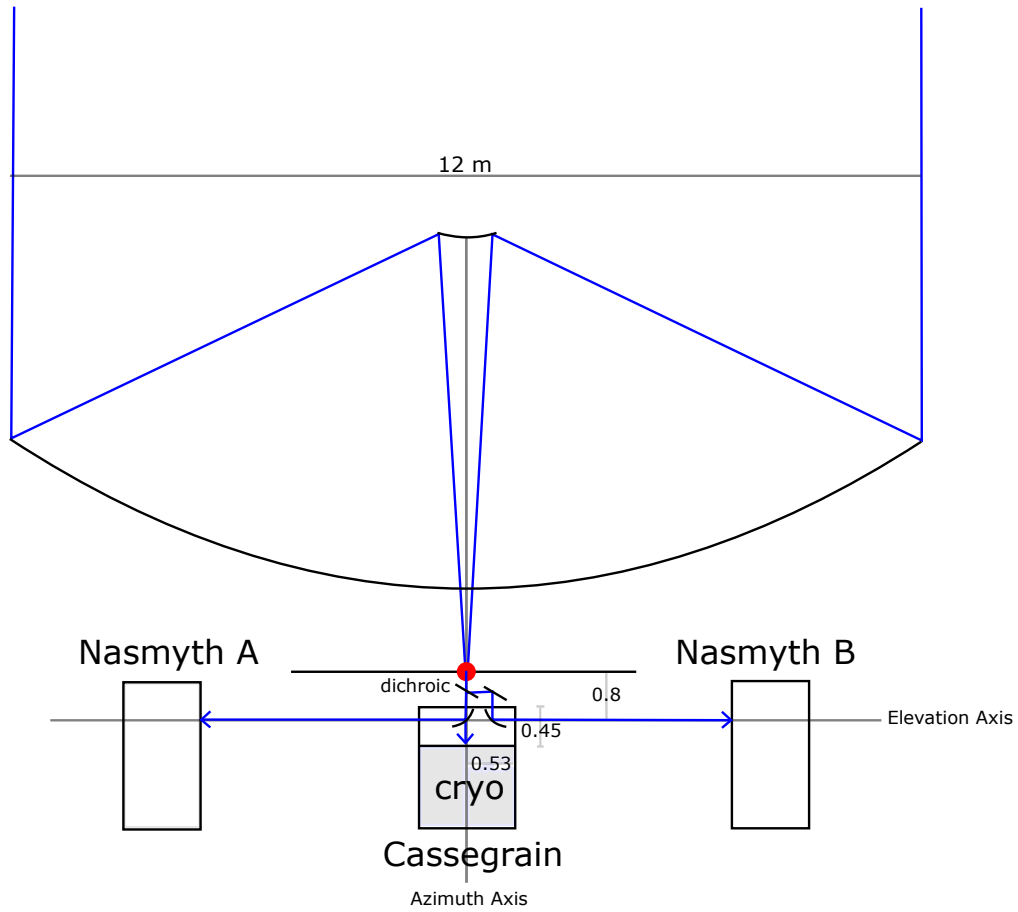


Figure 4.10: Scheme of LLAMA 12-m antenna and its cryostat. LLAMA bands are placed into the cryostat and over it an available space of 0.45 m high to place intermediate optical systems. Adapted from [62], image in page 4.

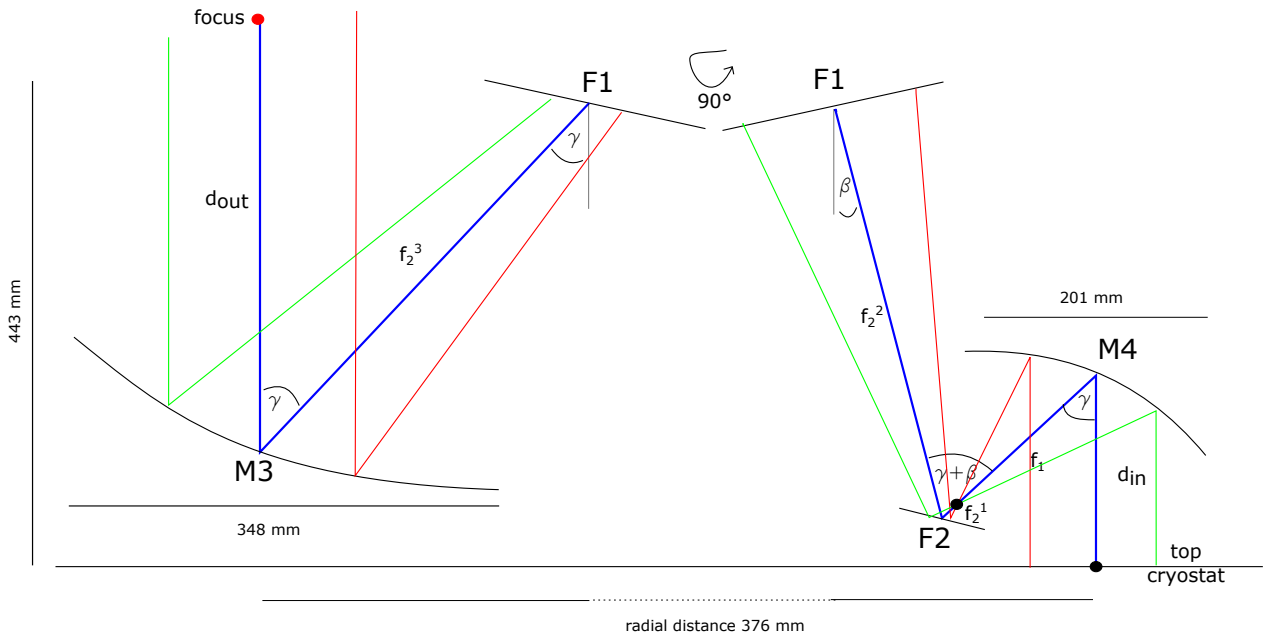


Figure 4.11: Scheme of GBT designed for LLAMA 12-m antenna. The beam hits M3 that is big due to the distance from the Cassegrain focal plane. Then it is directed to M4. Two flat mirrors are used in the middle to compact the system. Finally, the 7 beams arrive into the vacuum window.

Table 4.6: Parameters for the GBT of LLAMA.

d_{in} [mm]	f_1 [mm]	$f_2 = f_2^1 + f_2^2 + f_2^3$ [mm]	d_{out} [mm]	γ [°]	β [°]
170	178.40	802.82=12.52+370.42+419.88	973	45	15

4.9.2 Design of a Gaussian Beam Telescope for LLAMA Band-3 camera

We choose a magnification $M_{gbt} = 4.5$ to define the input beam waist w_{0in} of the system, which is placed at the top of the cryostat. We choose the smallest incidence angle to the mirrors (θ_i), then choose a pair (d_{out}, d_{in}) as inputs and (f_1, f_2) as outcome. In this case, the position of M3 and M4 are highly restricted and the focal distances have more flexibility. After testing several combinations, the parameters that deliver better performance were chosen.

Model

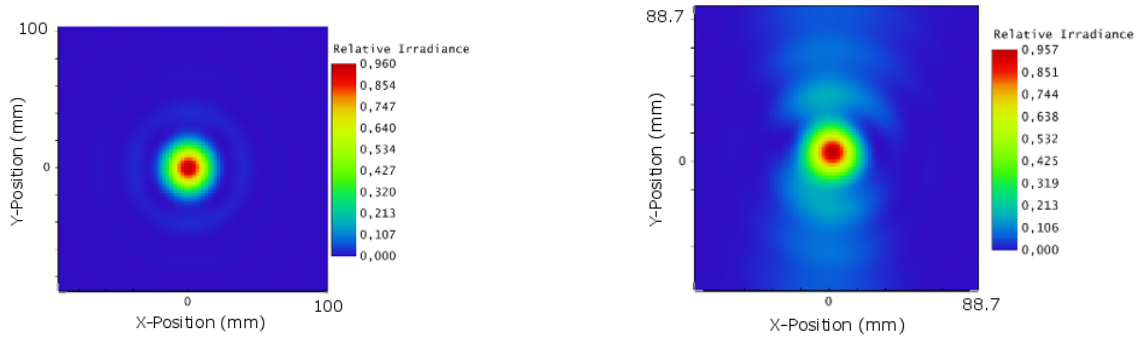
The proposed model is presented in Figure 4.11. The values of the parameters are in Table 4.6. We choose a magnification $M_{gbt} = 4.5$, thus, the spacing between pixels at the top of the cryostat is 13.01 mm. The beam waist at the same place is 3.73 mm. The size of M3 is 376.99 mm (348.29 perpendicular to the direction of propagation) and the size of M4 is 217.1 mm (200.57 perpendicular to the direction of propagation). The central pixel is placed at a radius 376.1 mm off the center. The total vertical space used is 442.80 mm, considering the size of mirror F1. The vacuum window is of radius 19.52 mm, which is an area of 11.96 cm², much smaller than the designed for ALMA. Fly-eye lenses can be used as a vacuum window if necessary, depending on the design of the feed antenna. In Appendix G are shown the parameters to simulate this model in Zemax.

Performance

The Huygens PSF for the central and the 13.01-mm off-center pixel is in Figure 4.12. The Strehl ratio normalized over the central pixel is 0.997. There is not a considerable distortion when we displaced the feed. An ellipsoidal shape is formed in the PSF when the outer pixel is analysed. The enlargement happens in the same direction of displacement of the pixel.

The illumination efficiencies calculated for the model previously presented are in Table 4.7. Those are the same as obtained for ALMA because both systems were designed using the same parameters from de Cassegrain focal plane to the secondary. The differences are in the Gaussian Beam Telescope and inside the cryostat.

The beam distortion due to reflections and cross polarization are shown in Table 4.8. The condition that $k \geq 0.99$ is accomplished ([16], chapter 5.8.2 and 5.8.3).



(a) Huygens PSF for the central pixel. Strehl Ratio=0.960. (b) Huygens PSF for the offset pixel. Strehl Ratio=0.957.

Figure 4.12: Huygens PSF and Wave-front function obtained in Zemax for the central and 13.01-mm offset pixel of LLAMA model.

Table 4.7: Illumination efficiency (effective and normalized over the central pixel) and percentage of power that passes through the main hole of a 12-m LLAMA antenna. Parameters for the outer pixel using the GBT designed for W band. The three frequencies has the same efficiencies as the edge taper is similar and the effects of a non ideal feed are not considered. w_0 is the beam waist at the Cassegrain focal plane, w_{sec} is the beam radius at the secondary reflector and d is the spacing between pixels at the Cassegrain focal plane. $M_{gbt} = 4.5$

f [GHz]	w_0 [mm]	w_{sec} [mm]	T_{e-sec} [dB]	d [mm]	e_{total}	e_{norm}	Power %
115	14.6	335.07	10.88	58.6	0.790	0.969	100
100	16.8	334.75	10.90	58.6	0.790	0.969	100
85	19.8	334.44	10.92	58.6	0.790	0.969	100

Table 4.8: Beam distortion in curved mirrors due to reflections and cross polarization in LLAMA's GBT

mirror	k_f	k_{co}	$k = k_f k_{co}$
M3	0.9997	0.9998	0.9995
M4	0.9969	0.9974	0.9943
GBT	0.9966	0.9972	0.9938

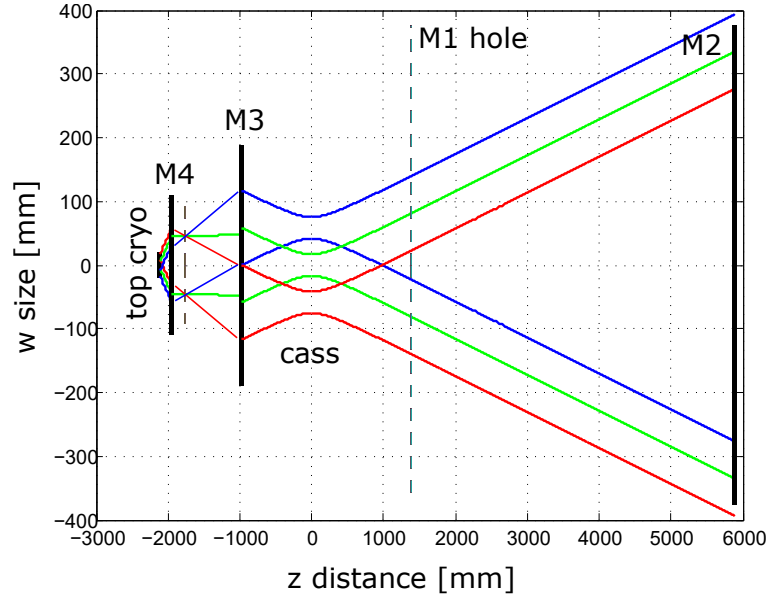


Figure 4.13: Beam propagation plot on axis for LLAMA’s GBT at 100 GHz. Lateral view. The three colors represent 3 contiguous pixels.

Table 4.9: Comparative analysis of hexagonal cameras with 7, 19, 37 and 61 pixels. The size of M3, the power lost for the outer pixel due to beam truncation at the primary reflector hole and the illumination efficiency for the outer pixel is considered.

Parameter	7 pix	19 pix	37 pix	61 pix
M3 size [mm]	348	465	582	700
Beam truncation [% of power lost]	0	0	0	0.15
Illumination efficiency	0.79	0.72	0.61	0.49

The beam propagation plot is presented in Figure 4.13. At distance slightly bigger than f_1 from M4 is placed the flat mirror F2 where the beams intersect each other so the size of the mirror is minimized. In the secondary reflector M2, the same effect than in ALMA happens. The lateral beams suffer from spillover with not restrictive consequences.

4.9.3 Expansion of LLAMA’s Band-3 Camera Using More Pixels

To analyse the expansion of the 7-pixel camera of the LLAMA 12-m antenna we choose three parameters: size of the mirror M3, beam truncation at the hole of the primary reflector and illumination efficiency at the secondary reflector. A comparison between four scenarios is shown in Table 4.9. We use the same hexagonal configuration.

We can conclude that the size of M3 and the illumination efficiency are the critical parameters when we add more pixels to the original configuration. Even when we use the 61-pixel configuration, practically all of the power of the beams can overstep without truncation. For the scenario with 19 pixels we obtain a bigger M3 mirror and less illumination efficiency but increasing mapping efficiency and achieving the state-of-the-art number of pixels for W-band heterodyne cameras in circular configuration (see Table 2.2).

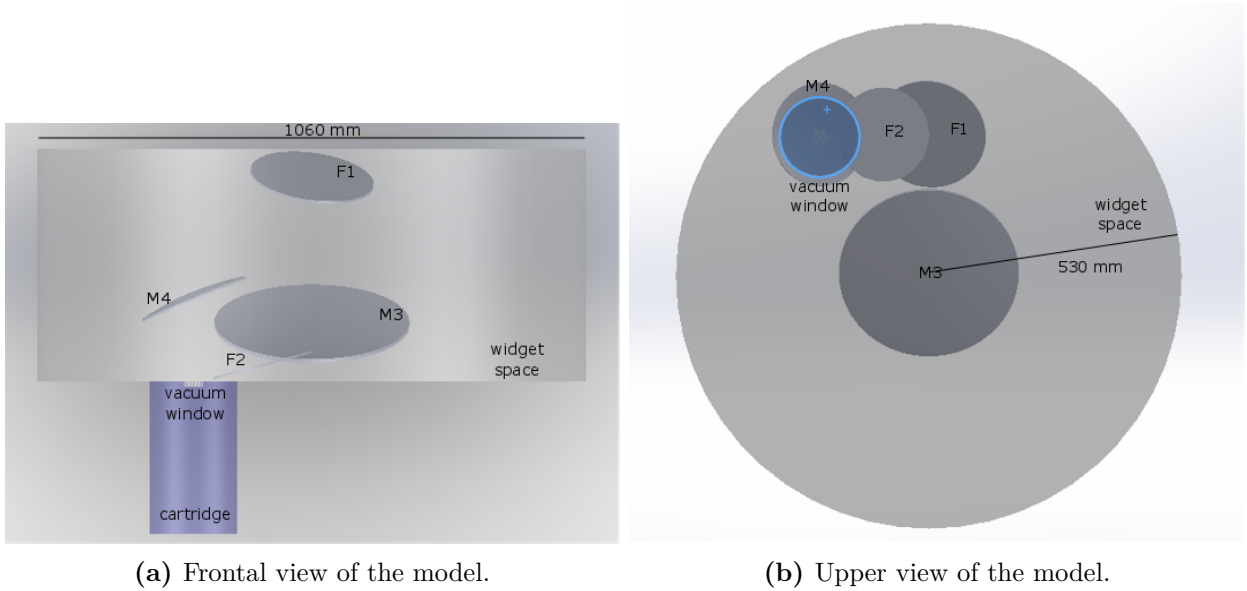


Figure 4.14: 3-D model of the intermediate optical system designed for LLAMA Band-3.

4.9.4 Mechanical considerations for LLAMA

An image of the 3-D model is presented in Figure 4.14. This model was exported from *Zemax*'s optical model and then completed with the available space, and the cryostat space. The system fits in the available space, leaving space for other multi-pixel receivers. The tolerances in construction are the same that were presented for ALMA in Chapter 4.5.

4.10 Analysis of results obtained for LLAMA

The existence of Nasmyth cabins in LLAMA implies that an additional optical system is added to guide radiation to the sides of the antenna. This system is placed between the Cassegrain cabin and the Cassegrain focal plane. For that reason, the mirror that collects incoming radiation, M3, is big. This is a huge restriction for LLAMA design.

One design for LLAMA Band-3 camera was developed. We consider the use of four mirrors, two of them used to have a Gaussian Beam Telescope with magnification $M_{gbt} = 4.5$ and two to compact the system. It was necessary to use two planes, otherwise, the central beam will be placed too far from the center.

The proposed system achieves an illumination efficiency of 79% for the outer pixel, meanwhile the central pixel has an efficiency of 81%. Strehl ratio obtained is 0.960 and 0.957 for LLAMA central and offset pixel.

Beam truncation in the hole of the main reflector is not an issue. For all the mirrors we use the criteria of having $4w$ of the outer pixel contained in the surface to minimize beam truncation.

As the vacuum window is small, the possibility of add flat mirrors inside the cryostat to have more freedom to place the horns can be considered. Cross polarization should be low because we use mirrors instead of lenses. We also considered the use of small incidence angles and long focal length for the same reason. The addition of noise temperature should also be minimal as we restrict the use of lenses in the design.

As in ALMA design previously mentioned, the surface accuracy of the mirrors must be kept under $26.1 \mu\text{m}$ to have total losses under 3.2%. A good alignment of optics is also relevant to guarantee the performance as it is expected.

The vacuum window is planned to be as a fly eye lens made of HDPE. The size of each one is equal to $s_{fp}/M_{gbt} = 13 \text{ mm}$ and contains approximately $3.5w_{0in}$.

Considering that the resolution is the same for a single or multi-pixel receiver, while a single pixel scans a zone of 1 arcmin, the 7-pixel arranged as proposed here can scan 7 arcmin, and the mapping is about 5 times faster (see Chapter 2.4.3). We showed that a more extended array of pixels is possible to design, at the expense of having larger optical devices and increasing lost due to spillover at the secondary mirror.

4.11 Summary

We have presented a design of an optical system for a 7-pixel camera for the 12-m ALMA and 12-m LLAMA antenna. For both designs, we based on the model of a Gaussian-beam Telescope composed by ellipsoidal mirrors.

For ALMA we have thought of a new scheme of band selection, with a flat switchable mirror placed at the Cassegrain focal plane, at the Azimuth axis. Two ellipsoidal mirrors and another flat mirror completed the design of a compacted Gaussian-beam Telescope for ALMA Band-3. The size, shape, focal length and position of the mirrors were presented in detail. This design had a magnification of 2. For the outer pixel, at 100 GHz, a normalized illumination efficiency of 0.97 and a Strehl ratio of 0.995 were obtained. The beam waist at the GBT focal plane was 8.4 mm and the spacing between pixels was 29.3 mm.

For LLAMA we started with a 7-pixel design and then we expand it to 19 pixels. We have considered that an optical system will be installed to guide radiation to Nasmyth cabins. Using the rest of the available space we used two ellipsoidal and 2 flat mirrors to compact the Gaussian-beam Telescope. The size, shape, focal length and position of the mirrors were presented in detail. This design had a magnification of 4.5. For the outer pixel, at 100 GHz, a normalized illumination efficiency of 0.97 and a Strehl ratio of 0.873 were obtained. The beam waist at the GBT focal plane was 3.7 mm and the spacing between pixels was 13.0 mm.

Chapter 5

Conclusion

We have succeeded in the design of the optics for three heterodyne cameras of 7 pixels arranged in a hexagonal distribution. All them operate in W band or ALMA Band-3, which is in the range 85 - 115 GHz.

For the SMWT, a 1.2-m antenna, the available space is reduced. We studied the feasibility of having the 7 pixels illuminating the secondary directly. As this telescope is meant to be for one scientific purpose and only operate in one band, it was possible to optimize for the frequency of interest, 115 GHz. The edge taper used is 10.89 dB and the spacing corresponds to $1.8\theta_{min}$. A normalized efficiency of 0.929 is obtained with 99.69% of the power for the outer pixel.

For ALMA Band-3 camera we propose an optical system formed by a compacted Gaussian Beam Telescope using 2 flat mirrors. This system is optimized for 100 GHz and for the central pixel. Having an edge taper of 10.9 dB, $M_{gbt} = 2$ and an incidence angle of 20° , a normalized efficiency of 0.969 was obtained and 100% of the power of the 7-pixels crosses through the main hole without truncation. The efficiency due to beam distortion and cross polarization was 99.85%.

For LLAMA Band-3 camera similar values were obtained. With an edge taper of 10.9 dB, $M_{gbt} = 4.5$ and an incidence angle of 22.5° , a normalized efficiency of 0.969 is obtained and 100% of the power of the 7-pixels crosses through the main hole without truncation. The efficiency due to beam distortion and cross polarization is 99.38%.

Finally, it was shown that in a simple system as the SMWT, a heterodyne camera is feasible to make, without the use of an intermediate optical system. Nevertheless, with high restrictions on space as it was not designed for that. In a new telescope, some parameters could be optimized for a camera, as the hole in the main reflector.

For more complex antennas as ALMA 12-m and LLAMA 12-m, it is impossible to place a heterodyne camera without the use of intermediate optics, specially if more pixels are installed. They need broadband operation, low levels of noise contribution and more than one band in operation. The intermediate optical systems used for this purposes are usually

Gaussian Beam Telescopes because they allow image formation and are λ -independent. The image formed in the receiver is geometrically the same as the one formed in the Cassegrain focal plane. We achieve a broadband design for both systems.

The normalized illumination efficiency for the three models is over 0.8. Temperature noise and cross polarization was not calculated but the devices used were chosen and designed to minimize its contribution. On the same direction, the size of the optical devices was chosen to contain $4w$ and thus minimize beam truncation. Resolution remains the same and the area covered in one scan increase seven times comparing to a single pixel receiver.

Despite the highly reduced space available and the other restrictions mentioned, the designs presented were successful. If the instruments are planned since the beginning to have cameras, more improvements can be made. A trade-off must be made as the addition of mirrors reduce the quality of the optics in terms of aberrations and cross-polarization. Nevertheless, for the designs presented, it allows an increase of 5 times in mapping speed. Depending on the astronomical goals, one characteristic is preferable than the other. For survey telescopes or to map a big area in the sky, we can choose speed.

5.1 Further Work

The designs presented here are planed for long-term projects, for the second stage of ALMA and for LLAMA, that stills in development. The first approach that we took was to develop a model as a proof of concept. The design of horn antennas is pending and the use of a fully electromagnetic simulation software should be considered.

A more extended array, with a circular configuration of 19 pixels is proposed to be designed. To achieve that, an intermediate optical system with a similar configuration as the one we proposed should be considered. The restriction of space will be more critical as the array is extended.

The design of the back end is also necessary to be develop before terminating the design of the optics. Restrictions of space inside the cartridge for each band is crucial. New designs and maybe the use of digital devices in early stage is an alternative, especially for low-frequency bands.

Once the corresponding horn antenna and fly-eye lens have been designed and the model has passed a fully electromagnetic simulation, the whole intermediate system must be built and characterized. For that, the Millimeter-wave Laboratory of the University of Chile has the necessary equipment to build horns, dielectric lenses and mirrors, and a W-band anechoic chamber to test the performance.

Bibliography

- [1] AUI. AUI web page, news. <http://www.aui.edu/news/experts-from-chile-and-the-united-states-defines-roadmap-to-promote-education-in-astronomy/>. Accessed: September 2nd, 2016.
- [2] ESO. VLT web page. <http://www.eso.org/public/teles-instr/paranal/>. Accessed: September 2nd, 2016.
- [3] APEX. APEX web page. <http://www.eso.org/public/chile/teles-instr/apex/>. Accessed: September 2nd, 2016.
- [4] ASTE. ASTE web page. <http://www.ioa.s.u-tokyo.ac.jp/kkohno/ASTE/>. Accessed: September 2nd, 2016.
- [5] ALMA. ALMA web page. <http://www.almaobservatory.org/>. Accessed: September 2nd, 2016.
- [6] LSST. LSST web page. <https://www.lsst.org/>. Accessed: September 2nd, 2016.
- [7] CCAT. CCAT-p web page. <http://www.ccatobservatory.org/>. Accessed: September 2nd, 2016.
- [8] GMT. GMT web page. <http://www.gmto.org/>. Accessed: September 2nd, 2016.
- [9] ESO. E-ELT web page. <https://www.eso.org/public/chile/teles-instr/e-elt/>. Accessed: September 2nd, 2016.
- [10] ALMA. Science with ALMA. <https://almascience.eso.org/alma-science>. Accessed: July 9th, 2016.
- [11] LLAMA. LLAMA's web page. <http://www.iar.unlp.edu.ar/llama-web/english.html>. Accessed: July 29th, 2016.
- [12] U. Graf, C. Honingh, K. Jacobs, and J. Stutzki. Terahertz Heterodyne Array Receivers for Astronomy. *Journal of Infrared, Millimeter, and Terahertz Waves*, 36(10):896–921, 2015.
- [13] H. Karttunen, M. Poutanen P. Kroger, H. Oja, and K. J. Donner. *Fundamental Astronomy*. Springer, Berlin, 5th. edition, 2007.

- [14] Zemax. What is a Point Spread Function? <http://www.zemax.com/os/resources/learn/knowledgebase/what-is-a-point-spread-function>. Accessed: July 20th, 2016.
- [15] L. Roberts, M. Perrin, F. Marchis, A. Sivaramakrishnan, R. Makidon, J. Christou, B. Macintosh, L. Poyneer, M. Van Dam, and M. Troy. Is that really your Strehl Ratio? In *Proceedings SPIE*, volume 5490, pages 504–515, 2004.
- [16] P. F. Goldsmith. *Quasioptical Systems: Gaussian Beam, Quasioptical Propagation and Applications*. IEEE Press, New York, 1st. edition, 1998.
- [17] G. M. Djuknic. Digital drawing. https://en.wikipedia.org/wiki/Near_and_far_field. Accessed: July 9th, 2016.
- [18] C. A. Balanis. *Antenna Theory, Analysis and Design*. Wiley, New Jersey, 3rd. edition, 2005.
- [19] A. W. Rudge, K. Milne, A. D. Olver, and P. Knight. *The Handbook of Antenna Design*. Peter Peregrinus, London, 2nd. edition, 1983.
- [20] R. C. Johnson. *Antenna Engineering Handbook*. McGraw-Hill, Atlanta, Georgia, 3rd. edition, 1993.
- [21] E. H. Armstrong. A New System of Short Wave Amplification. *Proceedings of the Institute of Radio Engineers*, 9(1):3–11, Feb 1921.
- [22] D. M. Pozar. *Microwave Engineering*. Wiley, New York, 4th. edition, 2012.
- [23] T. L. Wilson, K. Rohlfs, and S. Hüttemeister. *Tools of Radio Astronomy*. Astronomy and Astrophysics Library, Berlin, 5th. edition, 2009.
- [24] R. Rodriguez. Power Point Presentation. not published. 2016.
- [25] L. Olmi. The optical design of relay optics for heterodyne millimeter wave focal plane arrays. *International Journal of Infrared and Millimeter Waves*, 21(3):365–393, 2000.
- [26] R. Güsten, G. Ediss, F. Gueth, K. Gundlach, H. Hauschildt, C. Kasemann, T. Klein, J. Kooi, A. Korn, I. Kramer, R. LeDuc, H. Mattes, K. Meyer, E. Perchtold, M. Pilz, R. Sachert, M. Scherschel, P. Schilke, G. Schneider, J. Schraml, D. Skaley, R. Stark, W. Wetzker, H. Wiedenhover, S. Wongsowijoto, and F. Wyrowski. CHAMP: the Carbon Heterodyne Array of the MPIfR. In *Proceedings SPIE*, volume 3357, pages 167–177, 1998.
- [27] C. Kasemann, S. Heyminck, A. Bell, A. Belloche, C. Castenholz, R. Güsten, H. Hafok, A. Henseler, S. Hochgürtel, B. Klein, T. Klein, I. Krämer, A. Korn, K. Meyer, D. Muders, F. Pacek, F. Schäfer, G. Schneider, G. Wieching, H-J. Wunsch, A. Baryshev, R. Hesper, T. Zijlstra, C.F.J. Lodewijk, and T.M. Klapwijk. CHAMP+: A powerful submm Heterodyne Array. In *Proceedings of the 19th International Symposium on Space Terahertz Technology*, Groningen, April 2008.

- [28] C. Groppi, C. Walker, C. Kulesa, D. Golish, A. Hedden, P. Gensheimer, G. Narayanan, A. Lichtenberger, U. Graf, and S. Heyminck. DesertSTAR: a 7 pixel 345 GHz heterodyne array receiver for the Heinrich Hertz Telescope. In *Proceedings SPIE*, volume 4855, pages 330–337, 2003.
- [29] J. V. Buckle, R. E. Hills, H. Smith, W. R. F. Dent, G. Bell, E. I. Curtis, R. Dace, H. Gibson, S. F. Graves, J. Leech, J. S. Richer, R. Williamson, S. Withington, G. Yassin, R. Bennett, P. Hastings, I. Laidlaw., J. F. Lightfoot, T. Burgess, P. E. Dewdney, G. Hovey, A. G. Willis, R. Redman, B. Wooff, D. S. Berry, B. Cavanagh, G. R. Davis, J. Dempsey, P. Friberg, T. Jenness, R. Kackley, N. P. Rees, R. Tilanus, C. Walther, W. Zwart, T. M. Klapwijk, M. Kroug, and T. Zijlstra. HARP/ACSIS: a submillimetre spectral imaging system on the James Clerk Maxwell Telescope. *Monthly Notices of the Royal Astronomical Society*, 399(2):1026–1043, 2009.
- [30] C. Groppi, C. Wheeler, H. Mani, S. Weinreb, D. Russell, J. Kooi, A. Lichtenberg, and C. Walker. The Kilopixel Array Pathfinder Project (KAPPA): A 16 pixel 660 GHz pathfinder instrument with an integrated heterodyne focal plane detector. In *Proceedings of the 22nd International Symposium on Space Terahertz Technology*, pages 152–158, Tucson, Arizona, April 2011.
- [31] C. Walker, C. Groppi, D. Golish, C. Kulesa, A. Hungerford, C. Drouet d’Aubigny, K. Jacobs, U. Graf, C. Martin, and J. Kooi. PoleStar: An 810 GHz Array Receiver for AST/RO. In *Proceedings of the 12th International Symposium on Space Terahertz Technology*, San Diego, California, February 2001.
- [32] U. Graf, S. Heyminck, E. Michael, S. Stanko, C.E. Honingh, K. Jacobs, R.T. Schieder, and J. Stutzki. SMART: The KOSMA Sub-Millimeter Array Receiver for Two frequencies. In *Proceedings of the 13th International Symposium on Space Terahertz Technology*, Cambridge, Massachusetts, March 2002.
- [33] C. Walker, C. Kulesa, P. Bernasconi, H. Eaton, N. Rolander, C. Groppi, J. Kloosterman, T. Cottam, D. Lesser, C. Martin, A. Stark, D. Neufeld, C. Lisse, D. Hollenbach, J. Kawamura, P. Goldsmith, W. Langer, H. Yorke, J. Sterne, A. Skalare, I. Mehdi, S. Weinreb, J. Kooi, J. Stutzki, U. Graf, M. Brasse, C. Honingh, R. Simon, M. Akyilmaz, P. Puetz, and Mark Wolfire. The Stratospheric THz Observatory (STO). In *Proceedings SPIE*, volume 7733, pages 77330N–77330N–9, 2010.
- [34] C. Groppi, C. Walker, C. Kulesa, D. Golish, J. Kloosterman, S. Weinreb, G. Jones, J. Barden, H. Mani, T. Kuiper, J. Kooi, A. Lichtenberg, T. Cecil, G. Narayanan, P. Pütz, and A. Hedden. SuperCam: A 64 pixel heterodyne array receiver for the 350 GHz Atmospheric Window. In *Proceedings of the 20th International Symposium on Terahertz Space Technology*, Charlottesville, April 2009.
- [35] C. Risacher, R. Güsten, J. Stutzki, H. W. Hübers, P. Pütz, A. Bell, D. Büchel, I. Camara, R. Castenholz, M. Choi, U. Graf, S. Heyminck, C. Honingh, K. Jacobs, M. Justen, B. Klein, T. Klein, C. Leinz, N. Reyes, H. Richter, O. Ricken, A. Semenov, and A. Wunsch. The upGREAT heterodyne array receivers for far Infrared astronomy. In *Proceedings of the 39th International Conference on Infrared, Millimeter, and Terahertz waves*

(*IRMMW-THz*), pages 1–2, Sept 2014.

- [36] M. Sieth, K. Devaraj, P. Voll, S. Church, R. Gawande, K. Cleary, A. C. S. Readhead, P. Kangaslahti, L. Samoska, T. Gaier, P. F. Goldsmith, A. I. Harris, J. O. Gunder- sen, D. Frayer, S. White, D. Egan, and R. Reeves. Argus: a 16-pixel millimeter-wave spectrometer for the Green Bank Telescope. In *Proceedings SPIE*, volume 9153, pages 91530P–91530P–12, 2014.
- [37] K. Sunada, C. Yamaguchi, N. Nakai, K. Sorai, S. K. Okumura, and N. Ukita. BEARS: SIS 25-beam array receiver system for the NRO 45-m telescope. In *Proceedings SPIE*, volume 4015, pages 237–246, 2000.
- [38] K. F. Schuster, C. Boucher, W. Brunswig, M. Carter, J. Y. Chenu, B. Foullieux, A. Greve, D. John, B. Lazareff, S. Navarro, A. Perrigouard, J. L. Pollet, A. Sievers, C. Thum, and H. Wiesemeyer. A 230 GHz heterodyne receiver array for the IRAM 30 m telescope. *Astronomy and Astrophysics*, 423(3):1171–1177, 2004.
- [39] A. L. Fontana, B. Lazareff, A. Navarrini, and Y. Bortolotti. Heterodyne Array Receiver for Radio Astronomy in the 2mm Band. In *Proceedings of the 40th European Microwave Conference (EuMC)*, pages 906–909, Sept 2010.
- [40] A. L. Fontana, C. Boucher, P. Serres, Y. Bortolotti, I. Cope, F. and Stil, B. Lefranc, O. Garnier, G. Butin, F. Mattiocco, S. Navarro, D. John, A. Navarrini, and K. F. Schuster. A 3mm multipixel SIS receiver for IRAM 30-m Pico Veleta Telescope. In *Proceedings SPIE*, volume 8452, pages 84522E–84522E–11, 2012.
- [41] GBT Scientific Staff. Observing with the Green Bank Telescope. <https://science.nrao.edu/facilities/gbt/observing/GBTog.pdf>, November 2015. Accessed: July 12th, 2016.
- [42] P. Bolli, A. Orlati, L. Stringhetti, A. Orfei, S. Righini, R. Ambrosini, M. Bartolini, C. Bortolotti, F. Buffa, M. Buttu, A. Cattani, N. D’Amico, G. Deiana, A. Fara, F. Fiocchi, F. Gaudiomonte, A. Maccaferri, S. Mariotti, P. Marongiu, A. Melis, C. Migoni, M. Morsiani, M. Nanni, F. Nasyr, A. Pellizzoni, T. Pisanu, M. Poloni, S. Poppi, I. Porceddu, I. Prandoni, J. Roda, M. Roma, A. Scalambra, G. Serra, A. Trois, G. Valente, G. P. Vargiu, and G. Zacchiroli. Sardinia Radio Telescope: General Description, Technical Commissioning and First Light. *Journal of Astronomical Instrumentation*, 04(03n04):1550008, 2015.
- [43] FCRAO. SEQUOIA tour. <http://www.astro.umass.edu/fcrao/instrumentation/sequoia/seq.html>. Accessed: July 12th, 2016.
- [44] R. S. Cohen. Columbia University Southern Hemisphere Millimeter-wave Survey Telescope. <http://thirdworld.nl/columbia-university-southern-hemisphere-millimeter-wave-survey-telescope>, 1983. Accessed: July 18th, 2016.
- [45] P. Vásquez. Instalación y Puesta en Marcha del Radiotelescopio Mini. Bachelor thesis, Universidad de Chile, Santiago de Chile, 2011.

- [46] W. Max-Moeberck. Implementación de un oscilador Gunn en un receptor a 115 GHz, para fines radioastronómicos. Bachelor thesis, Universidad de Chile, Santiago de Chile, 2005.
- [47] N. Reyes. Integración física de un amplificador de bajo ruido a un receptor en 100 GHz. Bachelor thesis, Universidad de Chile, Santiago de Chile, 2006.
- [48] M. Vielma. Diseño de un receptor para radioastronomía milimétrica utilizando amplificadores HEMT. Bachelor thesis, Universidad de Chile, Santiago de Chile, 2006.
- [49] N. Ramos. Automatización de un radiómetro para medir la opacidad atmosférica a 115 GHz. Bachelor thesis, Universidad de Chile, Santiago de Chile, 2009.
- [50] P. Astudillo. Medición del Patrón de Radiación del Telescopio Mini. Bachelor thesis, Universidad de Chile, Santiago de Chile, 2014.
- [51] R. Finger. *Design and construction of a digital sideband separating spectrometer for the 1.2-Meter Southern Radio Telescope*. Ph.D. thesis, Universidad de Chile, Santiago de Chile, 2013.
- [52] R. Rodriguez. *Design, Construction And Testing Of A 2SB Receiver For The Southern Millimeter-Wave Telescope*. Ph.D. Thesis, Universidad de Chile, Santiago de Chile, 2015.
- [53] N. Wagner, H. Cong, P. Thaddeus. Documentation of the SMWT: manuals, plans and bitacora. No editorial, compilation of original photocopied information. Placed at MWL, Cerro Calan. 1978-1981.
- [54] Zemax. Optical Design Program. User's Manual. <https://physics.ucsd.edu/neurophysics/Manuals/Zemax/ZemaxManual.pdf>. Accessed: July 29th, 2016.
- [55] J. Leech, B. K. Tan, and G. Yassin. Smooth walled feed horns for mm and submm radio astronomy. In *2013 6th UK, Europe, China Millimeter Waves and THz Technology Workshop (UCMMT)*, pages 1–2, Sept 2013.
- [56] L. Zeng, C. L. Bennett, D. T. Chuss, and E. J. Wollack. A wide-band smooth-walled feedhorn with low cross polarization for millimeter astronomy. volume 7741, pages 774129–774129–9, 2010.
- [57] C. Jarufe. *Ph.D. Thesis, in preparation*. Ph.D. thesis, Universidad de Chile, Santiago de Chile, 2017.
- [58] M. Carter, B. Lazareff, S. Navarro, A. Baryshev, M. Harman, J. Lamb, G.A. Ediss, C. Y. Tham, Y. Sekimoto, M. Matsunaga, V. Heinz, and F. Patt. ALMA Front-end Optics Design Report. FEND-40.02.00.00-035-B-REP.
- [59] M. Carter, F. Coq, A. L. Fontana, F. Tercero, J.A. Lopez-Fernandez, C. Y. Tham, and D. Erickson. ALMA Front-end Optics Design Report. Appendix 3: Band 3 Optics Measurement. FEND-40.02.00.00-035-B-REP. App 3.

- [60] N. Reyes. Solid Works digital drawing. Not published. 2016.
- [61] EHT. Event Horizon Telescope web page. <http://www.eventhorizontelescope.org>. Accessed: January 5th, 2017.
- [62] J. W. Kooi. LLAMA Nasmyth Optics. Presentation. 10th November 2014.

Appendix A

Formulas for conic sections

Table A.1: Main parameters and formulas to define a conic section.

Conic	Eccentricity		Formula		Other
circle	$e = 0$	-	$x^2 + y^2 = a^2$	$r = a$	-
ellipse	$0 < e < 1$	$e = \sqrt{1 - \frac{b^2}{a^2}} = \frac{c}{a}$	$\frac{x^2}{a^2} + \frac{y^2}{b^2} = 1$	$r = \frac{b^2}{a - c \cos \theta}$	$f = c = \sqrt{a^2 - b^2}$
parabola	$e = 1$	$e = \frac{c}{a}$	$y^2 = 4ax$	$r = \frac{2a}{1 - \cos \theta}$	$f = c = a$
hyperbola	$e > 1$	$e = \sqrt{1 + \frac{b^2}{a^2}} = \frac{c}{a}$	$\frac{x^2}{a^2} - \frac{y^2}{b^2} = 1$	$r = \frac{b^2}{a - c \cos \theta}$	$f = c = \sqrt{a^2 + b^2}$

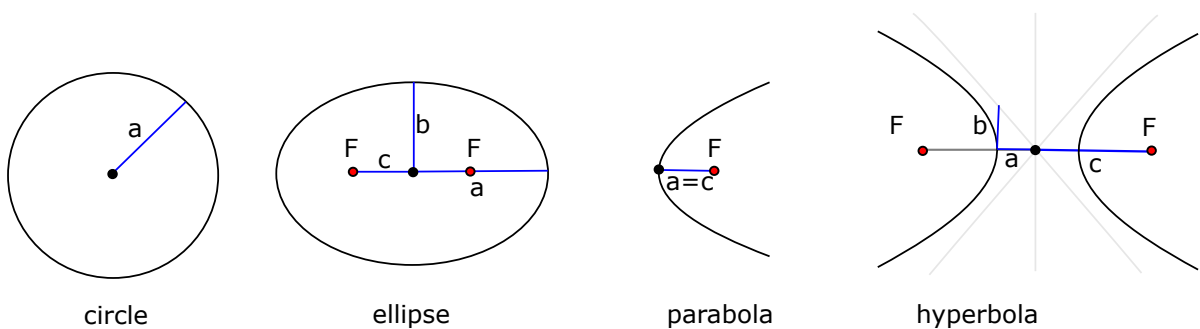


Figure A.1: Conic sections and its defining parameters a, b, c .

Appendix B

ABCD matrix

Table B.1: Examples of ABCD matrix. The direction of propagation is from media 1 to media 2. L is the distance travelled, n_1 and n_2 are the refractive index of the medium, R is the radius of curvature of the corresponding surface and f is the focal length of the device.

Type	ABCD matrix
uniform medium	$\begin{bmatrix} 1 & L \\ 0 & 1 \end{bmatrix}$
slab	$\begin{bmatrix} 1 & L \frac{n_1}{n_2} \\ 0 & 1 \end{bmatrix}$
curved surface	$\begin{bmatrix} 1 & 0 \\ \frac{n_2 - n_1}{n_2 R} & \frac{n_1}{n_2} \end{bmatrix}$
thin lens	$\begin{bmatrix} 1 & 0 \\ -\frac{1}{f} & 1 \end{bmatrix}$
gaussian telescope (thin lens)	$\begin{bmatrix} -\frac{f_2}{f_1} & f_1 + f_2 \\ 0 & -\frac{f_1}{f_2} \end{bmatrix}$
thick lens	$\begin{bmatrix} 1 + \frac{d(n_2 - n_1)}{n_2 R_1} & d \frac{n_1}{n_2} \\ -\frac{1}{f} - \frac{d(n_2 - n_1)^2}{n_1 n_2 R_1 R_2} & 1 - \frac{d(n_2 - n_1)}{n_2 R_2} \end{bmatrix}$

The expression $\frac{1}{f}$ in table B.1 can be used as:

$$\frac{1}{f} = \frac{n_2 - n_1}{n_1} \left(\frac{1}{R_2} - \frac{1}{R_1} \right) \quad \text{for a biconvex lens}$$

$$\frac{1}{f} = \frac{2}{R} \quad \text{for a spherical mirror}$$

$$\frac{1}{f} = \frac{1}{R_1} + \frac{1}{R_2} \quad \text{for an ellipsoidal mirror}$$

$$z_c = \frac{\pi w_{0in}^2}{\lambda}$$

$$R_1 = f \left(1 + \left(\frac{z_c}{f} \right)^2 \right)$$

$$R_2 = f \left(1 + \left(\frac{f}{z_c} \right)^2 \right)$$

$$a = \frac{R_1 + R_2}{2}$$

$$c = \frac{\sqrt{R_1^2 + R_2^2 - 2R_1R_2 \cos(2\theta_{in})}}{2}$$

Appendix C

Hexagonal distribution

Using the hexagonal distribution of pixels with a spacing of $2\theta_{min}$ between them, a sweep width of $5\theta_{min} \cos \alpha$ is obtained. $\alpha = 10.89^\circ$ gives $4.9\theta_{min}$. When a displacement d is done, we obtain an area 4.9 times larger than a single pixel θ_{min} , as shown in figure C.1.

Without considering that the area must be filled, it is possible to cover an area 25 times larger with the hexagonal configuration than with a single pixel, as shown in figure C.2.

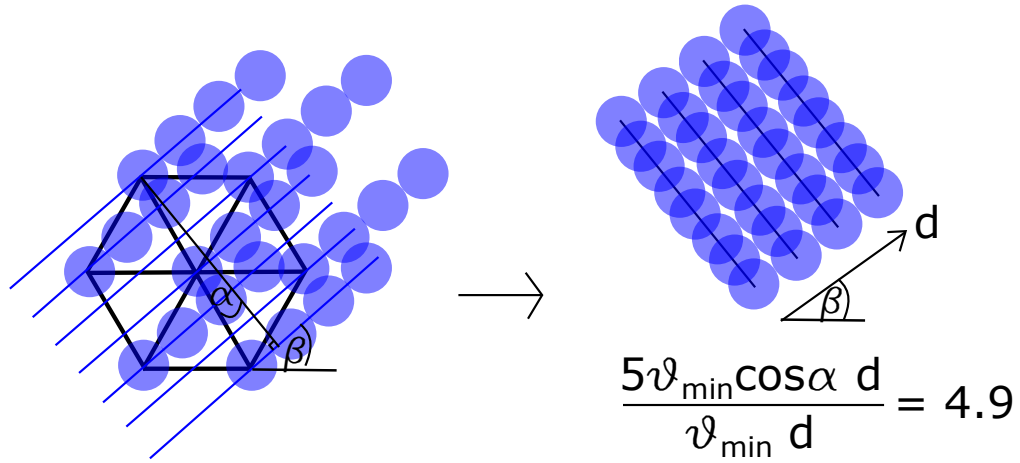


Figure C.1: If an angle β is used to sweep, the best coverage is obtained, having a sweep of width almost 5 times larger than only one pixel.

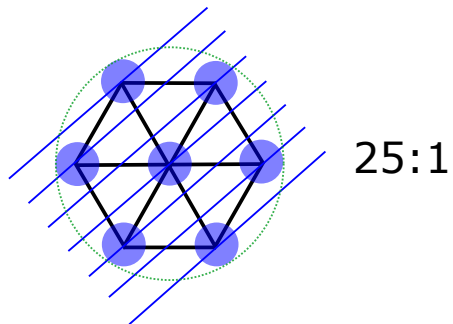


Figure C.2: Hexagonal area coverage is like a circle of radius $2.5\theta_{\min}$. This is 25 times larger than a single pixel.

Appendix D

Parameters of the SMWT in its original units

Table D.1: Main parameters of the Cassegrain antenna of the SMWT (Mini) in inches.

Main Reflector		Secondary Reflector	
Parameter	Value	Parameter	Value
D_m	48"	D_s	7"
a_m	6"	-	-
f_m	18"	f_s	14"
F_m	0.375	F_s	2
e_m	1	e_s	1.2184
α_m	0.131 rad	α_s	1.176 rad
Other Parameters			
f_{eq}	182.9449"	F_{eq}	3.8114
M	10.16	Δ	2.51"
d_{vv}	15.49"	d_{vf}	10"

Table D.2: Main parameters of the corrugated horn antenna of the SMWT (Mini) in inches.

Parameter	Value	Parameter	Value
r_h	0.5815"	r_{wg}	0.0585"
α_h	6°29'15"	α_{wg}	0°
l_h	5.1212"	l_{wg}	0.1000"
RH	5.1541"	th	0.2535"
Parameters of the corrugations			
h_1	0.0480"	d_1	0.2270"
h_2	0.0440"	d_2	0.2300"
h_3	0.0400"	d_3	0.2330"
h_4	0.0360"	d_4	0.2370"
h_{5-92}	0.0320"	d_{5-92}	0.2400"
w_{m1-92}, w_{h1}	0.0300"	w_{h2-93}	0.0200"

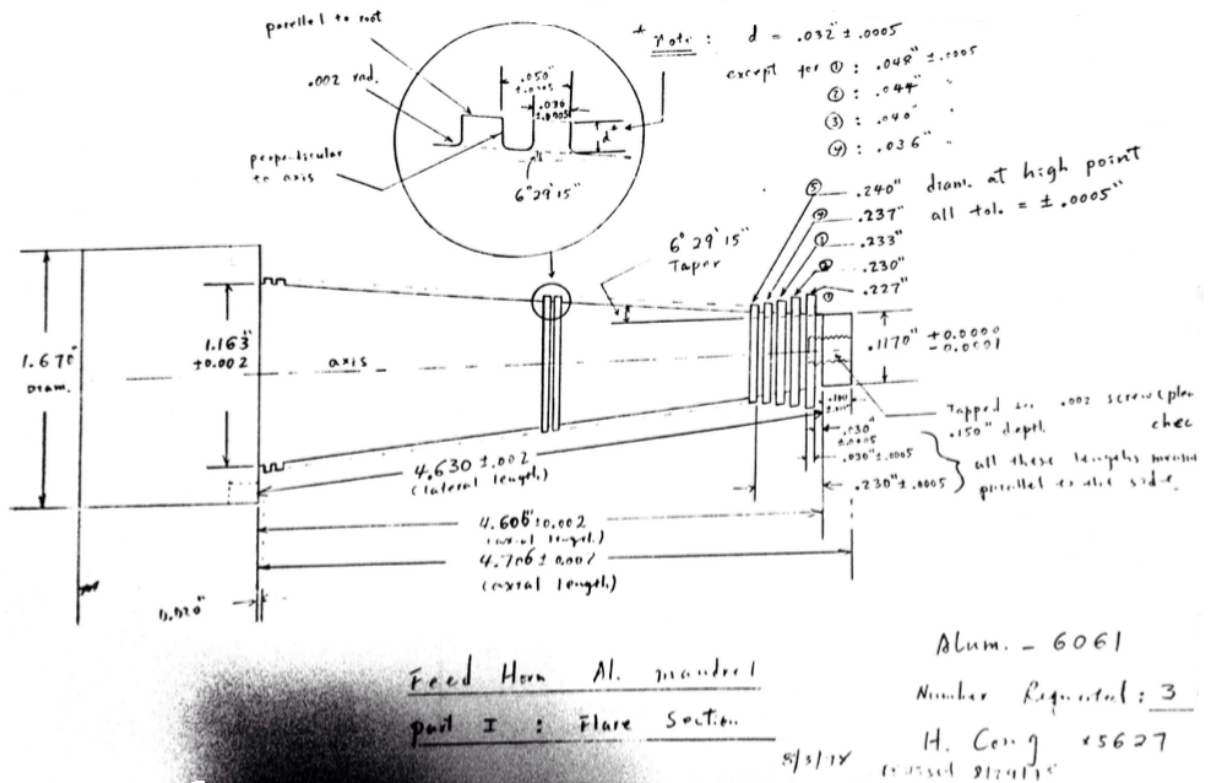


Figure D.1: Original blueprint of the horn antenna of the SMWT

Appendix E

Simulations of the SMWT in Zemax

To simulate the SMWT in Zemax there were used the following parameters

Table E.1: Parameters (in mm) for simulate the SMWT in Zemax.

Surf: Type	Comment	Radius	Thickness	Material	Semi-Diameter	Conic
OBJECT	sky	infinity	infinity		0	0
STOP (aper)	reference	infinity	457.2		609.6	0
(aper)	main	-914.4	-393.46	MIRROR	609.6	-1
(aper)	secondary	-141.409	647.46	MIRROR	88.9	-1.484
IMAGE	feed	infinity	-		0.019	0

Thickness, *Semi-Diameter* ($D/2$) and *Conic* ($k = -e^2$) were fixed using the known parameters mentioned in *Chapter 3*, the *Radius* for the main reflector was calculated as $2f_m$. Then, using the merit function was optimized the *Radius* for the secondary reflector in order to have a focused element. For the main reflector is drawn a center hole of radius 76.2 mm. In emitting mode is used an *Object Space NA* of 0.131 and a Gaussian distribution to illuminate.

Appendix F

Results for the SMWT

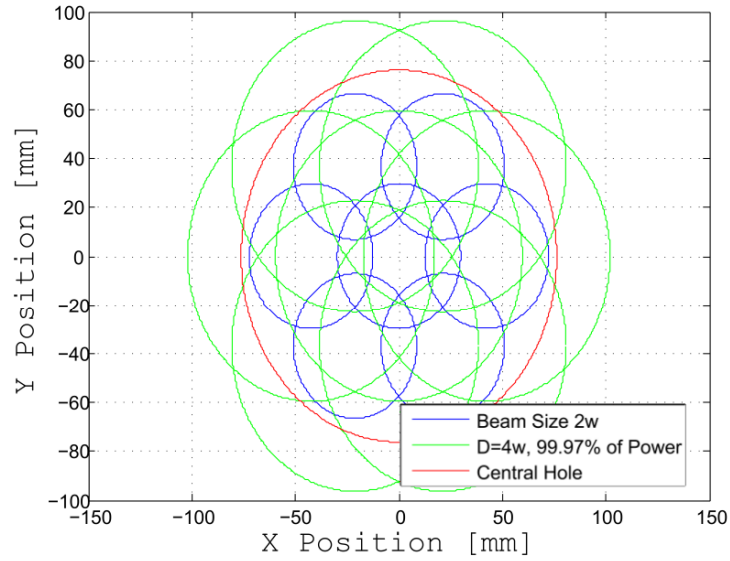


Figure F.1: Plane at $z=254$ mm. Percentage of power that can trespass through the hole of the main reflector of the SMWT using 7 pixels with a distance of 42.42 mm each. Beam waist used is $w_0 = 7.31$ mm for 115 GHz.

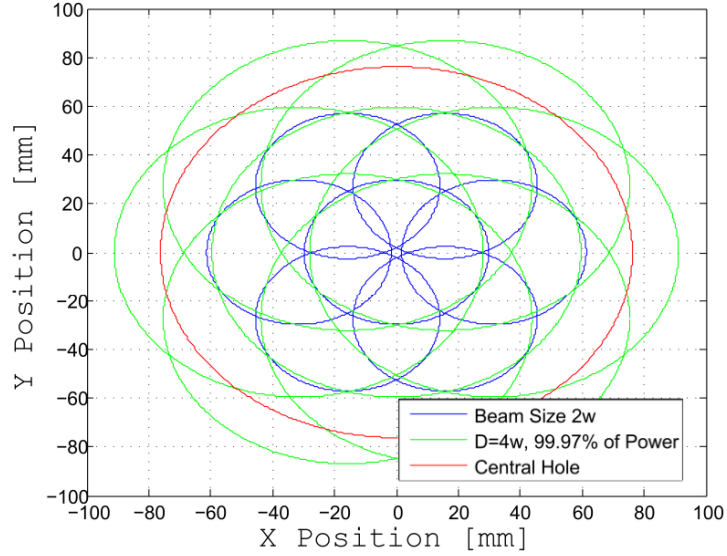


Figure F.2: Plane at $z=254$ mm. Percentage of power that can trespass through the hole of the main reflector of the SMWT using 7 pixels with a distance of 31.54 mm each. Beam waist used is $w_0 = 7.31$ mm for 115 GHz.

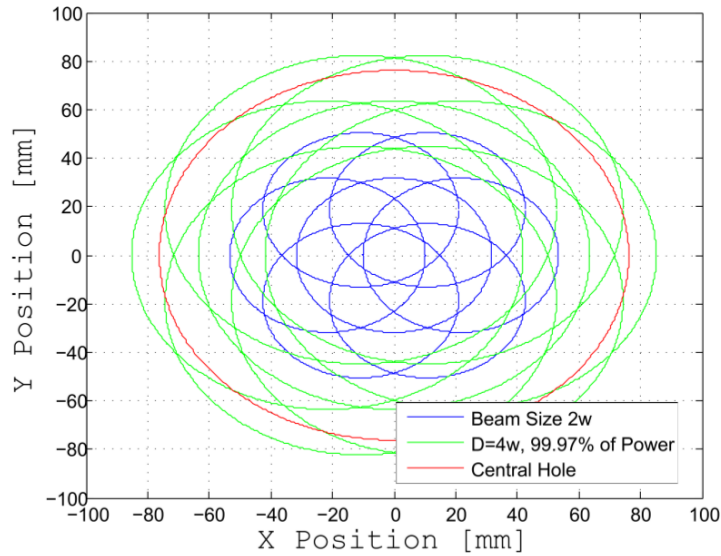
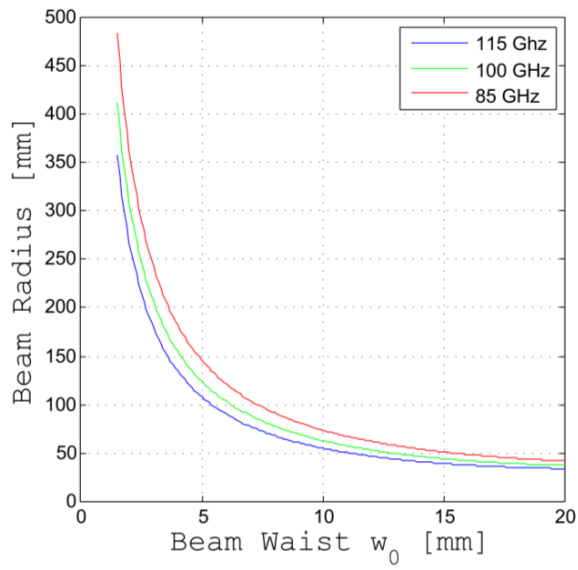
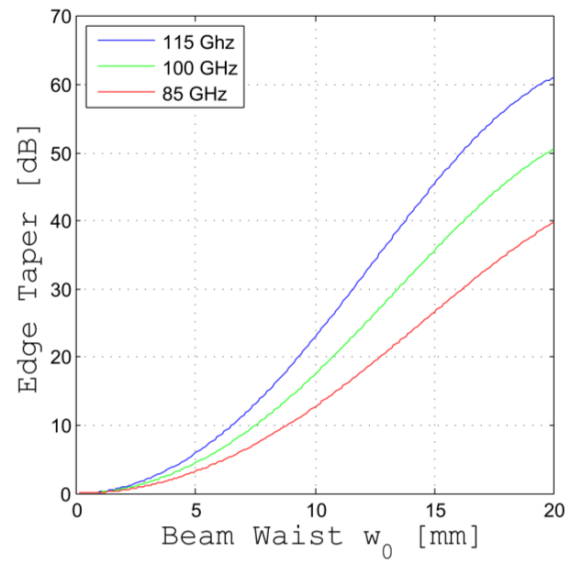


Figure F.3: Plane at $z=254$ mm. Percentage of power that can trespass through the hole of the main reflector of the SMWT using 7 pixels with a distance of 21.63 mm each. Beam waist used is $w_0 = 6.8$ mm for 115 GHz.

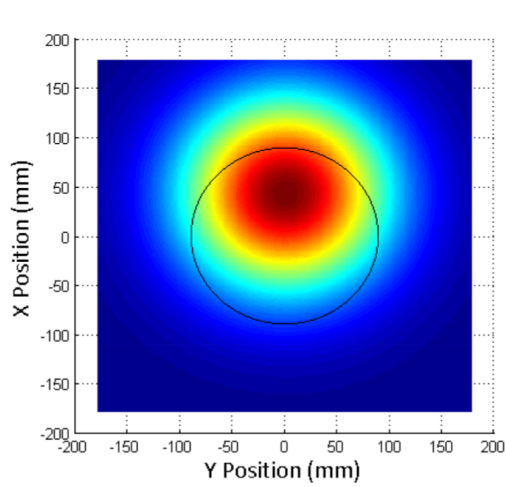


(a) Beam radius w

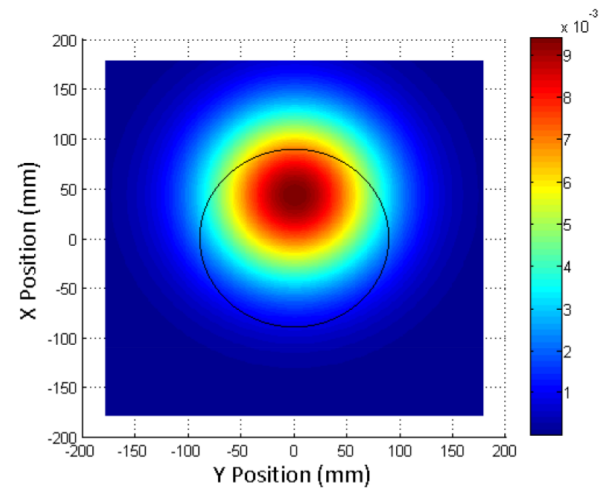


(b) Edge taper T_e .

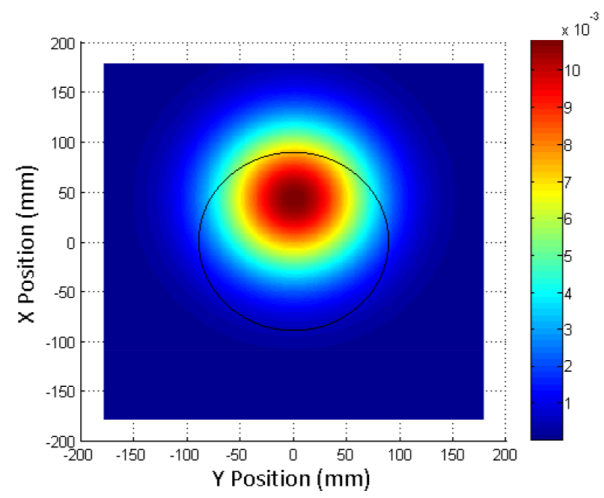
Figure F.4: Beam Radius and Edge Taper at the secondary reflector of the SMWT as function of the beam waist w_0 .



(a) 85 GHz

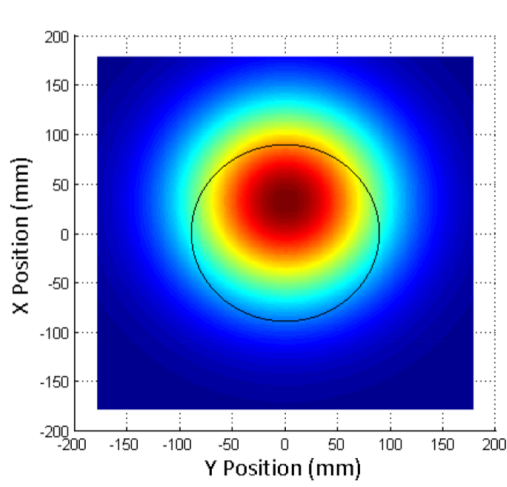


(b) 100 GHz

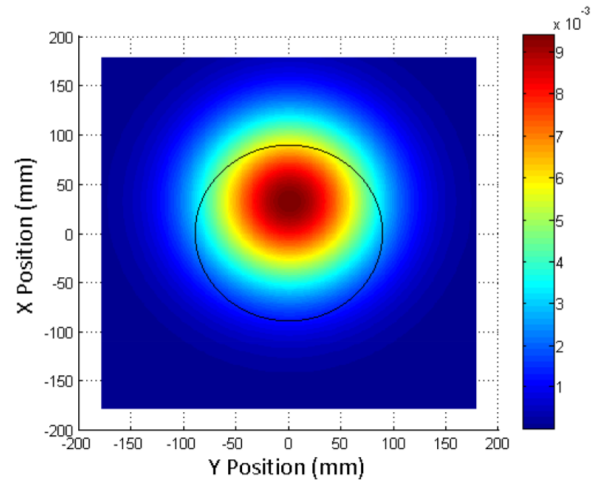


(c) 115 GHz

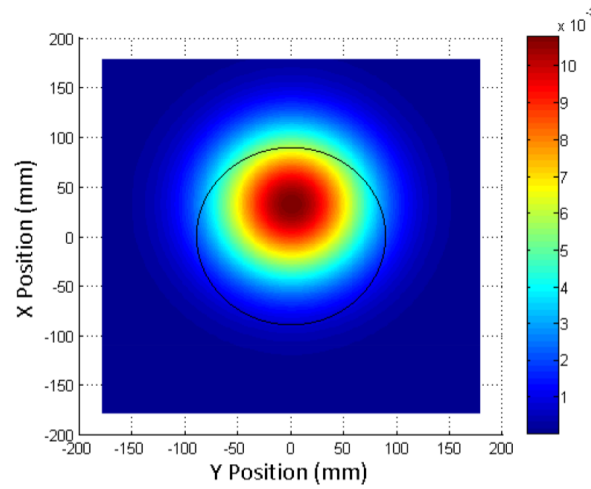
Figure F.5: Distribution of E for an outer pixel displaced 42.42 mm off axis and the secondary reflector border of the SMWT. Results for the current horn antenna.



(a) 85 GHz



(b) 100 GHz



(c) 115 GHz

Figure F.6: Distribution of E for an outer pixel displaced 31.54 mm off axis and the secondary reflector border of the SMWT. Results for the current horn antenna with a thinner wall.

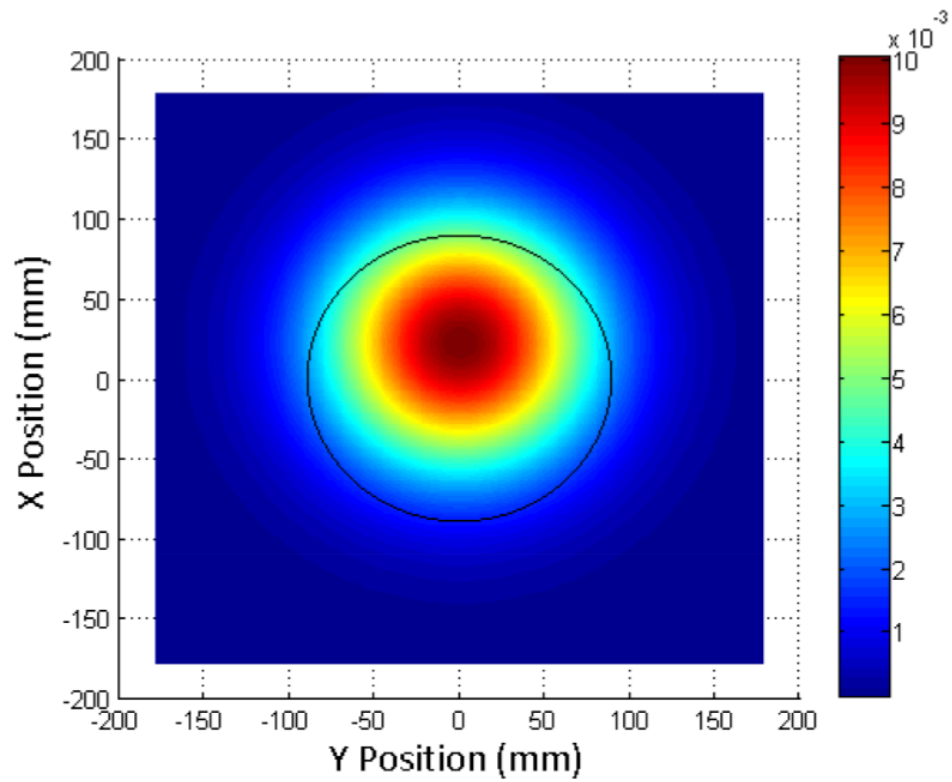


Figure F.7: Distribution of E for an outer pixel displaced 21.63 mm off axis and the secondary reflector border of the SMWT. Results for a horn antenna with a beam waist of 6.8 mm.

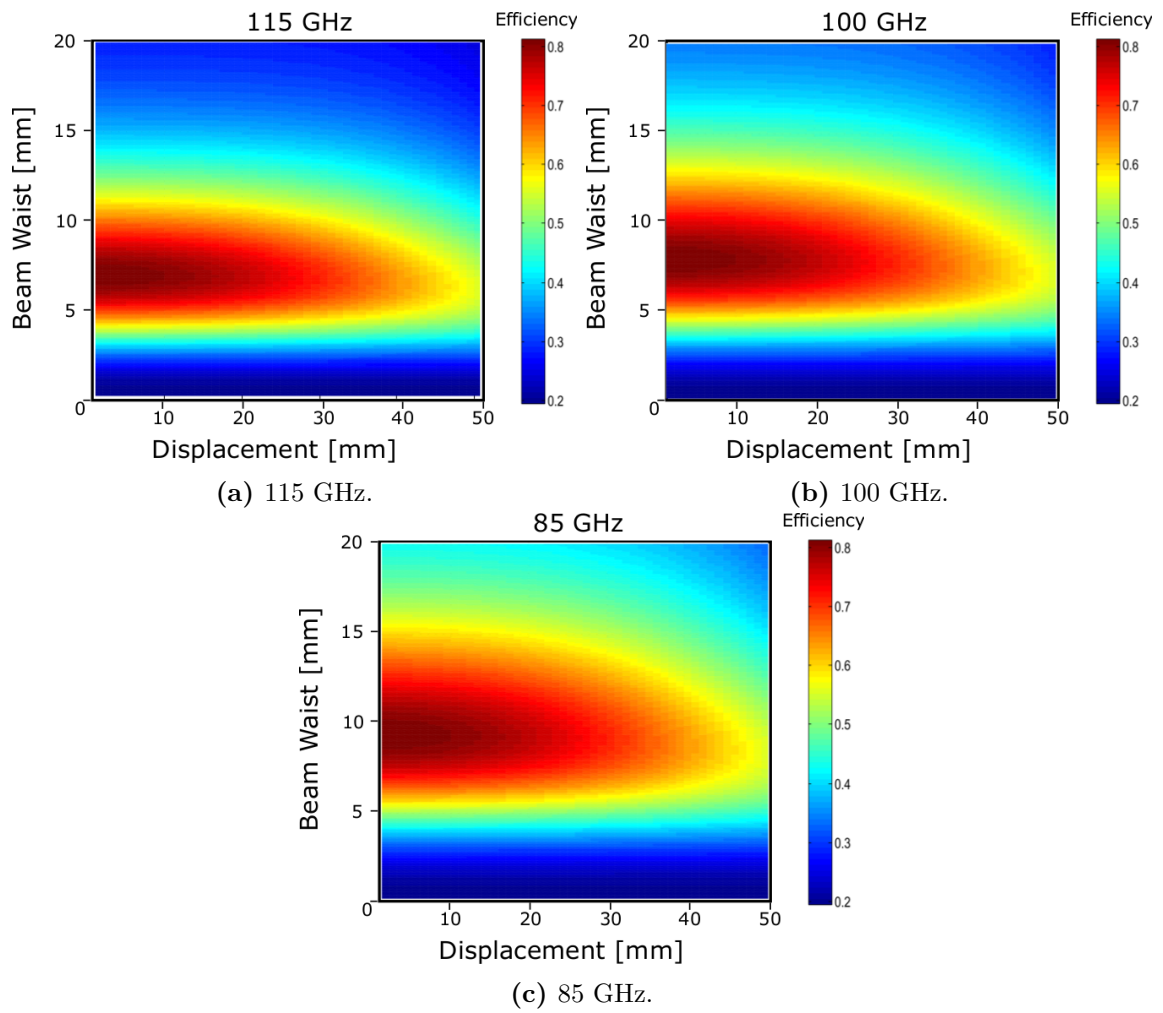


Figure F.8: Illumination efficiency as a function of the beam waist size and the displacement off the center for the SMWT.

Appendix G

Simulations of the ALMA and LLAMA 12-m antenna in Zemax

To simulate the ALMA 12-m antenna in Zemax there were used the following parameters

Table G.1: Parameters (in mm) for simulate the ALMA 12-m antenna in Zemax.

Surf: Type	Comment	Radius	Thickness	Material	Semi-Diameter	Conic
OBJECT	sky	infinity	infinity		0	0
STOP (aper)	reference	infinity	4800		6000	0
(aper)	main	-9600	-4505.9	MIRROR	6000	-1
(aper)	secondary	-619.151	5882.96	MIRROR	375	-1.222
IMAGE	feed	infinity	-		-	0

Thickness, *Semi-Diameter* ($D/2$) and *Conic* ($k = -e^2$) were fixed using the known parameters mentioned in *Chapter 4*, the *Radius* for the main reflector was calculated as $2f_m$. Then, using the merit function was optimized the *Radius* for the secondary reflector in order to have a focused element. For the main reflector is drawn a center hole of radius 375 mm. In emitting mode is used an *Object Space NA* of 0.062 and a Gaussian distribution to illuminate.

To simulate the ALMA 12-m antenna in Zemax, with the Gaussian Beam Telescope designed, we used the following parameters. Coordinate Breaks are used to decenter and tilt the mirrors. Material "MIRR" is an abbreviation of MIRROR, Semi-D is the Semi-Diameter or radius. In Decenter Y we include the simulation of an outer pixel using 29,28 mm for all the surfaces.

Table G.2: Parameters (in mm) for simulate the ALMA 12-m antenna in Zemax and the Gaussian Beam Telescope designed.

Surf: Type	Comment	Radius	Thickness	Material	Semi-D	Conic	Dec X	Tilt Y
OBJECT	focal plane	infinity	20		0	0		
STOP	pupil	infinity	169,97		20,48	0		
CB	elem tilt		0		0			22,5
(aper)	M4	-505	0	MIRR	80,47	-0,629		
CB	elem tilt		-153,87		0			-22,5
CB	elem tilt		0		0		-135	15
(aper)	F2	infinity	0	MIRR	50,38	0		
CB	elem tilt		395,62		0		135	-15
CB	elem tilt		0		0		-230,87	15
(aper)	M3	-600	0	MIRR	126,97	-0,195		
CB	elem tilt		-407,03		0		230,87	-15
CB	elem tilt		0		0		-527,77	22,5
(aper)	F1	infinity	0	MIRR	95,42	0		
CB	elem tilt		5828,20		0		527,77	-22,5
CB	elem tilt		0		0		-527,77	
(aper)	M2	619	0	MIRR	375	-1,222		
CB	elem tilt		-4505,90		0		527,77	
CB	elem tilt		0		0		-527,77	
(aper)	M1	9600	0	MIRR	6000	-1		
CB	elem tilt		1000		0		527,77	
IMAGE	sky	infinity			1000	0		

To simulate the LLAMA 12-m antenna in Zemax, with the Gaussian Beam Telescope designed, we used the following parameters. Coordinate Breaks are used to decenter and tilt the mirrors. Material "MIRR" is an abbreviation of MIRROR, Semi-D is the Semi-Diameter or radius. In Decenter Y we include the simulation of an outer pixel using 13,01 mm for all the surfaces.

Table G.3: Parameters (in mm) for simulate the LLAMA 12-m antenna in Zemax and the Gaussian Beam Telescope designed.

Surf: Type	Comment	Radius	Thickness	Material	Semi-D	Conic	Dec X	Tilt Y
OBJECT	focal plane	infinity	20		0	0		
STOP	pupil	infinity	150		20,48	0		
CB	element tilt		0		0			20
(aper)	M4	-550	0	MIRR	108,55	-0,977		
CB	elem tilt		-135		0			-20
CB	elem tilt		0		0		-129,11	15
(aper)	F2	infinity	0	MIRR	98,55	0		
CB	elem tilt		357,80		0		129,11	-15
CB	elem tilt		0		0		-433,87	15
(aper)	F1	infinity	0	MIRR	120	0		
CB	elem tilt		-296,90		0		433,87	-15
CB	elem tilt		0		0		-198,87	10
(aper)	M3	800	0	MIRR	188,49	-0,641		
CB	elem tilt		6855,90		0		198,87	-10
CB	elem tilt		0		0		-433,87	
(aper)	M2	619	0	MIRR	375	-1,222		
CB	elem tilt		-4505,90		0		433,87	
CB	elem tilt		0		0		-433,87	
(aper)	M1	9600	0	MIRR	6000	-1		
CB	elem tilt		1000		0		433,87	
IMAGE	sky	infinity			1000	0		

Appendix H

Results for the 12-m antenna

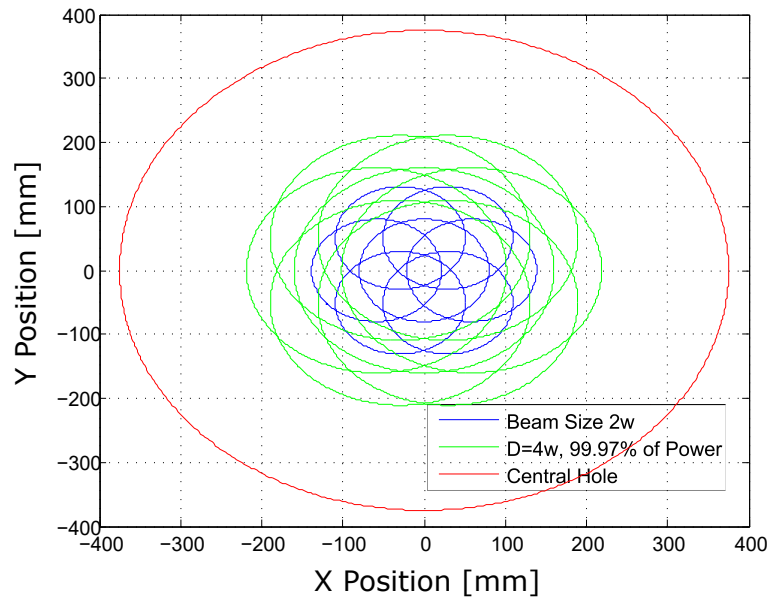


Figure H.1: Plane at $z=1377$ mm. Percentage of power that can trespass through the hole of the main reflector of the 12-m ALMA antenna using 7 pixels with a distance of 58.56 mm each. Beam waist used is $w_0 = 16.8$ mm for 100 GHz.

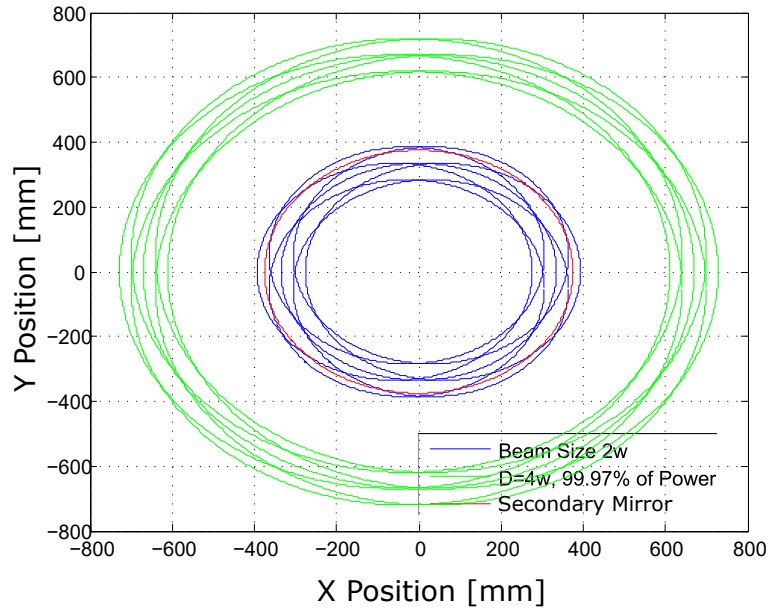


Figure H.2: Plane at $z=5882.9$ mm. Percentage of power that is contained in the secondary reflector of the 12-m ALMA antenna using 7 pixels with a distance of 58.56 mm each. Beam waist used is $w_0 = 16.8$ mm for 100 GHz.

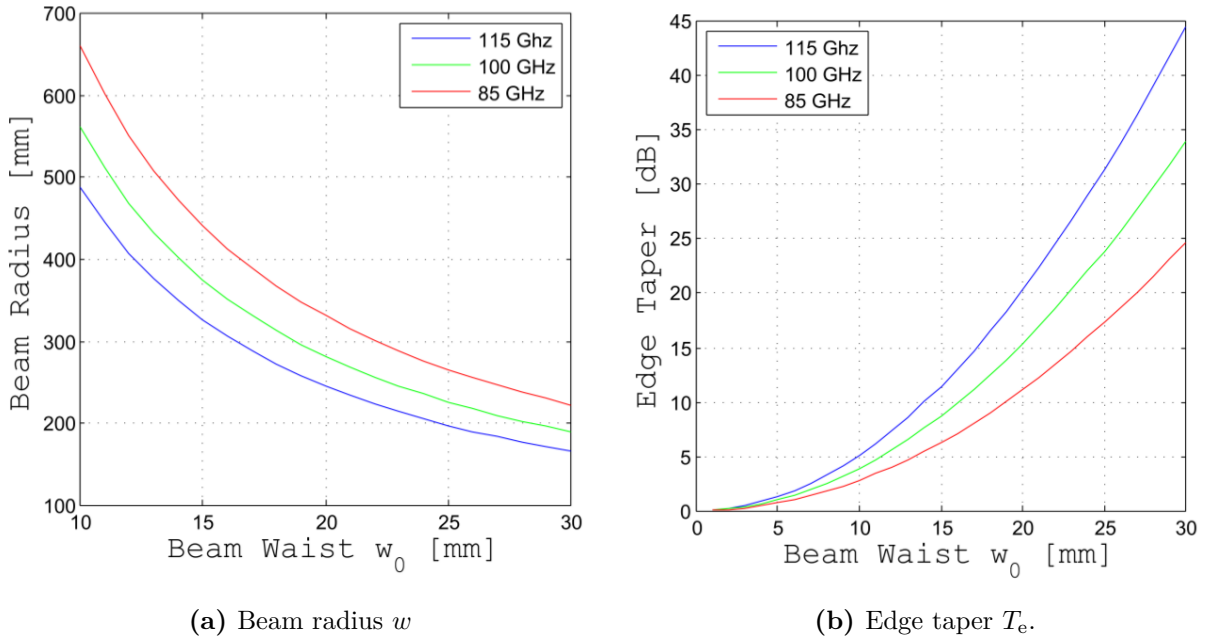
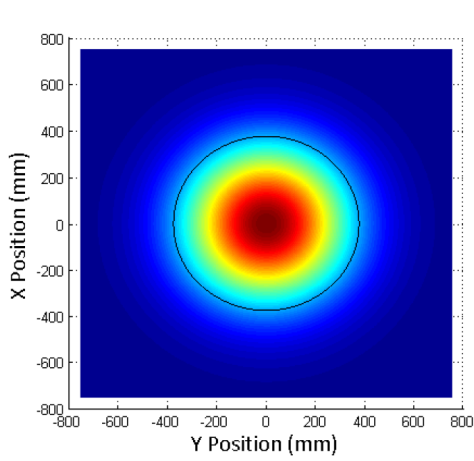
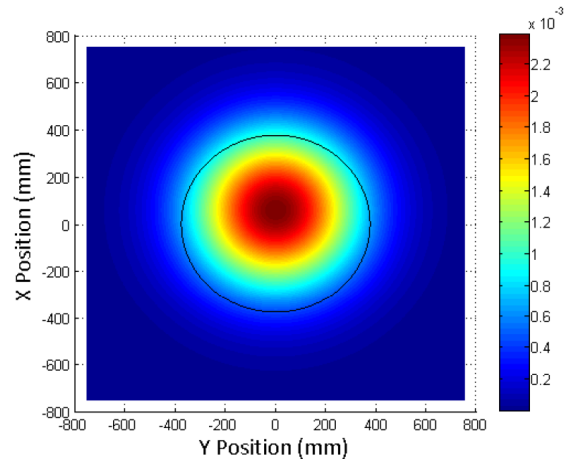


Figure H.3: Beam Radius and Edge Taper at the secondary reflector of the 12-m ALMA antenna as a function of the beam waist w_0 .



(a) Central pixel.



(b) 58.56 mm offset pixel.

Figure H.4: Distribution of E for a central and an outer pixel displaced 58.56 mm off axis and the secondary reflector border of the 12-m ALMA antenna. Results for 100 GHz and an edge taper of 10.9 dB.